3D Printing of Resorbable Metal-Photopolymer Composites Via Novel Vat Agitation System

by

Leyton Janowsky

A dissertation submitted to the Graduate Faculty of
Auburn University
in partial fulfillment of the
requirements for the Degree of
Doctor of Philosophy

Auburn, Alabama
August 8, 2026

Keywords: additive manufacturing, stereolithography, composites, additively manufactured composites

Approved by

Dr. Edward Davis, Chair, Associate Professor, Materials Engineering Program
Dr. Pengyu Chen, Francis Family Associate Professor, Materials Engineering Program
Dr. Bart Prorok, Professor Emeritus, Materials Engineering Program
Dr. Soledad Peresin, Professor of Forestry and Environmental Conservation & Materials Science and Engineering, Clemson University

Abstract

While metallic resorbable materials offer excellent mechanical strength, they are challenging to additively manufacture. In contrast, polymer-based resorbable materials are generally well suited for additively manufacturing but often lack the mechanical properties required for structural implant applications. Incorporating metallic powder additives into polymer feedstocks has improved the mechanical properties of several additively manufactured materials. However, this approach has not been extensively explored for the development of resorbable metal-polymer composites, especially within vat-based additive manufacturing. One potential barrier to the application of reinforcing metallic particles in these fields is the problem of particle settling during vat-photopolymerization additive manufacturing, which can produce non-uniform material compositions and print defects. This study presents both a novel suspension-maintenance methodology for vat-photopolymerization, achieved through continuous mixing of the feedstock during the printing process, and a new additively manufacturable and resorbable composite resin designed to combine the advantages of metallic and polymeric materials without compromising resorbability or biocompatibility. The composite resin was formulated using poly(ethylene glycol) diacrylate (M_n = 250) activated with diphenyl(2,4,6-trimethylbenzoyl)phosphine oxide and reinforced with microscale magnesium particles at concentrations ranging from 0.0 to 6.0 wt%. The agitated resins were fabricated using masked-stereolithography and evaluated for printability through visual assessment and dimensional accuracy measurements to determine the effects and practical limits of both magnesium incorporation and the use

of continuous mixing during printing. Composite specimens of each composition were subsequently characterized through compressive and tensile mechanical testing, microscopy, and mass-loss dissolution studies to evaluate the influence of magnesium addition on mechanical properties and degradation behavior, while also assessing the particle distributions within printed parts. Compression testing to failure was performed using cylindrical specimens measuring 15 mm in diameter and 40 mm in height, while tensile testing to failure was conducted using ASTM type V polymer specimens. The findings demonstrate the feasibility of maintaining homogeneous particle suspensions during vat-photopolymerization without modifying the resin formulation and establish a foundation for future optimization of mechanically enhanced resorbable composites for additive manufacturing.

Artificial Intelligence (AI) Use Disclosure Statement

In the preparation of this thesis / dissertation, the following Artificial Intelligence (AI) tools were used: ChatGPT. These tools were used primarily to assist with technical word choice and consistent terminology. The author acknowledges full responsibility for the intellectual content of this work and has ensured that all AI-assisted sections have been reviewed and revised for accuracy and appropriate academic style. All AI-generated content was reviewed and validated for relevance, appropriateness, and accuracy before incorporation into the final document to maintain scholarly integrity of this research.

Digital Accessibility Use Disclosure Statement

In the preparation of this thesis / dissertation, the following digital accessibility tools were used to ensure this document complies with federal requirements: Adobe Acrobat Pro and Microsoft Word accessibility check. The author acknowledges full responsibility for the intellectual content of this work and has made a good faith effort to comply with digital accessibility requirements in publishing, wherein the nature of the content does not significantly change in order to do so. Furthermore, all content has been reviewed and revised to meet these requirements prior to final publication.

Acknowledgments

Many thanks to my advisor, Dr. Edward Davis, who has provided me with his guidance, his experience, and his helpfulness in telling me the things that I didn't know that I didn't know. I would also like to thank my family and my friends, both of which have been constant sources of support, insight, and guidance. In particular, I would like to thank my fellow graduate student, Ernest Porterfield, who has always gone out of his way to help me with so many things that I will not even attempt to number them here, lest this document become unpublishable due to sheer file size.

Table of Contents

List of Tables

List of Figures

List of Abbreviations

AM	Additive Manufacturing
SLA	Stereolithography
M-SLA	Masked Stereolithography
VPP	Vat Photopolymerization
VPP-MP	Vat photopolymerization – Masked Projection
PBF	Powder Bed Fusion
DLP	Digital Light Processing
FFF	Fused Filament Fabrication
SLS	Scanning Laser Sintering
SLM	Scanning Laser Melting
PLA	Polylactic Acid

PLLA	Poly(l-lactic acid)
PCL	Polycaprolactone
SEM	Scanning Electron Microscopy
BSE	Back Scattered Electron
SEI	Secondary Electron Imaging
M3P	Anycubic M3 Plus VPP Printer
M7M	Anycubic M7 Max VPP Printer
PBS	Phosphate Buffered Saline

Chapter 1 - Introduction

Additive manufacturing (AM) has made significant strides in the last decade, going from a rare though functional laboratory process to a common production method used by millions. While the technological developments that enabled these strides have made additive manufacturing more reliable, accurate, and accessible, there is still considerable opportunity for further refinement. For many functional applications, the material choices available for additive manufacturing can be limited by the requirements of the additive manufacturing process itself. Even though a material might have favorable properties for a specific application, that material might lack the properties needed to be printable, ultimately restricting the properties of the manufactured components [1]. Polymer-based additive manufacturing - including processes such as Fused Filament Fabrication (FFF), Stereolithography (SLA), and Digital Light Processing (DLP) - is relatively fast, accurate, and inexpensive, but the printable polymers often lack the mechanical strength and thermal tolerance needed for many applications [1]. Metal-based additive manufacturing has continued to grow in popularity with processes like Scanning Laser Sintering (SLS) and Scanning Laser Melting (SLM), but remains generally very expensive and, at times, involves difficult and lengthy post processing to obtain a final product [1]. Despite their drawbacks, both polymer additive manufacturing and metal additive manufacturing are used regularly in research for medical applications [2]. Though polymeric methods are often more favorable in terms of cost and processing difficulty, metallic AM is still applied when the application requires properties, especially strength, which are not achievable utilizing current polymer AM methods. A clear opportunity exists for the development of polymer-

based materials which enable the AM fabrication of higher strength components without requiring substantially more complex or expensive processing.

Due to their high flexibility and biocompatibility compared to metal variants, polymeric materials are often favored for soft tissue implants, passive drug release implants, or implants designed to be resorbable [3]. A resorbable implant is a medical device that the body can break down and absorb. This means that a resorbable implant can serve a specific purpose, like providing support during healing, and then safely dissolve once it is no longer needed. The main benefit of resorbable implants is that they eliminate the need for a second surgery for removal. Since the implant dissolves on its own and generally won't require further surgery at a later time, the overall disruption to the healing process is substantially lessened [4]. However, higher strength is an important enabling factor for resorbable implants to be used in a wider range of applications, such as skeletal components and bone scaffolds [5].

In order to enhance the physical properties of polymers, it is a common practice to add metal powders, fibers, or other components to create a composite matrix. This principle has also recently been investigated for improving materials used in AM [6, 7]. Substantial improvements in the mechanical performance of additively manufactured polymeric materials for medical applications have also been demonstrated through compositing [3]. These composites can be more suitable for a wider range of implant applications than unmodified polymers, mainly as a result of their enhanced mechanical strength and durability [3]. Many investigations explore additives focusing on biocompatible metals [8, 9] such as titanium [10]. However, while titanium is high strength and biocompatible, it is not resorbable. As a result, composite materials

utilizing titanium are not fully resorbable and are not suitable for resorbable biomedical applications. Other notable biocompatible but non-resorbable metals commonly used in the medical field include stainless steel, cobalt-chromium alloys, and nitinol alloy. Relatively few groups have attempted to develop metal/polymer composites using resorbable metals, such as iron, magnesium, and zinc. Even fewer research groups have attempted to document the physical properties of composites made of entirely resorbable components. Further research on using resorbable metal additives for compositing is vital for developing biomedical materials with enhanced mechanical properties. However, it remains an open question of what magnitude and what types of mechanical property enhancement are achievable in these systems. Answering this question will be a significant contribution to the advancement of 3D printable devices for biomedical applications as it could lead to materials with improved mechanical performance without compromising their crucial biodegradation characteristics.

Within medical polymeric additive manufacturing, several common production methods are used but FFF, SLA, and DLP tend to be most common. Of these, FFF is known for being clean, efficient, and often inexpensive while vat photopolymerization (VPP) methods, including both SLA and DLP, have a reputation for high resolution and can produce materials with a wider range of properties [1]. However VPP-based methods are generally limited by the need for post-production processes like post-print curing and the removal of excess resin [1]. Development of stronger and more resilient 3D printable polymers has focused on materials suitable for FFF. In contrast, research into enhancing or adding any characteristics beyond mechanical properties, such as shape changing behavior [11], tends to focus on materials suitable for VPP. The

development of strengthening methods applicable to common medical VPP printing materials is an important area for further investigation.

Within VPP systems, however, strengthening can be difficult to achieve. While in FFF and similar processes the material is simply re-formed and reshaped, within VPP it is, instead, chemically polymerized from a liquid feedstock of the appropriate reactants. The chemical reactions involved in VPP printing can be disrupted by even minor changes to feedstock composition and can result in large, negative, changes to material performance [12]. For this reason, VPP feedstock formulation can involve a large number of materials, each designed to carefully control various aspects of the material in order to achieve favorable properties of the final part while also preserving properties relevant for VPP printing within the feedstock [12]. One portion of this that must be controlled relates to the addition of immiscible additives, like, for example, metallic particles. Due to the immiscibility and density differences between the matrix resin and the additives, immiscible materials tend to settle out of suspension over time and can result in changes to the material properties, and thus also the properties of the printed part, over the course of printing [13]. Current research towards the further development of these materials focuses on the use of additional chemical modifications or additives to keep immiscible additives suspended longer within each solution [14]. However, these chemical methods still result in settling during printing, can result in changes in the final part regardless, and are often specific to certain material types and combinations [12, 13, 15]. Further, inside highly-regulated fields like the medical industry, the application of any settling-suppressing chemical additives can necessitate their own regulatory processes and either lengthy assessments to confirm non-

hazardous nature or extensive post-processes for removal before material application. For these reasons, a non-chemical, generally-applicable methodology for limiting particle settling within VPP feedstocks during printing would be of great benefit to the field and possibly enable new forms of composite materials to be manufacturable using VPP.

As result of these research gaps, this study aims to test and evaluate resorbable metals as a strengthening additive for resorbable VPP medical materials. However, due to the possibility of settling within the system, this study also aims to develop and validate a physical method of maintaining additive suspensions within VPP feedstocks during the printing process through continuous mixing and agitation. The specific hypotheses for this research are as follows:

I. Continuously agitating the contents of the resin vat during printing will enhance the homogeneity of arbitrary dense, powdered additives in parts produced via the VPP printing process.
II. The level of agitation required to maintain homogeneity of the dispersed particles will have a minimum impact on the print quality.
III. The incorporation of resorbable metallic powders within resorbable additively manufacturable polymers will provide higher mechanical performance without compromising resorbability.
IV. The mechanical properties of the resorbable metal-polymer composites will depend on the loading ratio and particle size of the metal powder.

Chapter 2 - Literature Review

Modern Medical Implants and Applications

When picturing medical implants, it is common to think of joint replacements, spinal or skeletal reinforcing rods, or the various plates and pins applied to repair fractures. However, there are several other classes of implants with applications that don't necessarily involve being rigid, such as pelvic floor repair meshes [16], polymeric materials for cosmetic implants [17], and scaffolds for tissue engineering [18]. Aside from mechanical properties, many types of implants also demonstrate important functionality, such as resorbability. A resorbable implant is an implant which facilitates or accelerates natural healing while also passively decomposing into non-toxic and non-disruptive byproducts. The decomposition of a resorbable implant results in the complete removal of the implant by the time its purpose is fulfilled, without requiring additional surgery. For example, sutures, one of the most common types of resorbable implants, can be applied internally to hold various pieces of the body together long enough for them to heal and maintain that connection on their own. After the point where healing is sufficiently completed, the suture is slowly disintegrated by the body around it and leaves little, if any, evidence that it was present. The additional surgeries required to recover non-resorbable implants result in further damage to the body and are an important factor in slowing recovery times [4]. Thus, resorbable implants can provide a significant boost to patient well-being by reducing recovery times and avoiding potential complications from additional surgeries. However, the number of situations where a resorbable implant can be used is limited by the mechanical properties of available resorbable materials [19].

Resorbable implants have undergone several important advancements in relatively low strength applications such as biodegradable polymeric stents [20] and tissue engineering [21]. High-strength resorbable materials, for applications such as bone fixation, are in high demand and development on the subject is ongoing, though advancement in the field has been slow [5]. Efforts in the field have focused on two fronts: the development of 100% metal-based resorbable alloys and the improvement of the mechanical properties of resorbable polymeric systems.

Metal resorbable material choices are somewhat limited. The most notable examples are iron, magnesium, and zinc, each of which has its own benefits and disadvantages. While iron is mechanically strong and durable, its speed of degradation within the body is far slower than would normally be considered ideal for resorbable implant applications [19]. Magnesium also has a favorable set of mechanical properties but, conversely, degrades far more quickly under body conditions than desired [19]. Zinc is closer to the generally desired degradation speeds than the other two candidates, but is mechanically weak [22]. As a result, many researchers have sought to develop alloys with considerable strength that are also safely resorbable.

Hong, et al. [23] investigated some possible resorbable alloy combinations in order to determine which had the most advantageous degradation speed, based upon predictions generated from computational models. To do this, they combined iron, manganese, and calcium as powders and then utilized binder jetting additive manufacturing to generate testable parts. Binder jetting utilizes an applicator head, bearing similarities in role to the extruder in FFF processes, to layer-by-layer apply a glue or “binding agent” to a powder bed of a semi-arbitrary material. Once the object is

formed, it is then subjected to intensive de-binding operations where the binding agent is burned away and the powder material sintered into a cohesive solid. While this method did allow them to successfully produce testable components, the use of binder jetting resulted in substantial porosity within the resulting materials. This was suggested as a possible method of further increasing the effective degradation rates of the iron component, through increased surface area, and thus getting closer to the target degradation speed. However, while the porosity may accelerate the decomposition, that increase to porosity appears to change with different material proportions. For example, the Fe-(35wt%)Mn alloy displayed an open porosity of about 39.3%, while the Fe-(34wt%)Mn-(1wt%)Ca alloy displayed a much higher 52.9% open porosity. While the goal of the study was to determine the difference in degradation behavior of the alloys, this difference in porosity was not predicted. The expected change in degradation was a result of the different thermodynamic stability and resistance to hydrolysis of each alloy. As a result, obtaining a specific desired degradation rate by altering composition of these alloys would require carefully balancing the change in porosity with the change in hydrolysis behavior, which may be difficult. It is also to be noted that binder jetting results in substantial shrinkage of the final part compared to the part as designed for the printer. Though this can sometimes be accounted for, this paper reported shrinkage after de-binding was highly variable for the Fe-(34wt%)Mn-(1wt%)Ca alloy: 11.7±2.4%. This variability is not acceptable for the high-precision fits expected from custom-printed biomedical devices.

Oh-ishi, et al. [24] investigated Mg-(0.3 at.%)Ca-(0-1.6 at.%)Zn alloys. Calcium was added to the magnesium as a method of increasing the creep resistance of the final

parts. The addition of both calcium and zinc was reported as enabling the alloy to demonstrate much more age-hardening than a binary alloy of the same components. This behavior could be advantageous for custom-tuning the mechanical properties of the resulting alloy, as might be needed for use in custom implant devices. However, this study did not assess the degradation characteristics or biocompatibility of the alloy. Sun, et al. [25] investigated an alloy of similar proportions, Mg-(0.2 wt%)Ca-(4.0 wt%)Zn, finding it to be highly biocompatible and minimally cytotoxic. A resorbable and hardness-tunable, through age-hardening, alloy of this type is promising. However, the degradation speed was determined to be only 0.08 mm/year slower than that of pure magnesium, 2.13 mm/year. As the alloy remains very similar in degradation speed to magnesium, it is likely to degrade faster than acceptable for most applications [5]. This type of alloy also requires complicated metallurgical processing to produce, limiting its utility for the production of custom implants.

For the second branch and the improvement of resorbable polymer systems, research often focuses on developing composite or hybrid materials that reinforce a polymer with other materials. For example, work by Sharma, et al. [26] focused on creating a composite of a poly(glycolic) acid scaffold then coated with poly(glycolide-co-caprolactone) and crosslinked. This composite was found to have significantly improved mechanical strength in both compression and tension when compared to the unmodified poly(glycolic) acid base material. For the intended application as a stent material, the composite was also found to have expansion properties similar to metallic stents, which are otherwise difficult to approach with polymeric materials due to the differences in mechanical properties. Following these improvements, testing was also

conducted to determine resorbability of the composite and found that it degraded rapidly and completely within conditions similar to the human body. However, the degradation occurred too rapidly to be resorbed appropriately, resulting in unacceptable inflammation of the cells surrounding the implant. Increasing the thickness of the poly(glycolide-co-caprolactone) slowed degradation and provided more acceptable levels of inflammation. However, this change in composition is likely to have influenced the mechanical properties as well, though the mechanical properties of the more thickly coated material were not assessed in this study. Aside from the development of the composite, this paper serves as an important reminder of the importance of precisely controlled degradation rates within resorbable implants.

Polymer-based composites do not, however, have to involve only combination with other polymers and can involve the addition of both metals and ceramics as well. Work by Oosterbeek, et al. [27] explored the addition of phosphate glasses to polylactides to improve their mechanical strength. Additions in ratios near to 15wt% phosphate glass led to increases in ultimate tensile strength and elastic modulus, though also caused the material to become more brittle. Higher proportions of phosphate glass were also correlated with higher absorption of water over the course of degradation. Higher water absorption could have impacts on utility as an implant material if the absorption caused the composite to swell, but swelling of the material was not assessed. The phosphate glass was believed to heighten water absorption by offering hydrophilic pathways for water at the interfaces between the polymer and the glass. As these pathways also facilitate more contact surfaces with the dissolution environment, higher proportions of glass were noted as having faster mass loss when

degrading. However, it was also noted that this mass loss was largely the deterioration of the phosphate glass while the degradation of the polymer component continued largely unaffected. This is stated to possibly be the result of the solution approaching a concentration equilibrium with the surroundings, which would not occur as significantly under anatomical applications.

Strengthening of resorbable polymers via compositing has many possible material combinations to be explored. Some refinement of these wide choices can be found when discussing drug-eluting implants and materials. A drug eluting implant, as the name implies, is designed to release a pharmaceutical agent over an extended period of time and generally into a specifically targeted area adjacent to the implant. Drug-eluting implants often utilize degradation and resorption as a mechanism to control elution rates. Thus, there is a substantial overlap between the polymers and additives utilized in polymer-based resorbable composite materials and those used in drug-eluting implants. These materials have been investigated for a wide range of applications including catheters eluting antibiotics to decrease infection chances [28], chemotherapy agent distribution taking a variety of forms [28-32], stents [32], and pain relief in combination with anti-inflammation [33].

Though drug-eluting implant materials do not tend to have their mechanical properties as a priority, they can provide insights into the resorbability of composites. In addition, drug-eluting implants can demonstrate that the presence of resorbable metals or ceramics can provide benefits to the body and healing beyond simple physical reinforcement. Such benefits to healing are especially noted in tissue engineering scaffold development, where the release of various agents -- such as calcium [34],

hydroxyapatite [35], and magnesium [36] – are used to promote increased healing speed and quality. For example, Gu, et al. [37] investigated the magnesium doping of tricalcium phosphate ceramic bone scaffolds to determine the benefits of magnesium elution on osteogenesis. This paper found that the incorporation of magnesium had substantial positive effects on osteogenesis and the expression of relevant genes without compromising biocompatibility. Further, it was also found that magnesium incorporation heavily strengthened the ceramic matrix.

Up to this point, the discussion of drug eluting implants within this paper has focused upon a “passive release” based condition, where the release of material is controlled primarily by how easily the relevant portions of the body can access it. The correspondent “active release” methods do also exist and can utilize a variety of stimuli -- such as thermal [38], chemical [39], magnetic [40], and many others -- to trigger the release of various portions of the contained pharmaceutical. However, these active types are, at the moment, of less relevance to composite resorbable materials.

In combination with the development of new materials for medical technology, the development and refinement of production methods for those materials has continued as well. One of the most prominent of those production methods is additive manufacturing.

Additive Manufacturing in the Medical Industry

With the recent advances in additive manufacturing technology and manufacturing, the use of additive manufacturing within medical applications has grown substantially. While some of the earliest uses for the creation of dental implants, molds,

retainers, and similar items are relatively well known [41], there are a significant amount of applications which have yet to be fully developed. Some of the main benefits of additive manufacturing in medical applications are the enabling of designed and customized implants, relatively speedy part creation in most cases, and a less expensive resulting component [2]. Of these three benefits, customization of medical implants is considered to be very important for the future of medical technology and has been a major research focus in recent years [2]. A customized implant has several benefits, the most critical of which is that an implant or component can be designed to fit the particular needs of the patient prior to surgery. In typical medical applications involving pre-made non-customized implant components, the patient is made to fit the implant which is available, rather than the implant made to fit the patient. This often involves the shaving down of bone or tissue at minimum, which should generally be minimized in order to preserve as much natural body material as possible. The fitting process is also a significant portion of the time consumed by the general implantation process. Shortening the process by providing a custom implant which requires significantly less modification to fit to the patient can bring immediate benefits to lowering surgical time, difficulty, and cost. Further, any dimensional differences between the used implant and the body component it is designed to replace or supplement can have major impacts upon patient health. In the case of a joint replacement, for example, this can result in a permanent limp or similar if the replacement is a different size or shape than the original [42].

Lee, et al. [42] discussed the drawbacks of conventional implants compared to customized implants in the case of knee replacement. In this case, the contact

geometry of the knee joint is often slightly different between patients, while the implant is not. This means that after implantation with a standard implant, nearly a quarter of patients would experience a substantial change in geometry of the replaced knee joint [43]. The minimization of this difference in geometry, through the use of a custom implant, also minimizes long-term pain as a result of the replacement and results in a lower likelihood of other postoperative issues [42].

As mentioned previously, medical polymeric additive manufacturing generally involves FFF, DLP, and SLA [2]. Medical metal additive manufacturing generally uses some variation of Powder Bed Fusion (PBF), with the main variations directing a scanning laser to melt (SLM) or sinter (SLS) specific portions of freshly applied successive layers of powder in order to create the final object [2]. While PBF methods produce accurate and durable parts, finalizing each component can be complex [1]. The complexity is largely due to the postprocessing procedures required due to surface disruptions. Many of the surface disruptions are generated as a result of spatter created by the scanning laser, which then causes liquid metal to solidify in small amounts outside of the intended printing area [44]. This can have large impacts and generate significantly compromising inclusions, but is most often noted for simple accuracy loss and causing substantial roughness on the part surface [44]. The other primary complication of this process is the creation of significant residual stresses during printing, which can lower the apparent physical properties substantially when compared to bulk formed material [45]. Most PBF production necessitates the use of a purge gas, often argon or nitrogen [46], to minimize the chances of ignition of the powder and to minimize the oxidation of the material before printing. For medical purposes, it should

also be noted that the produced components are typically covered in a thin layer of loose metallic powder. Depending on the material, this powder may pose a variety of dangers to the patient if the component was to be implanted as is, necessitating a thorough cleaning process. Further, the metallic spatter will generally end up contaminating the unused powder from the printing process, either invalidating or significantly complicating reuse of the un-melted powder [47]. These details together generally define PBF and similar processes as very expensive, but providing the valuable capability of producing complex and custom designed metallic components. The cost only increases when adding further parameters such as larger maximum print size or higher print speed.

FFF utilizes a layer-by-layer application of melted thermoplastic filament continuously extruded through a nozzle to develop a final printed component. While one of the most common additive manufacturing processes, it does have drawbacks. One of the most important to consider is that all printing in the FFF mode must occur with final components comprised of layers upon layers of semi-cylindrically cross-sectioned material. Without post-processing, this necessitates a rough, and generally directionally rough, surface [48]. This roughness can be advantageous for facilitating cell adhesion, but can be detrimental if attempting to limit the friction applied by the final surface. Another important consideration is that printing in this mechanism requires the print material to be thermoplastic to allow for flow through the extruder at high temperature, which can limit the choice of materials [1]. In the case of materials designed for drug release, the temperatures involved can also limit the material compatibility or require modifications to the pharmaceutical loading. The high required temperatures bring the

possibility of exceeding the decomposition temperature of the pharmaceutical agent during printing and can facilitate unwanted chemical interactions between the various components. As summary, FFF processes for medical applications are accurate as well as being relatively inexpensive, but can produce high surface roughness and tend to display high amounts of anisotropy [49].

VPP additive manufacturing methods, such SLA and DLP, both rely upon layer-by-layer photopolymerization of a liquid print material, which is generally held in a large vat. Compared to other printing processes, these methods can be considered to be often “upside down”, wherein the printed component moves upwards away from the base material and printing apparatus at the bottom. In these methods, an ultraviolet light or laser is focused onto specific locations to initiate a polymerization, which is then continued layer by layer to complete a structure. These methods are well known for their high accuracy and capability of producing materials with a relatively wide range of properties, with particular focus on the ability to print non-thermoplastic materials [1]. DLP and M-SLA (masked stereolithography) are both known for relatively fast printing speeds resulting from being able to polymerize an entire layer simultaneously. However, these printing processes have drawbacks as well. One of the most important is the requirement of a photoinitiator within the print material in order to generate the free radicals necessary to begin the polymerization process [50, 51]. These photoinitiator materials can have their own limiting characteristics including very precise light wavelength requirements [51], unfavorable biocompatibility or toxicity [51, 52], and can pose the possibility for the free radicals released to interact with not just the intended polymeric material for solidification, but with other components of the material mixture

as well. Different print materials and additives can also necessitate the addition of a UV absorber [52]. Materials demonstrating high refractivity, transmissivity, or similar optical properties can lead to scattering of the UV light which activates the photoinitiator. This scattering causes polymerization to occur in a wider area than might be intended and limits the accuracy of the print. A UV absorber blocks the UV light of the relevant wavelengths, allowing control over the maximum penetration depth of the optical system and the horizontal propagation of the polymerization simultaneously. In whole, VPP processes are very important for the medical industry due to providing highly accurate printing of various highly functional materials. However, the printing material can be more expensive than the polymers used in FFF, and similar processes, and usually requires a thorough cleaning to remove excess liquid print material from the surface of the part.

While the strengths and benefits of metallic additive manufacturing are significant, the processes do have limitations which polymeric additive manufacturing methods do not. Metal additive manufacturing methods have long had the stated difficulties with controlled surface roughness, dimensional consistency, and contaminant leeching as a result of the powderous nature of the print material and the high energies involved [53]. Polymeric additive manufacturing generally involves lower temperatures and more stable print materials, which lowers the cost substantially simply due to having less strenuous performance requirements for the printer. Further, these types of additive manufacturing generally boast high accuracy and comparatively wide print material compatibility [54], both of which can be quite beneficial for medical applications.

Methods of Improving Additively Manufactured Medical Materials

As a result of the rapid increase in interest in additive manufacturing, research in the field of additively manufacturable materials has increased as well. The growing importance of AM in certain high-end manufacturing applications called for materials boasting specific and advantageous qualities to be created [54]. Some examples include additively manufacturable materials demonstrating increased strength, increased electromagnetic absorption, altered electrical properties, and even responsive materials suitable for the fabrication of solid-state actuators [55]. However, not all of the methods used for producing these enhanced qualities are applicable to additive manufacturing or to the medical field.

In standard metallic manufacturing, a handful of options are available for improving the properties of the resulting materials. If the composition is not restricted, alloying can be used to enhance or modify the properties in many ways. Under most conditions, Cold working, and other physical processes, can be generally used to increase strength and hardness while reducing ductility. Heat treatment can be used to influence the grain structure and generate corresponding changes in mechanical properties as well. Other methods like aging might be applicable to specific systems for the control of material properties [24], but are based on atomic interactions that might not be sufficiently pronounced in all cases. Polymeric manufacturing has less possible property improvement methods. Within each polymer, variances on crosslinking ratios and chain length can be produced to result in different bulk properties of the polymer, though this can be difficult to do at the consumer end of production.

Within additive manufacturing, the particularities of layer-by-layer production can introduce other methods of influencing the mechanical properties of resulting materials. For both metals and polymers, changing print parameters can result in altered layer adhesion and altered effective porosity. In metals, the laser parameters used in SLS/SLM can be altered to introduce different grain formations and heat-effected-zone penetration depths, thus also affecting the resulting mechanical properties. Changes in the sizes of the metallic particles that are used as the feed material in printing can also influence the resulting porosity and grain formations. Heat treatments can be used to influence the grain structure or further solidify the structure following printing, though in some cases this can cause shrinkage of the part depending on how it was formed [56]. However, additive manufacturing generally implies a specific structure will be formed, largely invalidating the use of deformation-based strengthening methods like cold working. In FFF polymer manufacturing, different layer heights and the size of the extrusion nozzle can both influence the shapes of the interfaces between each layer and thus the adhesion between layers as well. Heat treatments can be used to slightly melt the polymer and increase adhesion between each layer in FFF processes, which can have few drawbacks so long as the melting does not lead to degradation and can even lead to mechanical strengthening [57, 58]. Chemical treatments can be applied to smooth the surface of the printed part, but this can lead to size reductions and losses in mechanical strength [58]. In VPP processes, post-curing can be performed using additional application of both heat and UV light to increase the extent of polymerization and the mechanical properties of the final material.

When focusing specifically on medical, resorbable, additively manufacturable materials, the number of available strengthening methods reduces heavily. The alloying of metals becomes difficult as many metals are not biocompatible, let alone resorbable, and must be excluded from use. Chemical treatments, like crosslinking agents or part smoothing of polymeric materials, can have many simultaneous impacts on the molecular structure and can be difficult to implement without compromising resorbability. However, while modifying the mechanical properties of each material category can have limitations, combining multiple material categories into a composite can provide an additional method of controlling the resulting properties. Within additive manufacturing compositing, the printability of the “parent” or “matrix” material, that being the material making up the majority of the final composition, can be largely inherited by the following composite. With careful development, the creation of a composite can show the desired additional properties without significant modification to printability and without disrupting resorbability.

In metallic additive manufacturing, the compositing of a metal with a small amount of polymer is not generally an option as the heat required to melt the metal would generally decompose the polymer. However, compositing metals with reinforcing ceramics during PBF processes has had some success in non-medical fields [59]. Within polymeric additive manufacturing, compositing opportunities are more pronounced and involved. Two of the most common methods of creating an additively manufacturable polymer composite are powder incorporation and fiber incorporation. In both cases, a small amount of a second material is added before printing occurs, generally while the base material is in a fluid or fluid-like state or while it is a powder. In

the case of fiber incorporation, the length of the fiber is of great importance [60]. FFF processes can utilize longer fibers since the printing process occurs parallel to how those fibers would be arranged within the filament, while processes like VPP or powder FFF require shorter fibers due to the directional relationship between the feed material and the printed material being much more difficult to predict [60]. The fibers can be a variety of materials for a variety of purposes, but the addition of carbon fiber to increase strength is one of the most common. In this case, longer fibers are generally associated with higher strength, but can have negative impacts upon layer adhesion and maximum print accuracy due to the increase in mechanical stiffness [60]. Powder-based compositing can have a generally easier material incorporation process, but the homogeneity of the produced printing material can be difficult to maintain [61].

One field of interest for polymeric composite materials is composites combining metals with a polymeric primary structure. Composites of this type can demonstrate a wide range of helpful qualities including increased electrical conductivity, thermal conductivity, increased toughness, increased stiffness, and increased strength [62, 63]. Compared to combination with other polymers, metal compositing can generally allow for much larger increases in the noted properties. This field has seen major development with specific focus on additive manufacturing, wherein these mixtures can provide improved qualities without significantly compromising the manufacturability. It should be noted that there are two major methodologies for the usage of this type of material. The first consists of the development of a material mixture where a polymer base is reinforced or supplemented with a metallic secondary component for the purposes of augmenting the properties of the bulk. The second method involves the

development of a material mixture which can be printed using inexpensive polymeric additive manufacturing methods, followed by thermal or chemical processes to eliminate the polymer from the structure and fuse the metallic components into a solid final piece. Despite initial compositing, this method serves as an additional method of producing components that are almost entirely metal. As the second pattern focuses on composite development only to facilitate the creation of a final material which is not intended to be a composite, the rest of this section will focus on the first methodology.

Metal/polymer composites are commonly based on a homogeneous distribution of a powderous metallic material within a polymeric matrix [64]. A further benefit of producing a metal/polymer composite material for medical applications can also be the lowering of the effective stiffness from the values demonstrated by the pure metal. While this may seem contrary to common expectations, fully metallic implants can have their own difficulties that require mitigation. One of the most important is called stress shielding, which describes a phenomenon where an implant which has a substantially higher stiffness than bone ends up absorbing the loads normally applied to an adjacent section of bone. The resulting lack of loading on that section of the skeleton then causes it to degrade over time due to atrophy and disuse. With an appropriate material selection and mixing process, the strength differences between a prospective implant material and human bone can be mitigated. One major application of this type of compositing is the creation of bone tissue engineering scaffolds. These scaffolds provide support and occasionally even nutrients for the regrowth of bone tissue, which necessitates not only a porous structure but also an overall rigidity and strength comparable to that of bone. Many of these scaffolds are also designed with resorbability

in mind so that the scaffold itself does not cause delays or complications during the healing process. Metal/polymer compositing can provide additional control over the properties of scaffolds through modification of the composition of the composite. This control over the compositional material ratios enables an additional method of tuning the performance of parts which require specific mechanical properties in combination with specific degradation rates. Given that the three major resorbable metals – iron, magnesium, and zinc – are also important for a number of bodily processes including healing, their addition to implant components even has the potential to improve healing rates by providing the regenerating tissue with an adjacent and available source of critical nutrients.

Dong, Q et al. [36] investigated this directly by producing polymeric scaffolds composed of polycaprolactone (PCL) and powder-composited with magnesium before FFF fabrication. The produced scaffolds demonstrated improved osteogenic and angiogenic behavior compared to unmodified PCL, indicating that the presence of magnesium did lead to increased regeneration speed. In the case of PCL specifically, the magnesium present was also believed to have served as a catalyst for increasing the biodegradability of the polymeric material. While the majority of this study was focused on bioactive effects of the final composite, compressive strength testing was also conducted and reported. These results indicated that the addition of magnesium to PCL, in weight percents between 1% and 9%, led to increases in compressive strength and modulus. The most significant improvement occurred at 5wt% magnesium with a strength approximately double that of the unmodified PCL.

Jiang, D et al. [8] investigated the incorporation of 316L stainless steel within polylactic acid (PLA) and producing scaffolds via FFF. Similar to magnesium in PCL, the resultant material demonstrated substantially improved compressive strength but conversely showed a negligible effect upon degradation speed. The lack of degradation impact is most easily explained by the fact that 316L itself has minimal vulnerability to the environmental conditions within the human body, which leads to an additional important note on this research. With a 316L steel impregnated PLA structure, the primary structure of PLA will degrade over time, while the steel powder within will not. Though it was not assessed in this study, incorporation of non-resorbable metal powders within resorbable polymers would, during application, eventually expose the inside of the human body to a potentially harmful free floating non-degradable metal powder.

Another scaffold compositing study, conducted by Lee J, et al. [10] combined PLA with titanium. The resulting material demonstrated substantial improvements to compressive strength, as was generally expected, but also demonstrated significant increases to tensile strength. Normally, tensile strength improvements are related to fibrous additives since metallic powders can often serve as stress concentrators, leading to lower strength when tested in tension. Impact toughness increases were also noted and determined as resulting from titanium particulates causing crack pinning. The biocompatibility was noted as being enhanced due to increased cell activity compared to unmodified PLA, but no further investigation was performed into the degradation or terminal degradation behavior.

Shuai C, et al. [65] investigated PLLA (Poly-l-lactic acid) combined with magnesium and produced via SLS. The produced material was described as having substantially increased compressive strength, hardness, compressive modulus, and, by design, degradation rate. The main goal of this study was to evaluate the impact of magnesium inclusion upon the degradation rate of PLLA. It was hypothesized that magnesium would accelerate degradation by altering the pH through formation of $Mg(OH)_2$, which was supported by the conclusions in this study. The study also indicated various biocompatibility benefits from magnesium compositing, including enhanced cytocompatibility, cell adhesion, and cell proliferation.

From each of these studies, it seems clear that compositing in this method has the potential to improve the mechanical characteristics of the implant material, tune the degradation rate of a resorbable material, and provide increases to cellular regeneration all at the same time. However, several investigations have used metallic materials for compositing that are not themselves resorbable. As previously noted, these combinations could cause a release of free non-resorbable metal powder within the body following terminal degradation of the host implant. While some studies have determined that, for example, solid titanium implants demonstrate significant osseointegration [66] and this has been applied to indicate that titanium powder would pose few health hazards due to integrating with the bone rather than being free floating [10], this does not conclusively negate the issue. It remains possible that metallic powder could escape the implant prior to osseointegration depending on the degradation rate, which might be difficult to control to the degree required to eliminate any hazard. This leads naturally to a focus on compositing with resorbable metals that

pose less health risks but still demonstrate the noted mechanical property enhancements. However, extensive analyses of these property enhancements from resorbable metal additives have limited availability at this time, and the field remains open for the development of experimental data quantifying the benefits in certain areas. For example, the development of experimental data related to the compositing of materials for VPP additive manufacturing.

Composites in VPP Additive Manufacturing

Within VPP additive manufacturing, compositing has an additional complication that is not present inside FFF or SLS/SLM systems: settling. Because the printing resin for VPP is a liquid, compositing with solid particulates or fibers will generally result in those solid particulates or fibers falling out of the solution over time [14]. As many SLA/DLP prints can take several hours, especially for larger model designs, the instability of the solution can easily become a factor impacting the properties of the final composite. At this time, there is not a commonly accepted solution.

Several investigations into solid-additives within VPP environments [62, 67-70] have employed ultrasonication to attempt to ensure the resin and additive are homogenized before printing. While this is generally effective at initial homogenization, this method is unlikely to do anything to maintain homogeneity during the printing process. Regardless, these papers did not feature any collection of information related to the changes in the concentration of the additive within the printed component over the course of printing. The investigation by Gil, et al. [70] specifically concluded that

agglomeration and settling could be a problem for further testing, even suggesting possible solutions like heating or the addition of emulsifiers, but did not assess the distribution within printed specimens.

Safee, et al. [14] performed some investigation into the feasibility of chemical modification of additive particles to maintain dispersions. Magnesium particles (~300 nm in diameter) were treated to apply silane functional groups to their outer surface. This process was intended to increase interactions between the resin and the nanoparticle and thus slow precipitation. In order the measure the rate of precipitation, samples of resin containing the dispersed particle were stored under static conditions and sampled from the top layer at selected times. The gathered material was evaluated by collecting an image of the specimen under a microscope and assessing the coloration of the result. The treatment method used here was seemingly successful at slowing precipitation. However, the performance of this process was heavily affected by the resin system that the particle was inserted into. In the tested commercial elastic resin system, only a small amount of particle loss was recorded over the period of testing, while the tested commercial ultra-high resolution resin showed a much lower presence of particles after the same time period. Separately, this test also makes clear that the precipitation rate of materials, even after a chemical treatment, can still be fast enough to be relevant over the course of a VPP additive manufacturing process.

Mousapour, et al. [71] attempted to produce metal powder/polymer resin composites and noted that settling was an issue once crossing a certain threshold of printing time. In order to avoid this, samples were redesigned to be very thin (2mm tall) and print as quickly as possible. While the reduction of physical parameters might avoid

the issue of settling, it does not solve the problem and is unlikely to be reasonable for most additive manufacturing purposes. Xiao, et al. [72] investigated lunar regolith as a filler for photopolymers and suggested that smaller solid particles produce more stable suspensions and more homogeneous particle distributions. However, this study also did not assess the distribution of particles within printed solids or the effect of that distribution upon the final properties. Tang, et al. [73] investigated silicon carbide ceramics dispersed within resin for DLP printing and noted that sedimentation and settling were an issue with time. However, this study provided only that the stability of the produced slurries met the requirements of the printer for production, without further analysis of the impact of settling during printing on the printed parts.

Some recent studies have, however, performed important assessments of settling within commercial resin systems. Prause, et al. [13] examined the microstructure of parts printed from commercial, medical VPP polymer/ceramic composite feedstocks. Though there was significant variance between the materials examined, settling and agglomeration were recorded at the micro-scale even during regular printing processes. In particular, the settling of additive material was shown to occur inside each layer, presumably as the polymerization for that layer occurs, driving the creation of intra-layer inhomogeneity. Further, general inhomogeneity was noted within the whole of the material, even after following manufacturer recommendations for processing and printing only small 2 mm diameter cylinders. Picariello, et al. [15] investigated how several of the properties of a commercial filled resin evolve over time as a result of settling. Most critically, settling within the printing environment, though

exaggerated through the use of an abnormally slow printing profile, was noted to cause immediately noticeable and impactful defects in the final parts.

From these studies in this section, it appears clear that settling of solid material during composite vat-photopolymerization is important for many applications. However, limited investigation has been carried out into the assessment of the effect of settling on the properties of printed materials. Depending on the mixture, it is likely that later-printed layers will have lower concentrations of solid additives compared to earlier printed layers, as a result of those additives settling over time. When printed, this could mean that the final printed layers have substantially different properties when compared to the earlier layers. At this time, very little investigation has been done into the minimization of settling during printing and what research has been done depends on chemical processes that have limited applicability.

Summary and Research Directions

Medical metal/polymer additively manufactured composites are developed based on two main ideas. First, the creation of a stronger material increases the number of potential medical applications due to the increased mechanical properties [64]. Second, the creation of a component demonstrating additional non-mechanical functionality due to the presence of metallic materials – such as components that can supply nearby bone with nutrients to improve healing – increases the range of possible applications as well [36]. However, the literature contains little information on the mechanical performance of many additively manufactured metal/polymer composites. Given that knowing the mechanical properties of an implant would be absolutely critical for its safe

application, a greater understanding of how metallic additives affect the strength, toughness, viscoelastic behavior, and other mechanical properties of polymer-based additively manufacturable composites should be developed.

However, composite development focused towards strengthening or the addition of non-mechanical functionality can result in the mixing of materials without direct concern for their other properties, such as resorbability. As with some of the noted material combinations in the literature review [8, 10], this can lead to the combination of a non-resorbable metallic powder with a resorbable polymeric base. After implantation, this type of mixture could degrade into a cloud of free-floating and moving metallic powder within the body. At this time, there are limited studies that attempted to develop a composite which was fully and safely resorbable while also demonstrating improved mechanical properties.

In addition, the research thus far has focused on FFF and similar extrusion-based processes. However, VPP printing can produce materials with superior performance due to increased crosslinking and limited thermo-plastic behavior [2]. However, the issue of settling during the printing process limits the use of VPP for composite production. There is limited research into preventing or documenting settling within vat-photopolymerization and there is not currently a commonly accepted solution. The lack of significant data on mechanical properties and the clear bias toward FFF as a production technology leaves a clear gap in current research for resorbable metal/polymer composites. This dissertation is intended to help close the gaps in knowledge related to the production characteristics and requirements of metal/polymer compositing within vat-photopolymerization environments and the mechanical

properties of the resulting resorbable composites, while also suggesting a method for addressing settling within VPP printing going forward. Specifically, a mechanical mixing system was designed, constructed, and applied to allow for continuous agitation, and homogenization, of the VPP feedstock during printing.

Chapter 3 - Methodology

Materials

Poly(ethylene glycol) diacrylate (PEGDA, Mn = 250; SigmaAldrich) was selected as the base polymer and diphenyl 2,4,6-trimethylbenzoyl phosphine oxide (TCI America) was used as the photoinitiator to form a photoactive resin. Magnesium powder (99.8%, Beantown Chemical) was selected as the test additive and obtained sieved to -325 mesh, corresponding to a nominal maximum particle size of approximately 44 μm.

For some testing, the obtained magnesium powder was filtered and fractioned further using a 400 mesh screen, producing two additional particle sizes used in specific tests: particles with a nominal maximum particle size of approximately 36 μm and particles with sizes larger than 36 μm, but smaller than 44 μm. Unless otherwise indicated, the as-obtained <44 μm condition was used for testing and formulation.

Feedstock Preparation

For each print, PEGDA was loaded to 2.5 mg/mL of the photoinitiator inside a beaker and magnetically stirred until fully dissolved and a macroscopically homogeneous solution was obtained. 200 mL of the produced solution was then

combined with magnesium powder to the desired loading, between 0.22 wt% and 6.0 wt% magnesium, and additional magnetic stirring was applied for 10 min at 800 rpm. Once the 10 min of initial mixing was completed, the prepared feedstock was immediately transferred to the mixer system and its mixing started, followed immediately by the start of printing.

Gravimetric Sedimentation

A 100 ml volume of PEGDA feedstock was prepared as described above and loaded with magnesium to achieve a concentration of 2.5 mg/mL. The suspension was magnetically stirred at 800 rpm for 10 min in a 150 mL beaker to ensure a uniform initial dispersion. The stir bar was then removed and the beaker was transferred to a balance equipped with an aluminum collection pan which was suspended, within the feedstock, approximately 1 mm above the bottom surface of the beaker. A distance of 1 mm was selected to allow continuous evaluation of accumulated mass without disrupting the experiment and while maintaining sufficient clearance to prevent interaction between the collection pan and sediment accumulating on the beaker base.

The mass of sediment collected on the pan was recorded at regular intervals over a period of 5 hours for correlation with the Stokes' law-based settling velocity of the magnesium particles within the PEGDA matrix. The measured mass was also normalized by the theoretical maximum mass expected to collect on the pan based on the ratio of the pan area to the beaker cross-sectional area, allowing the fraction of settled magnesium to be estimated throughout the experiment.

Additive Manufacturing

Initial test printing was performed on an Anycubic Photon Mono M3 Plus vat photopolymerization – masked projection (VPP-MP) printer, hereafter referred to as the M3P printer, while later PEGDA-Mg composites were produced on one of two Anycubic Photon M7 Max VPP-MP printers, hereafter referred to as M7M-1 and M7M-2. All three printers are shown in Figure 1. VPP-MP, like several VPP methods, enables the polymerization of entire layers simultaneously.

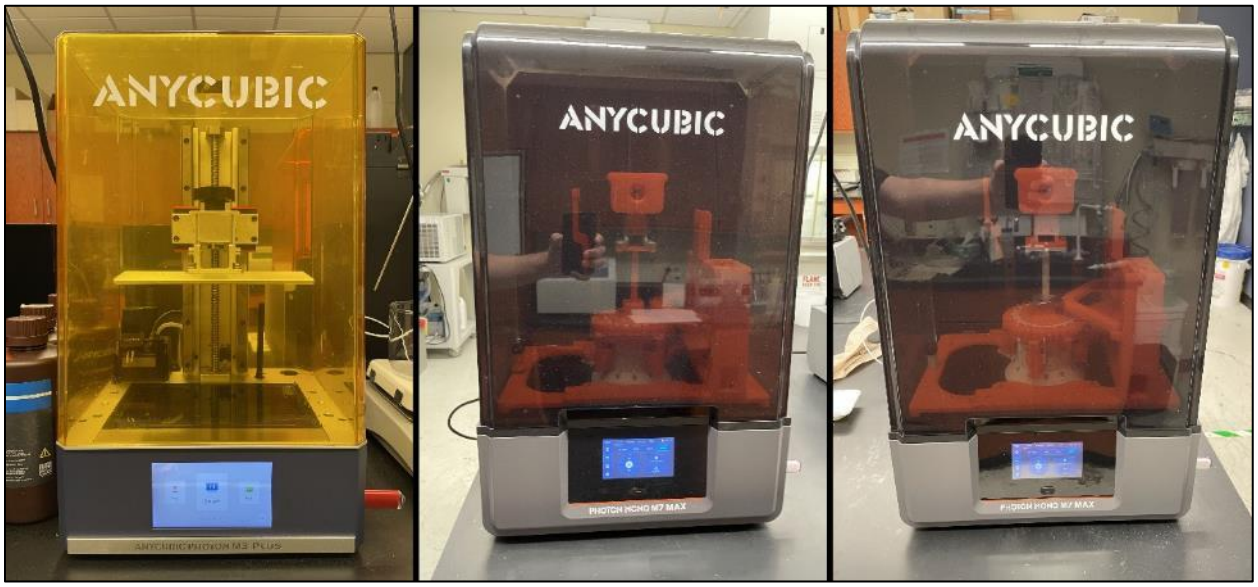

Figure 1. Printers used in this work. Anycubic M3 Plus (left), Anycubic M7 Max - 1 (center), and Anycubic M7 Max - 2 (right).

A summary of used printing parameters for the M3P printer is provided in Table 1. For reference, the mixing speed refers to the speed of the mixing system during printing and exposure time refers to the number of seconds that each layer is exposed to the UV source for polymerization. Layer thickness is the vertical height of each liquid layer as it is polymerized, which is controlled by a corresponding change in build

platform position between layers. Movement of the build platform is controlled by the Z lift speed, which controls how fast the platform moves upwards after a layer is completed, Z lift height, which controls the total height that the platform is lifted to between layers, and the Z retract speed, which controls the speed at which the platform returns downwards to start the polymerization of the next layer. A layer exposure time of 8 s was selected, which provided stable curing behavior and consistent part formulation under the tested conditions. Mixing behavior was kept to simple, single-direction, single-speed, continuous mixing throughout the whole printing process. Printer M3P was used only to produce low-additive samples (2.5 mg/mL of magnesium) under various mixing speeds, with two stir bars attached opposite each other in the mixing chamber.

Table 1. Print parameters utilized in the production of the test samples on printer M3P, including total print time for a single 40 mm tall cylinder with a 15 mm diameter.

Printer	Mixing Speed (rpm)	Exposure Time (s)	Off Time (s)	Layer Thickness (mm)	Z Lift Distance (mm)	Z Lift Speed (mm/s)	Z Retract Speed (mm/s)	Total Print Time (hours)
M3P	0	8	5	0.05	6	6	6	4.43
M3P	100-250	8	10	0.05	40	6	6	8.28

Due to slight variances between printers, as can commonly occur in consumer and commercial grade systems, the print parameters needed to achieve the same printer performance were different between all three tested printers. In addition, higher

additive content resulted in more limited UV penetration, as expected, requiring slightly higher curing times in each layer to achieve appropriate print quality. Similarly, printer M7M-2 experienced a slight reduction in UV curing efficiency, likely a sign of aging within the system's UV source, over time, requiring additional exposure time to preserve print quality in later prints, generally needing approximately 2 s of additional exposure time compared to M7M-1. To account for these differences in the mechanical evaluation of PEGDA-Mg, off time was used to increase per-layer time and keep total printing time for each parameter set the same. In addition, the M7 Max printers supported newer two-stage movement profiles for the build platform, allowing a slow withdrawal and retract to the printing surface (stage 1) while also allowing a higher speed for moving to the total Z lift distance afterward (stage 2) and allowing homogenized resin to refresh the printing zone. The primary printing parameters for printers M7M-1 and M7M-2 can both been seen in Table 2. All printing of PEGDA-Mg hybrids on printers M7M-1 and M7M-2 occurred at a mixing speed of 250 rpm, in single direction mixing with four stir bars attached, unless otherwise stated.

Table 2. Primary print parameters utilized in the production of the compression and tensile test specimens on printers M7M-1 and M7M-2.

Printer	Type	Exposure Time (s)	Off Time (s)	Layer Thickness (mm)	Z Lift Distance (mm) (stage 1 – stage 2)	Z Lift Speed (mm/s) (stage 1 – stage 2)	Z Retract Speed (mm/s) (stage 1 – stage 2)	Total Print Time (hours)
M7M-1	Compression	14	6	0.05	2 - 30	1.5 - 6	1.5 - 6	7.33
M7M-1	Tensile	14	0	0.05	2 - 20	1.5 - 20	1.5 - 20	6.86
M7M-2	Compression	16	4	0.05	2 - 30	1.5 - 6	1.5 - 6	7.33

Printed used three primary models. First, a cylindrical, 40 mm tall 15 mm diameter cylinder model was printed, with one circular face directly on and in the center of the build platform, for compression testing and microscopic analysis. Second, ASTM Type V tensile testing dog bones were fabricated vertically, in sets of three, positioned radially around the center of the build platform and alongside a small set of supports to assist with stability. Third, an hour-glass shaped model was designed to provide various measurements related to print quality. All of the printed models can be seen in Figure 2.

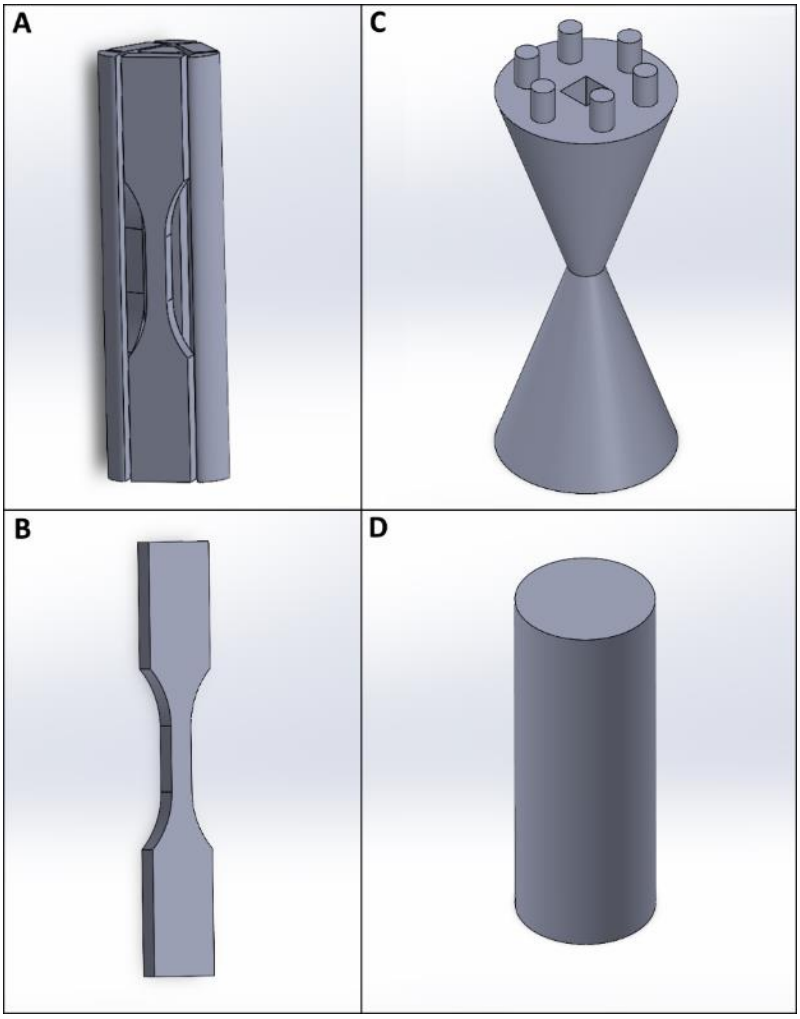

Figure 2. 3D models of printed parts: (A) tensile specimens with supporting structure for printing, (B) Tensile specimen, (C) Quality Test Model, and (D) Compression Cylinder.

Print Quality Assessment

In order to assess the quality of components, and how the operation of the mixing system may impact the quality, the quality test model was printed without magnesium at speeds of 0, 100, and 250 rpm and at curing times of both 10 and 14 seconds on printer M7M-1, otherwise using the same printing parameters as the compression cylinders. Once printed, these models were visually assessed for general

quality, then measured using calipers with a resolution of 0.01 mm. Measurements were collected of the total height of the hourglass section, the diameter of the hourglass at its thinnest point, and the diameter of the hourglass at its widest point. The small cylinders on top of each hourglass were assessed by measuring by their diameter and height, while the square cut-in was assessed using its depth and wall length. Each measurement was collected three times on the same specimen, then averaged and recorded.

Microscopy

Cylindrical compression specimens were fabricated as described above. Following fabrication, each cylinder was sectioned so as to expose the longitudinal centerline using an aluminum oxide cut-off wheel. The exposed surface was then polished via sequential grinding with using 180 grit aluminum oxide abrasive paper followed by 400, 800, and 1000 grit silicon carbide abrasive papers to produce a surface suitable for microscopic examination and particle counting.

Microscope images of the polished longitudinal centerline were acquired at 2 mm intervals along the height of each cylinder. Images were not collected from the extreme top or bottom edges as artifacts resulting from the sectioning process had affected those regions. Both optical microscopy and scanning electron microscopy (SEM) were used for characterization. For optical microscopy, each image captured an area measuring 1.12 mm wide and 0.839 mm tall, with the width of the image parallel to the print direction. SEM images, for image processing, were acquired at 40x magnification, corresponding to an imaged area measuring 2.98 mm wide and 2.24 mm tall, with the

height of the image parallel to the direction of printing. All SEM images used for image processing were collected in compositional-contrast backscattered electron (BSE) mode, while selected images for topographical interest were collected via secondary electron imaging (SEI). SEM images for other analysis were obtained under similar magnifications and specimen orientations to those used for image processing, unless specified otherwise. Prior to SEM imaging, specimens were sputter-coated with gold to a nominal coating thickness of 24 nm.

Image Analysis

Image analysis was performed using ImageJ. Individual particles were identified via grayscale intensity thresholding, allowing determination of both particle count and particle area fraction for each image. Due to slight variations in background intensity within the collected images, a single global threshold was not applicable across the entire dataset. Therefore, the contrast limits used for thresholding were adjusted manually according to a consistent criterion, selecting threshold values such that measured particle boundaries coincided with the visually identifiable particle edges in the original image with a minimal inclusion of background pixels. All image analysis was performed by the same researcher and according to the same image-processing procedure.

Simulation

In order to determine what area fraction would be expected for a given metal/polymer ratio, the stereological relationship described by Delesse's principle

should apply, where the average plane-intersected area of particles would be identical to the volume fraction of those particles. However, this relationship assumes that a representative image set is available. In the case of the produced samples, microscopy focused on high magnification with the intent of providing distribution information as close to a layer-by-layer assessment as was feasible. For this reason, microscopy could not sample a sufficiently large representative area for direct application of Delesse's principle and a particle-size-based imaging bias due to limited imaging area was likely. To account for this issue, a Monte Carlo simulation was implemented in MATLAB to produce expected values for area percent from images which could not capture a fully homogeneous continuous volume. Within this simulation, particles were randomly distributed throughout a periodic 1 mm^3 representative volume element. Then, two-dimensional cross-sectional planes of the volume were randomly selected and the area fraction of particles in each plane could then be calculated and recorded. After many simulations, these calculated measurements were averaged to produce an expected area fraction occupied by additive particles for a range of specified weight fractions. To account for particle overlapping during the random distribution, any overlapping particles were assigned repulsive interaction forces and the system was iteratively relaxed until the total overlapping particle volume fell below 1%. The periodic nature of the volume allows for moving particles which exit one boundary to immediately re-enter from the opposite side, minimizing boundary effects on both particle distribution and sectional area evaluation. The particles were simulated under the assumption of spherical morphology and assuming that particle diameter was normally distributed with a 10 μm standard deviation. Mean particle size was varied between 20, 25, and 30 μm

while the additive loading was varied between 0.1 wt% magnesium and 20.0 wt% magnesium. For each condition, a total of 1000 random particle distributions were simulated and each evaluated using 1000 randomly selected measurement planes.

Mechanical Testing

Compression testing was conducted utilizing an Instron 5982 universal testing machine while tensile testing was conducted utilizing an Instron 68TM-10 universal testing machine. Compression testing was conducted at a strain rate of 1.3 mm/min, in line with ASTM D695, with a 100 kN loadcell, calibrated according to ASTM E2 to an accuracy within 1% of reading, a resolution of 0.25 N, and a minimum calibrated loading of 0.18 kN in compression. Tensile testing was conducted using a strain rate of 1.0 mm/min, in line with ASTM D638, using a 10 kN loadcell, calibrated according to ASTM E2 to an accuracy within 0.5% of reading, a resolution of 0.025 N, and a minimum calibrated loading of 10 N in tension.

Mechanical testing was conducted on specimens containing 0, 1, 2, 3, 4.5, and 6 wt% magnesium, which each condition containing at least three specimens. Additional testing was performed at 3 wt% concentrations using magnesium particles filtered, from the obtained condition of <44 μm in size (-325 mesh), to <36 μm (-400 mesh) in size and utilizing the particles retained above the filter to create specimens with particle size between 36 and 44 μm. In the case of compression, only one specimen could fit on the build plate at a time, resulting in each condition being produced over multiple individual prints, each with their own feedstock preparation process. In the case of tension, three specimens could be printed simultaneously, allowing indicated testing within the output

of a single print job except in cases where tested specimens exceeded 3. Number of prints and tested specimens for each condition can be seen in Table 3.

Table 3. Number of mechanical tests and number of individual prints used to produce specimens for each condition.

Feedstock Loading (wt% magnesium)	Particle size (μm)	Number of Tested Compression Specimens	Number of Prints for Tested Compression Samples	Number of Tested Tensile Specimens	Number of Prints for Tested Tensile Specimens
0.0	N/A	5	5	4	2
1.0	< 44	9	9	3	1
2.0	< 44	5	5	3	1
3.0	< 44	3	3	3	1
3.0	< 36	3	3	6	2
3.0	36-44	3	3	3	1
4.5	< 44	3	3	3	1
6.0	< 44	3	3	3	1

Mass-loss dissolution

To evaluate the degradation speed of PEGDA-Mg composites, one compression cylinder was printed for loadings of 0, 1, 2, 3, 4.5, and 6 wt% magnesium in the feedstock. Two additional cylinders were printed at 3 wt% magnesium in the feedstock,

but with additional filtration to yield particles less than 36 μm in size and particles between 36 and 44 μm in size. The printed cylinders were then weighed, placed into separate glass vials, submersed into 20 mL of 1X phosphate buffered saline (PBS) with a pH of 7.4, and held at a temperature of 37°C for 30 days. Every five days, the cylinders were removed, patted dry, weighed, and then returned to the dissolution environment following replacement of the phosphate buffered saline with fresh material.

Chapter 4 - Results and Discussion

VPP Mixing System Design

The proposed mixing system was designed with ease of production, cost-effectiveness, chemical compatibility, and adaptability as primary objectives. The majority of the components can be additively manufactured using widely available, low-cost materials, and the assembly relies entirely on easily sourced, standardized hardware (such as M3 screws and captured hex nuts), eliminating the need for thread tapping or complex machining. The following subsections detail the design and implementation of the system on an Anycubic M3 Plus desktop VPP printer (M3P) and an Anycubic M7 Max VPP printer (M7M). For reference, a fully-assembled mixing system setup for an Anycubic M3 Plus printer, along side a 3D model of the mixing system, can be seen in Figure 3. An exploded view of the system including all major parts for this setup can be seen in Figure 4, while a further view details the subcomponents of the main mixing chamber assembly in Figure 5.

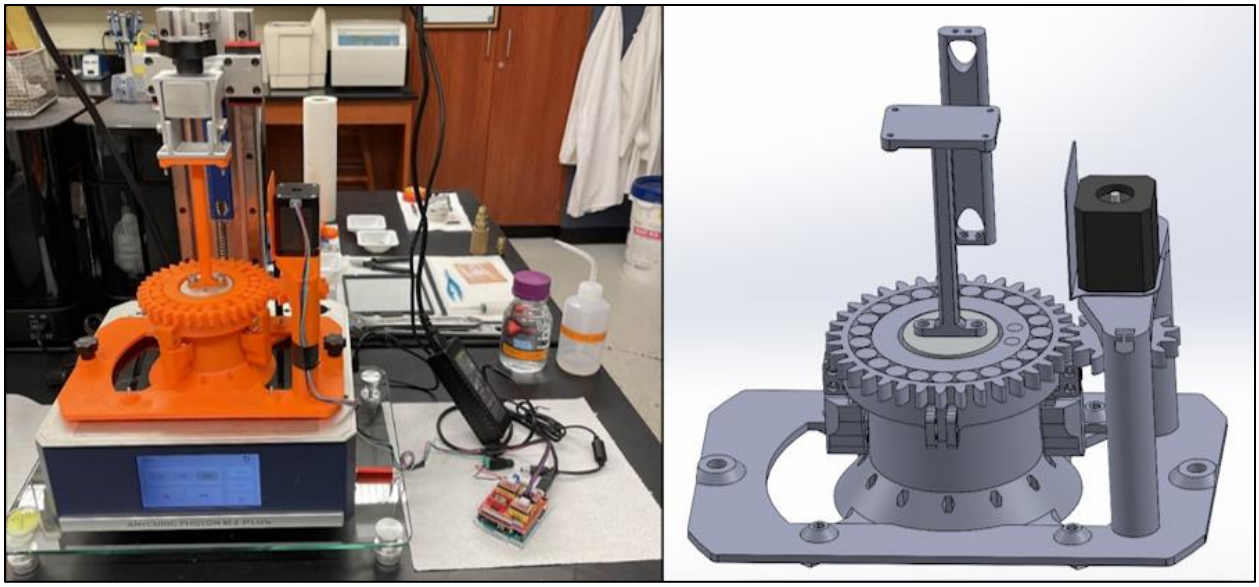

Figure 3. Fully assembled M3P printing setup with the mixing system (left) and 3D model of the mixing system and M3P printer modifications (right).

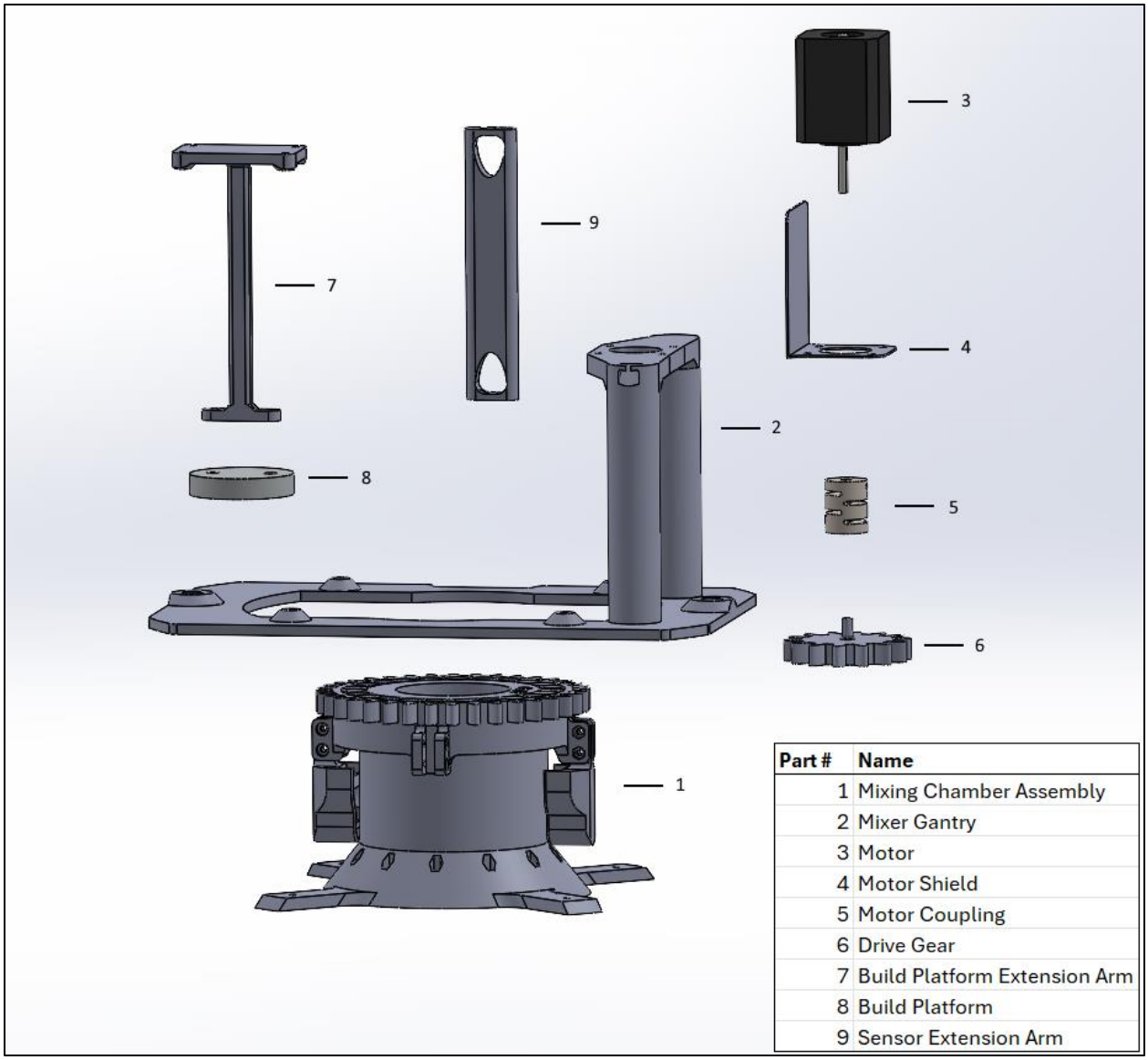

Part #	Name
1	Mixing Chamber Assembly
2	Mixer Gantry
3	Motor
4	Motor Shield
5	Motor Coupling
6	Drive Gear
7	Build Platform Extension Arm
8	Build Platform
9	Sensor Extension Arm

Figure 4. 3D rendered exploded view of the mixing system and printer modifications.

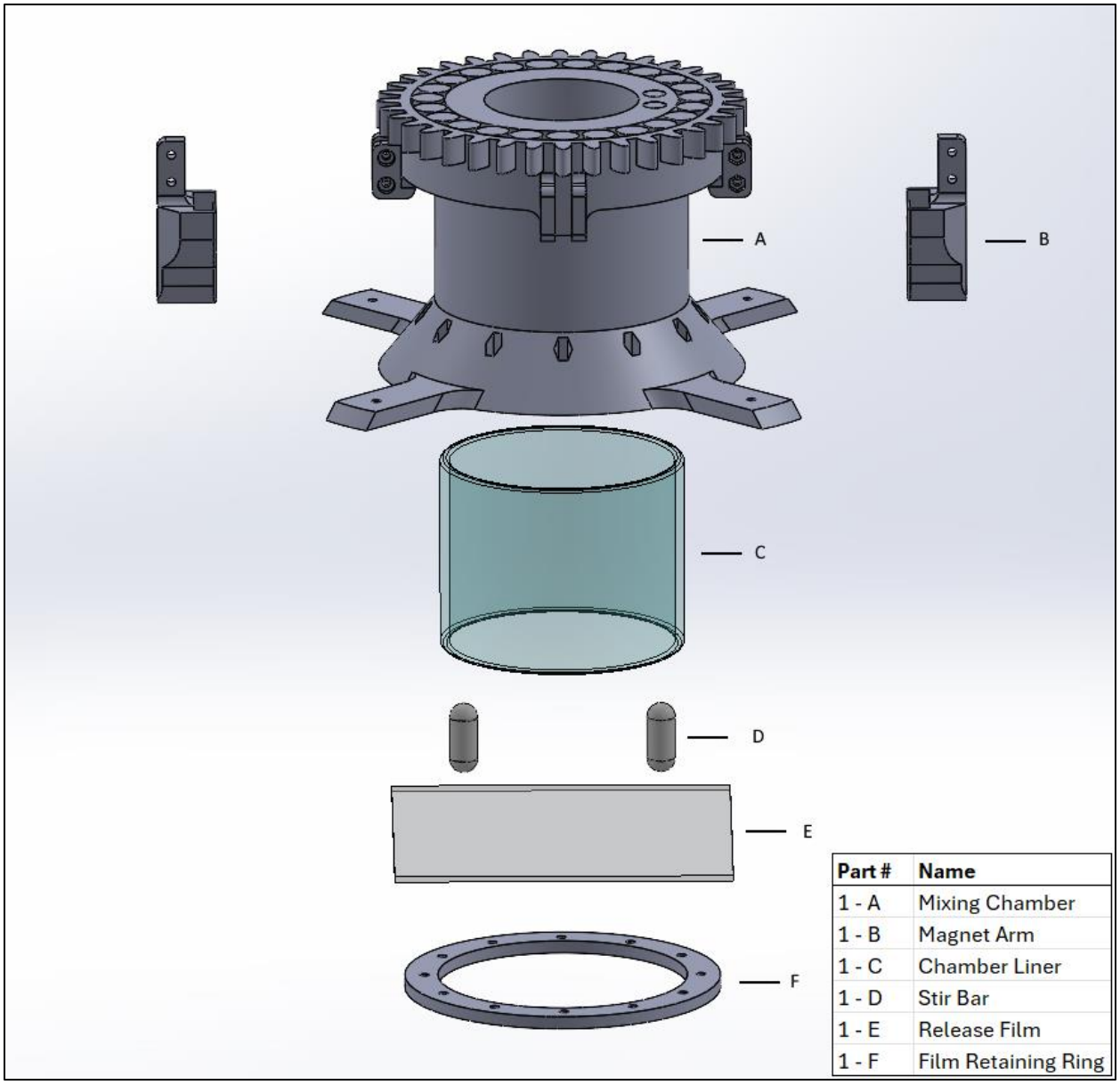

Figure 5. 3D rendered exploded view of part 1, the mixing chamber assembly, showing all sub-components.

Mixing Chamber

The design of the mixing chamber was guided by three main considerations: minimizing the possibility of turbulence-based disruption of the fabrication process, maintaining a simple and adaptable design, and ensuring wide compatibility with

conventional desktop VPP systems. For the first consideration, it was hypothesized that turbulence near the curing interface could affect layer formation during polymerization. To reduce this risk, the mixing mechanism was positioned well above the release film such that, during fabrication, the build surface can provide a physical barrier between the curing interface and the mixing mechanism. Using this setup, the chamber can be divided into a large “mixing zone” above the build platform where full agitation occurs and a confined “printing zone” below the build platform that is comparatively isolated from mixing action, particularly during the initial layers where adhesion to the build platform is established.

The second consideration was to balance the project interests of adaptability, ease of production, and mixing performance. Accordingly, the design of the mixing chamber avoided highly complex mixing geometry in favor of a simple, flat-walled cylindrical vessel that could be readily produced and replaced while still demonstrating the benefits of the process. Mixing was achieved using commercially available magnetic laboratory stir bars, which provide excellent chemical compatibility while remaining inexpensive and easily replaceable. The stir bars were driven externally by rotating permanent magnets surrounding the mixing chamber, eliminating direct contact between the drive mechanism and the feedstock.

The final consideration was compatibility with the dimensional constraints of conventional desktop VPP printing systems while maximizing the available build volume and minimizing required machine modifications. Because the circular profile of the mixing chamber is dissimilar to the typically rectangular build area of commercial VPP systems, the available build area is limited by the maximum circular diameter

achievable within the rectangular build area. Similarly, an increase in chamber height, compared to a conventional wide and shallow resin vat, reduces the available build height within the attached printing system and motivates towards minimizing the vertical size of the system.

The tested mixer body was designed as a hollow cylindrical chamber with an internal diameter of 80 mm and a height of 65 mm, shown with a cross-section in Figure 6. This chamber serves as the feedstock reservoir during printing. The chamber diameter was selected to accommodate the build area available in many common desktop VPP systems, while the chamber height was set at the minimum necessary to provide sufficient space for the external drive components, thus maximizing the available build height within the system. To provide interchangeability and chemical compatibility, the mixing chamber is separated from the rest of the structure by a 3.5 mm thick cylindrical liner (part 1-C) composed of borosilicate glass. two laboratory stir bars (part 1-D) are placed within and a release film (part 1-E) is mounted and sealed over the bottom edge of the chamber to serve as the printing surface. The release film is secured using a retaining ring (part 1-F), which is similar to the film attachment methods commonly used in commercial printing systems. The stir bars used in testing were polytetrafluoroethylene coated, 25.4 mm in length, 9.5 mm in diameter and polygon-style, without a pivot ring, obtained from VWR. The release film used was 0.15-0.20 mm thick FEP film obtained from Koyofei. In this configuration, the mixer body only has three components which are in significant contact with the feedstock: the release film, the stir bars, and the liner. Each of these components can be readily sourced out of a variety of materials and easily replaced as needed.

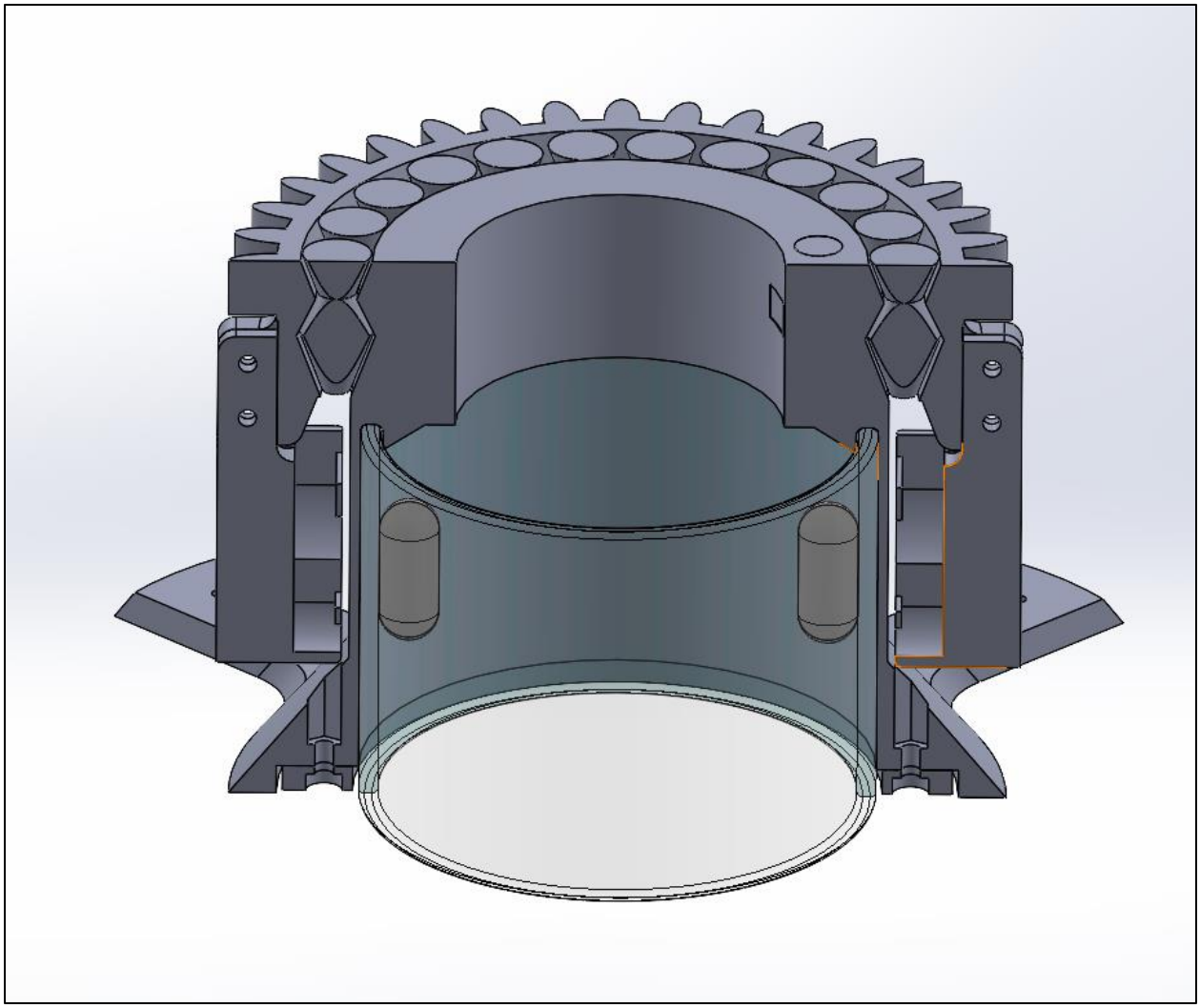

Figure 6. 3D rendered cross section of the mixing chamber assembly, release film not pictured.

Mixing is achieved using several pairs of permanent magnets that are mounted onto an externally-driven gear-toothed bearing. Though the bearing is designed to support up to four magnet pairs, testing on the M3P was conducted using only two sets and two stir bars, spaced 180° apart, while testing on the M7M utilized all four sets and stir bars, spaced 90° apart. One of the arms used to mount the magnets externally (part 1-B) is shown in Figure 7. The permanent magnets in each arm were circular, neodymium magnets of sizes 25 mm in diameter and 2 mm in thickness (Obtained from

MAGXCENE) and 12 mm in diameter and 1.5 mm in thickness (Obtained from TRYMAG). Within each arm, the magnets were mounted in stacks to each achieve an effective thickness of 6 mm and paired such that the larger magnets and the adjacent smaller magnets were presenting opposite poles towards the mixing chamber. In this orientation, the magnets each couple with one pole of the stir bar inside the chamber, holding it into a single, vertical, orientation against the chamber wall. Rotation of the bearing causes the magnetically coupled stir bars to rotate along the chamber wall, driving mixing activity within the system. This configuration minimizes any direct interaction between the drive components and the photopolymer resin. As a result, standard laboratory stir bars are the only drive component which contacts the feedstock. Due to selecting the system height to be as small as possible and due to the geometry of other necessary components, the stir bars could only be mounted at a single height, suspended in a vertical orientation with the mid-point of the bar held approximately 42 mm above the release film.

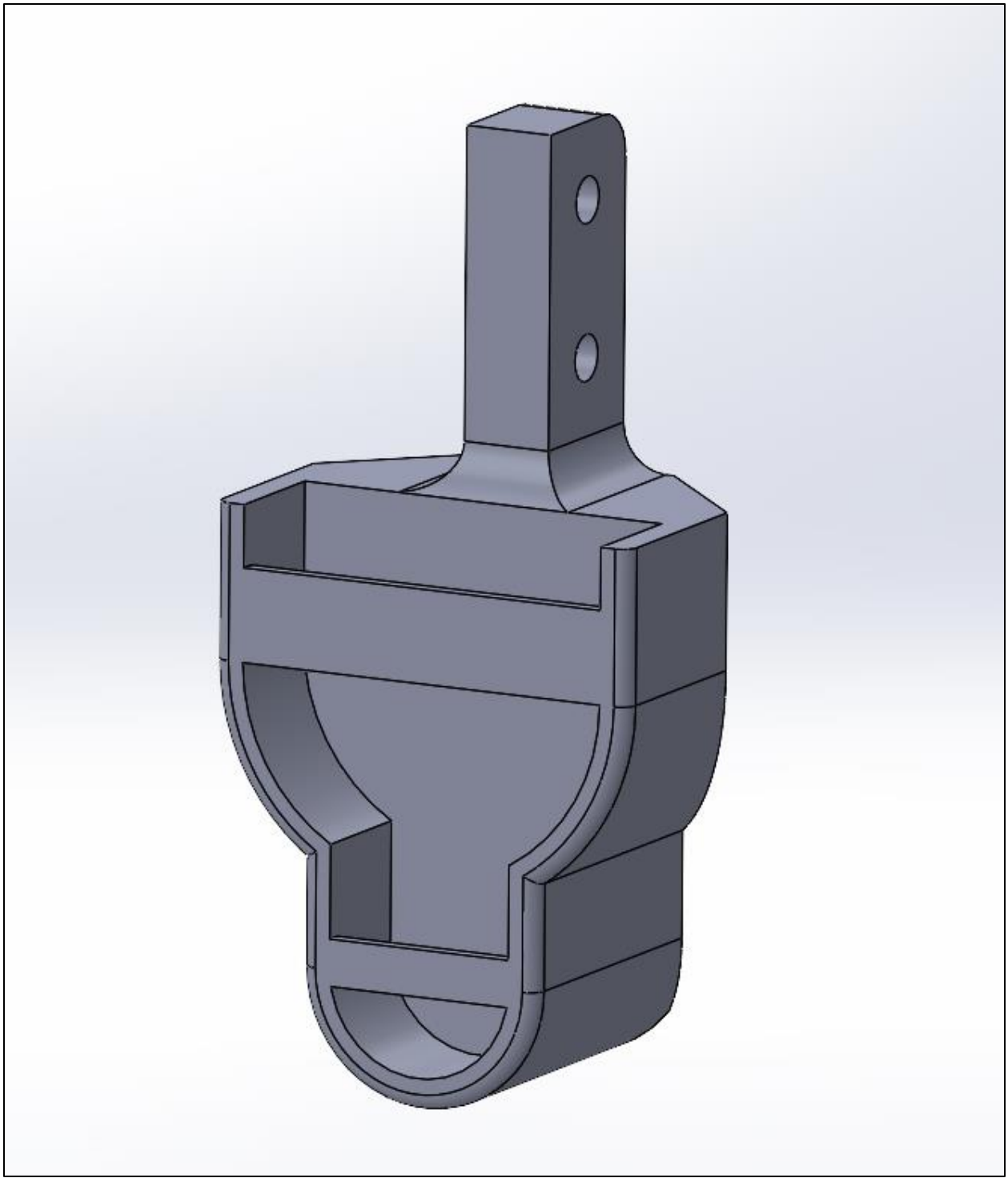

Figure 7. 3D rendered example of an external magnet arm.

During printing, the center of the cylindrical mixing chamber is occupied and periodically disturbed by the build platform. Consequently, fluid motion is governed by a combination of the wall-driven agitation, vertical translation of the build platform, and, critically, the evolving geometry of the printed part. Assuming that the magnetic stir bars are powered in a constant, single-direction rotation throughout printing, a vortex is expected to form above the build platform during polymerization and then be disturbed during the subsequent lifting motion of the build platform. However, as printing continues, the position of the build platform relative to the chamber changes continuously as the printed model grows larger. As a result, the geometry of the printed part continuously becomes more relevant for the flow behavior within the chamber. This dependence, combined with the change in build platform position, leads to time-variant flow conditions that depend on the geometry of the printed part and complicate the application of fluid modeling to predict system performance. Given the cylindrical nature of the chamber, stagnation zones are expected to occur primarily within the printing zone during polymerization and at the interface between the chamber wall and the release film, but may be heavily disturbed by the regular motion of the build platform.

The Reynolds number for the mixing system can be estimated using the reported properties of commercial VPP feedstock materials, which typically indicate viscosities within the range of 0.15 Pa·s to 2.00 Pa·s (μ) and densities (ρ) between 1.00 and 1.25 g/mL. Rheological information on commercial resins is limited, but materials are reported as generally near-Newtonian and otherwise often best performing when demonstrating only minor non-Newtonian behavior [74]. As a result, fluids are assumed to be Newtonian for this calculation and comparison. Assuming an applied rotational

speed of 250 rpm, equating to 4.17 rps (N), and a characteristic impeller diameter of 80 mm (D) for the wall-driven mixing system, the Reynolds number is estimated using expression (1) for impeller driven flow within a cylindrical mixing chamber.

$$Re = \frac{\rho N D^2}{\mu} \quad (1)$$

Under these conditions, the system is estimated to operate within the transitional mixing regime for many commercial resins, with Reynolds number values ranging approximately from 13 to 222 depending on fluid properties.

For comparison, composite feedstock preparation in literature commonly relies on mechanical stirring for initial homogenization [75-77], often specified as simple magnetic stirring [14, 78-82]. Assuming a representative stir bar size of 25 mm, a speed of 800 rpm, the same properties common to commercial VPP feedstocks, and expression (1), these systems yield a range of Reynolds numbers approximately between 6 and 100. Based on these comparative estimates, the developed mixing chamber provides mixing conditions comparable to, or more intense than, the environments typically used for pre-print homogenization.

Printer Attachments and Modifications – M3P

In order to attach the mixer system to a conventional VPP printer, four main components are required: a supporting frame to hold the mixer to the printer (part 2) hereafter referred to as the gantry, a build platform extension arm (part 7), a specially shaped build platform (part 8) and a sensor extension arm (part 9). The gantry is primarily responsible for securely fixing the position of the mixer body to the used VPP system and supporting the motor and drive system as well. For the design used for the

M3P printer, the gantry was connected to the mixing chamber via four mounting flanges which extend out from the bottom of the chamber. Then, the Gantry could itself be affixed to the used printer via the two mounting thumbscrews which normally hold the traditional resin vat in place.

Due to the shape of mixer, a specially shaped build platform with a diameter of approximately 50mm is required for operation. In this work, the build platform consisted of a circular section cut from a consumer aluminum build surface produced by Anycubic. Because the mixer body extended significantly above the form factor of conventional resin vats, an extension arm, shown in Figure 8, was needed to offset the build platform sufficiently such that the Z-axis carriage of the printer did not interfere with the mixer body during operation. The used platform extension arm provided an offset of 130mm compared to the original height of the build platform relative to the Z-axis carriage. To increase the tolerances allowable in part production and assembly, the design of the extension arm preserved the build platform mounting and leveling system of the original printer.

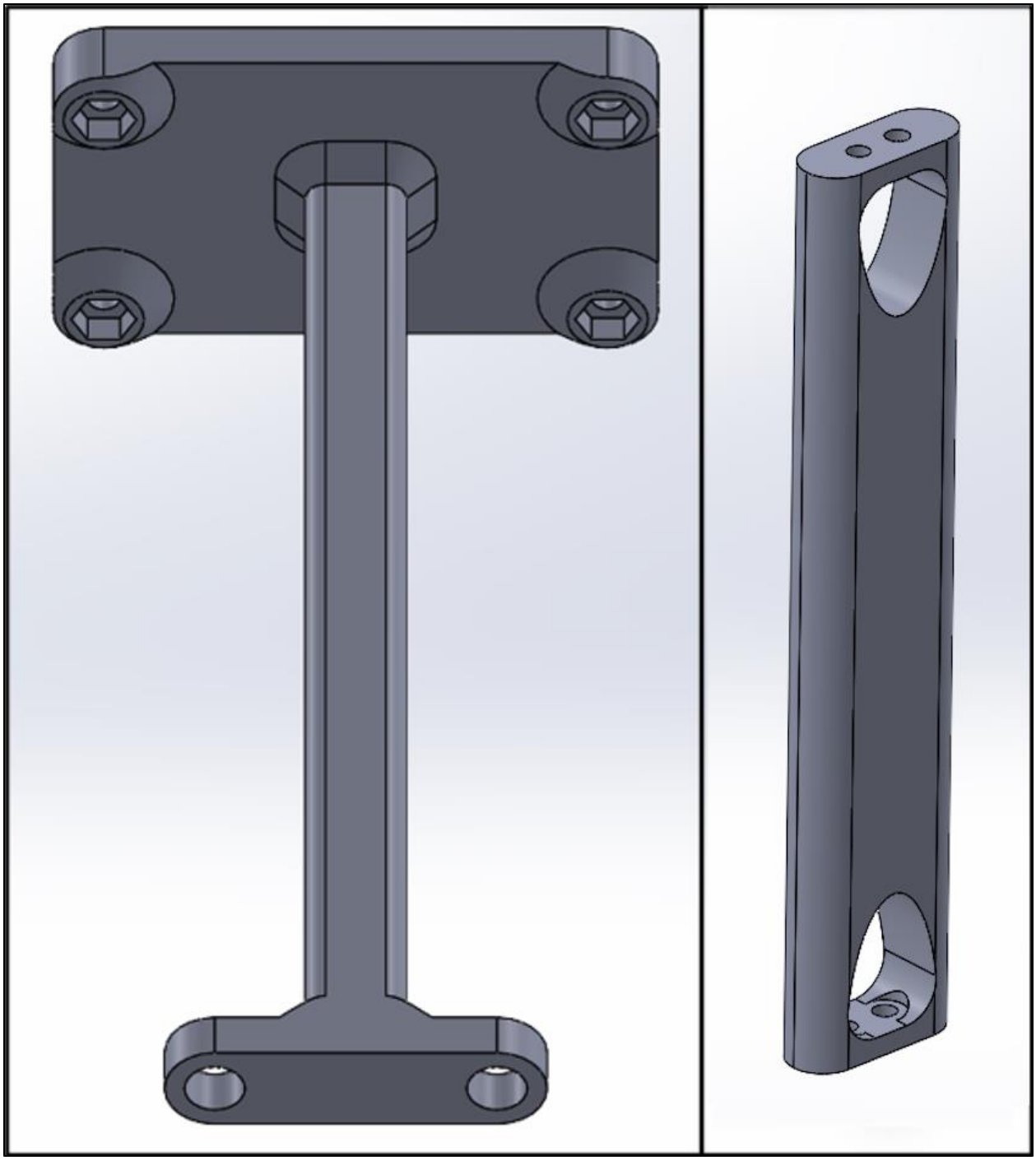

Figure 8. 3D models of a build platform extension arm (left) and sensor extension arm (right).

The introduction of the build platform extension arm necessitated a corresponding sensor extension arm, example also shown in Fig. 6, to appropriately

activate the z-axis end stop sensor at the corrected height of the build platform. In general, this sensor arm should provide the same effective offset as the build platform extension, though leveling adjustment systems can allow for significant tolerances between the two offsets.

In this work, a NEMA 17 pattern stepper motor (part 3), controlled by an Arduino Uno Rev3 and a A4988 stepper driver, was used to provide continuous rotation at precise speeds. Because stepper motors are driven in discrete step pulses, the rotation speed can be regulated through software without requiring closed-loop feedback mechanisms or rotary encoders, thereby minimizing setup cost and difficulty. Though not necessary for operation, a small shield (part 4) was added to protect the motor from any contact with the feedstock during the removal of the build platform. To provide power to the toothed-bearing and perform mixing, the motor is coupled (part 5) to a small drive gear (part 6). The standard gearing of the toothed-bearing uses 36 teeth and was matched to the drive gear in a 18:7 (bearing : drive) gearing ratio. A smaller drive gear was selected to help avoid low-speed stepper resonance by allowing the motor to remain at a significantly higher speed than the mixing chamber.

Printer Attachments and Modifications – M7M

In comparison to the simplified variation for the M3P, the reinforced version of the mixer attachments used for the M7M still have the same four main components: a supporting frame, or gantry, to hold the mixer to the printer, a build platform extension arm, a specially shaped build platform, and a sensor extension arm. The reinforced gantry, shown in Figure 9, is instead composed of several pieces, allowing more

interchangeability and production using printers with smaller build volumes. Otherwise, the reinforced gantry also features several major revisions to the drive system. In the simplified version, high torque motors operating at high speed creates a significant torque on the gantry, leading to flexing and a loss of performance if the flexing causes the mechanical components to jam. In order to address this, the new system uses the upper attachment interfaces to secure the gantry to the mixing chamber at the top as well, lowering the significance of flexure, while also incorporating a separate driveshaft supported by small commercial bearings on both sides, shown in Figure 10, limiting the flexure which could result from the drive gear being directly attached to only the motor. As a result of these improvements and the goal of mixing at speeds above 250 rpm, the gearing ratio was also changed to be 1:1, using the same motor and control system as the M3P system. This leads to a more significant risk of low-speed stepper resonance, but also affords a greater top speed as stepper motors lose torque at higher rates of rotation. Lastly, a removable cap, shown in Figure 11, was added around the build platform arm to minimize any chance of the feedstock splashing out of the mixing chamber under high agitation conditions. An exploded view of the various parts of the new drive system can be seen in Figure 12.

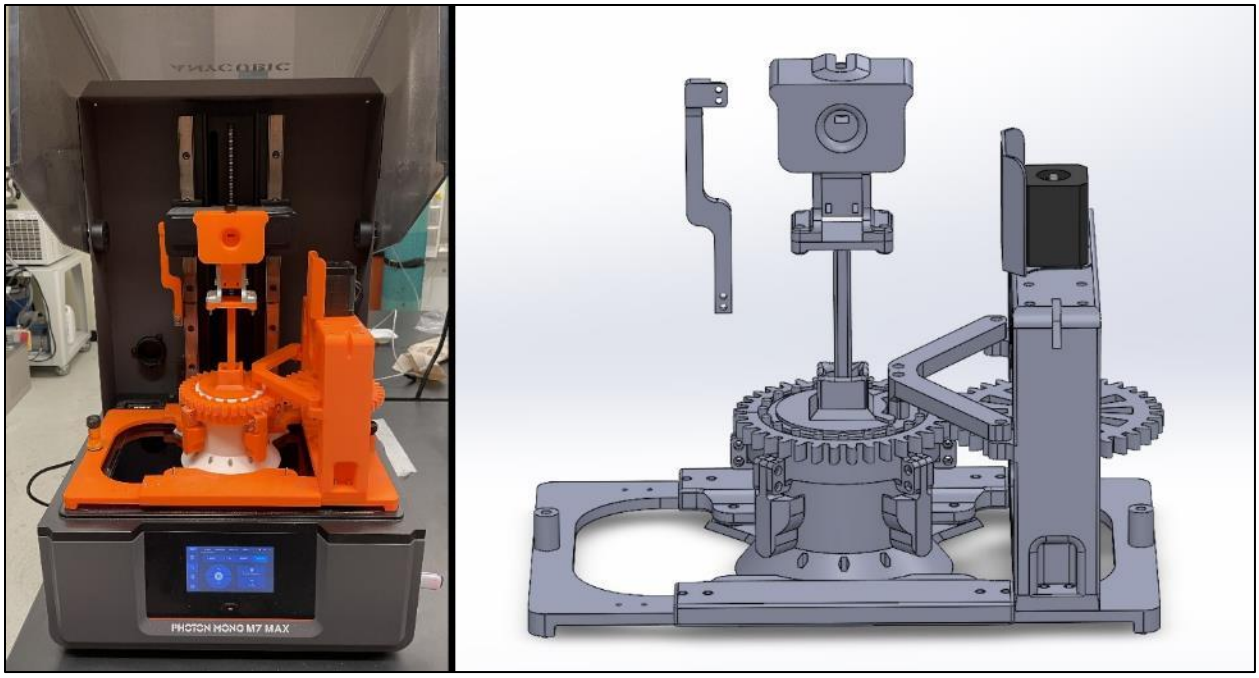

Figure 9. Fully assembled mixing system attached to printer M7M-1 (left) and 3D model of the mixing chamber and M7M adapters (right).

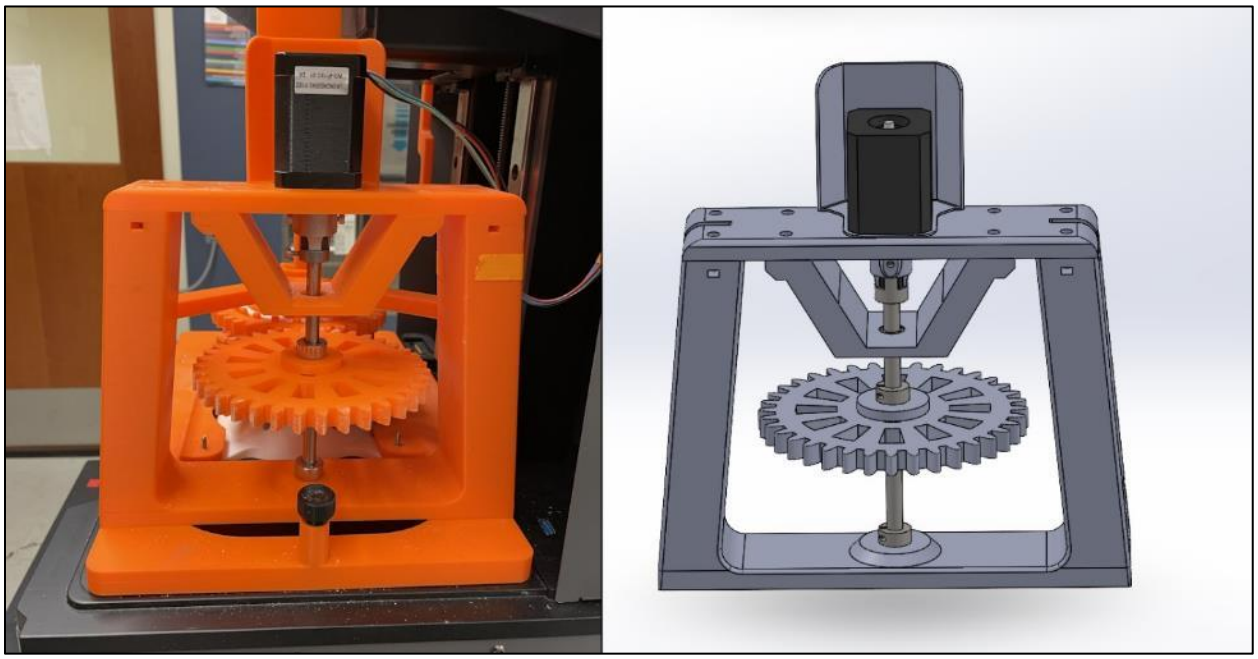

Figure 10. Side view of the drive system for M7M adapter setup (left) and 3D model of the detached drive system (right).

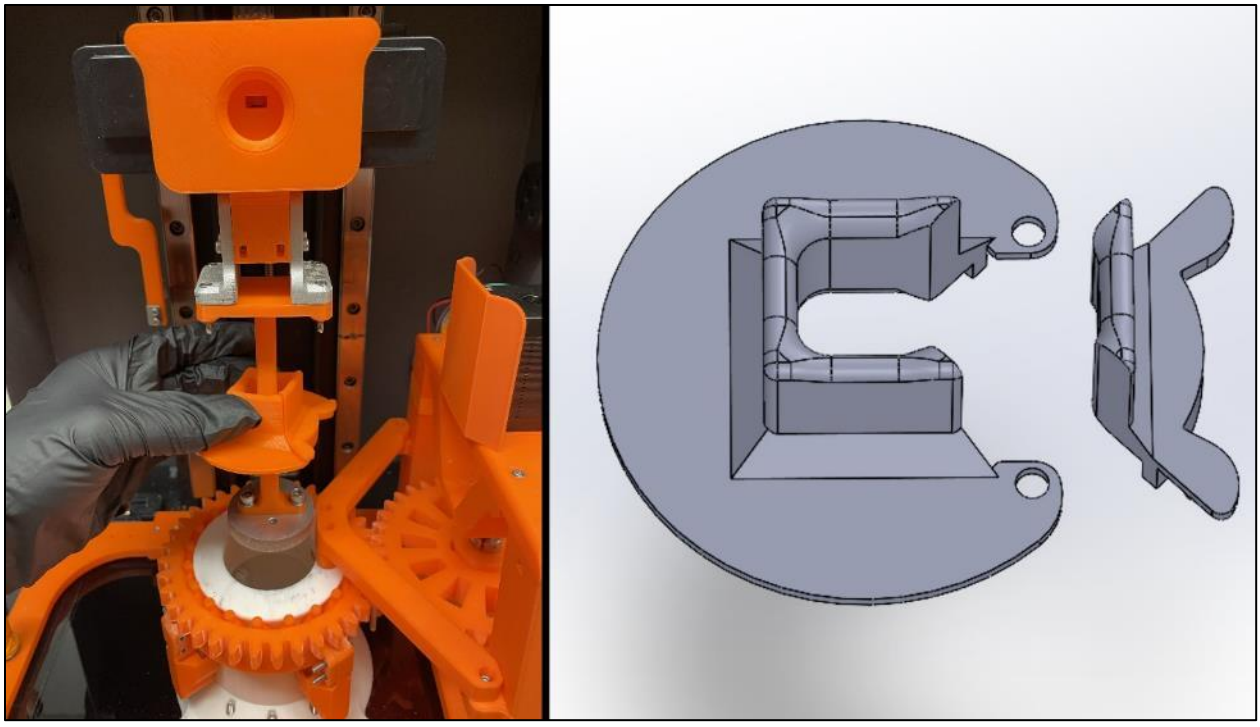

Figure 11. Mixing chamber cap attached to build platform extension arm (left) and as 3D model (right).

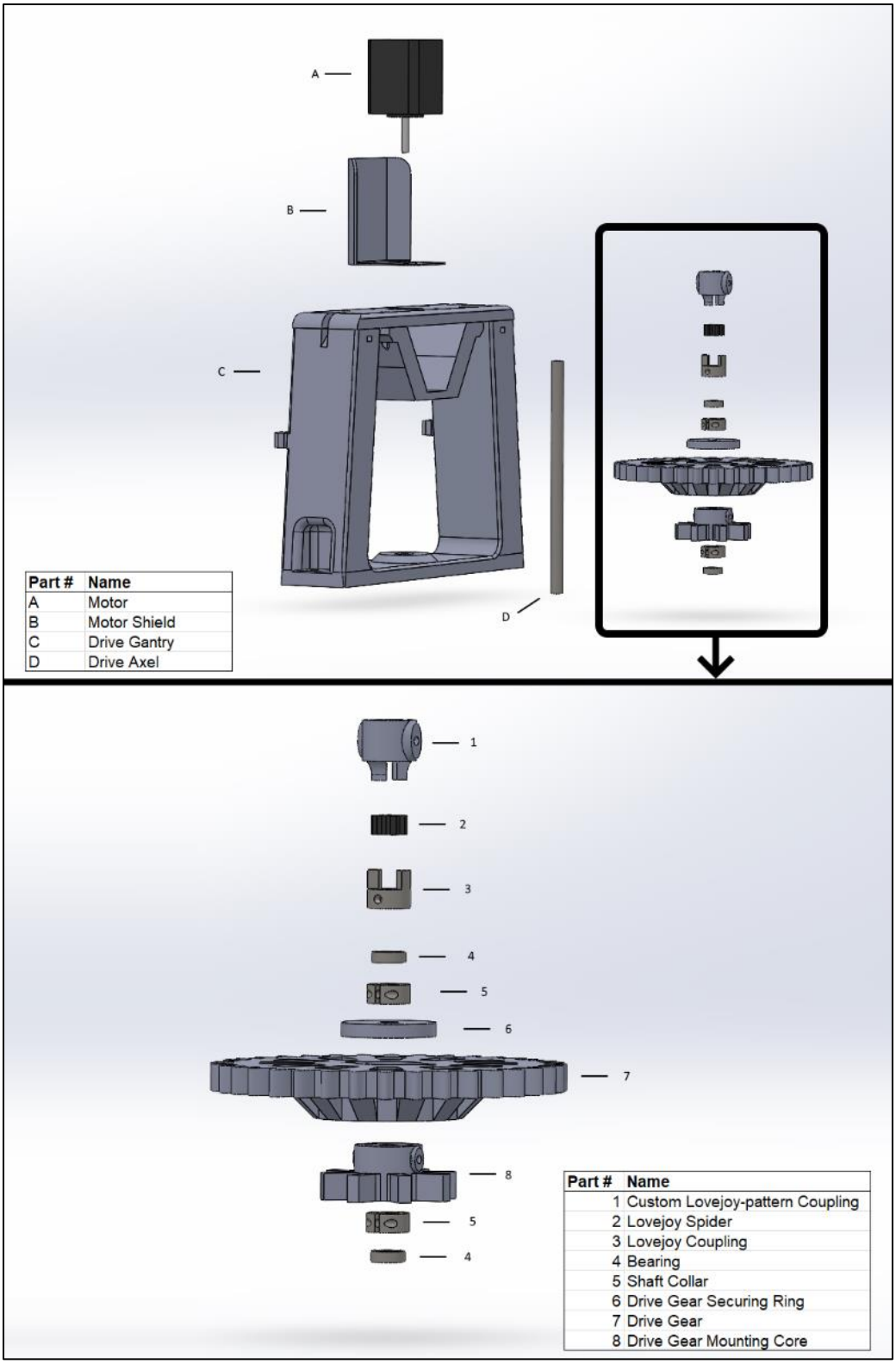

Part #	Name
A	Motor
B	Motor Shield
C	Drive Gantry
D	Drive Axel

Part #	Name
1	Custom Lovejoy-pattern Coupling
2	Lovejoy Spider
3	Lovejoy Coupling
4	Bearing
5	Shaft Collar
6	Drive Gear Securing Ring
7	Drive Gear
8	Drive Gear Mounting Core

Figure 12. Breakdown and exploded view of the M7M drive system.

Similarly, the original bearing design prioritized ease of assembly, but the tolerances needed to successfully print an all-in-one bearing design on available equipment meant that the final part was not tightly fitted, allowing some wobble in the bearing as it rotated. At speeds at or below 250 rpm, this effect was minimally impactful. However, at high speed, this became a significant source of energy loss and drag, requiring more energy to turn and causing issues with reliability as a result. To compensate, the bearing was redesigned to be produced in several pieces and assembled later, allowing much more freedom to iterate on roller dimensions with the goal of producing a much more tightly fitted bearing. For reference, the original bearing experienced an angular misalignment during rotation of approximately +/- 0.5° between the inner and outer rings. Due to its size, this translates to approximately +/- 1 mm in the vertical positioning of the outer components. In the new bearing design, shown in Figure 13, no angular misalignment could be detected macroscopically.

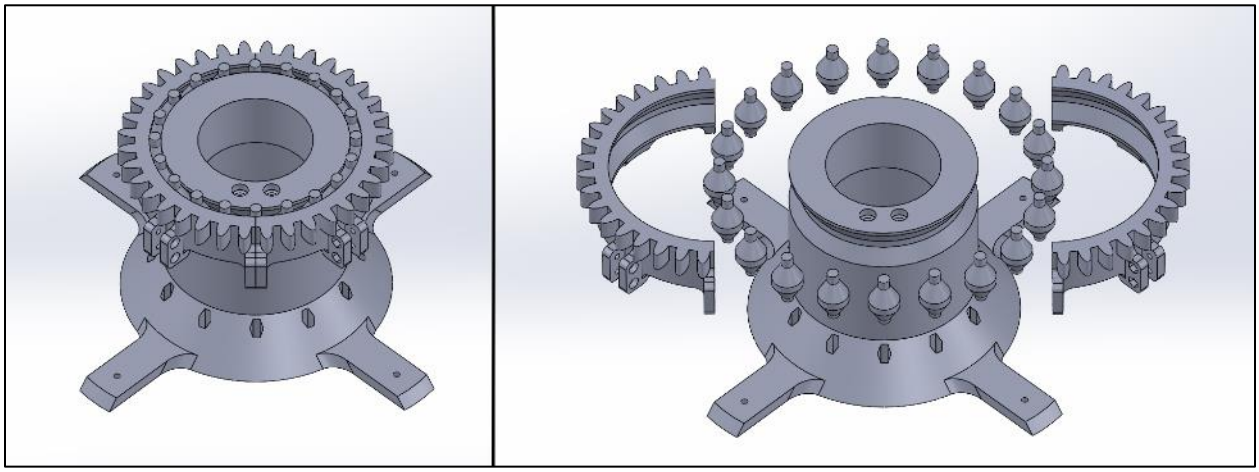

Figure 13. The revised bearing attached to the mixing chamber (left) and exploded view of the bearing halves and rollers (right).

The build platform and extension arm used for this new design was unmodified from those designed for the M3P. However, the new printer did not support the same attachment geometry and required a replacement attachment interface to match the pre-existing designs, incorporating a simple replacement leveling system as well. Lastly, the sensor arm, shown in Figure 14, required a different geometry due to the difference in sensor placement in the M7M, but otherwise served the same purpose.

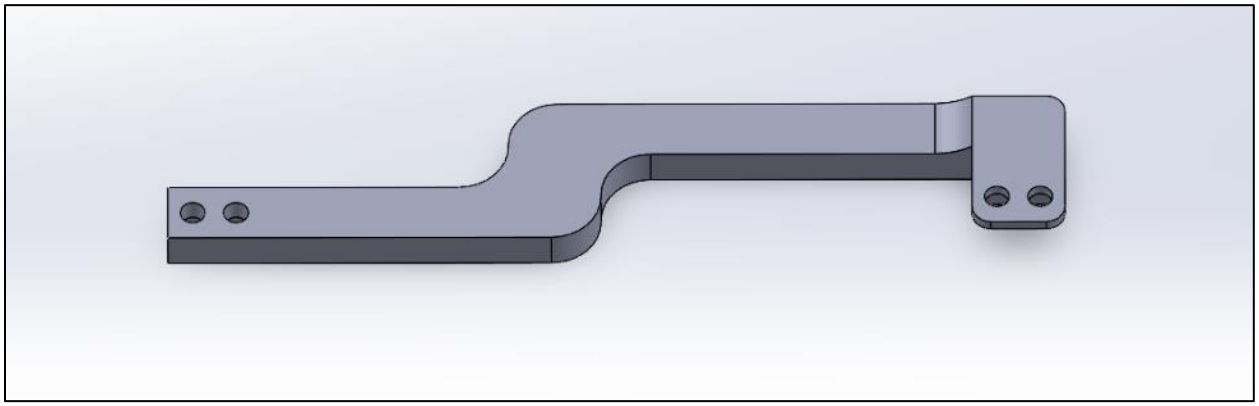

Figure 14. 3D model of the M7M Sensor offset arm.

Quality of Printed Parts

The printed quality model for each condition can be seen in Figure 15 and Figure 16, while the measurements taken of each model can be seen in Table 4. The percent error of those measurements from the real values can be seen in Table 5 along side the calculation of the average absolute percent area for each condition.

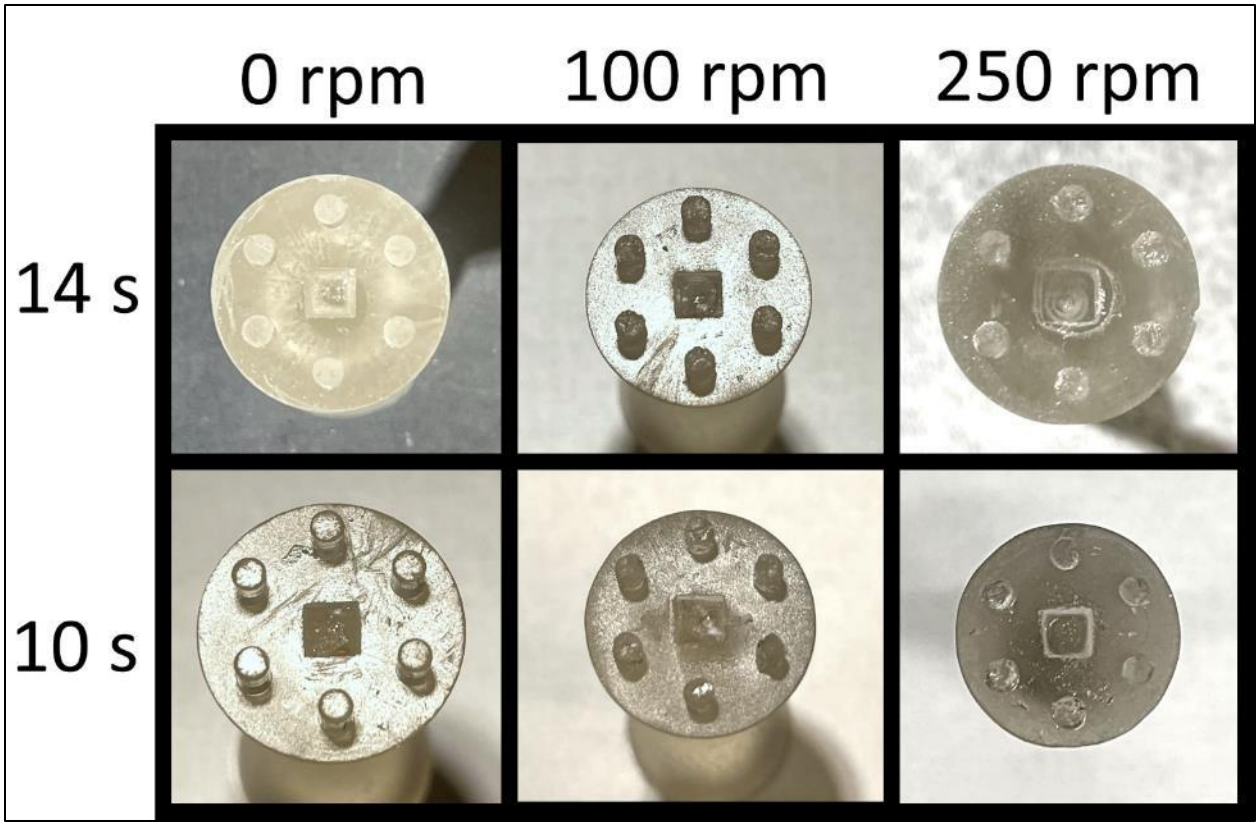

Figure 15. Top view of quality models produced on printer M7M-1, at different indicated mixing speeds and layer exposure times.

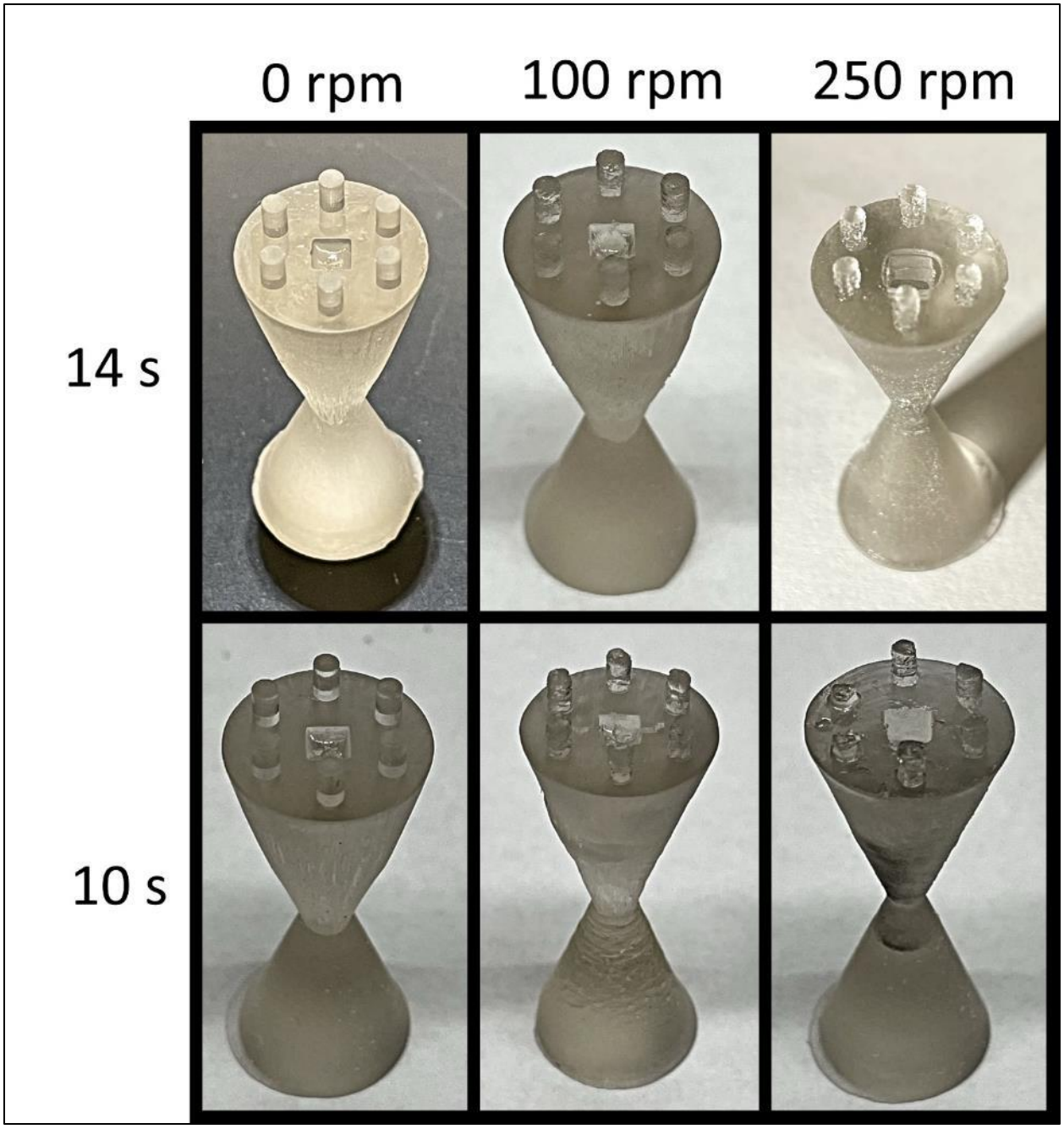

Figure 16. Overall view of quality models produced on printer M7M-1, at different indicated mixing speeds and layer exposure times.

Table 4. Measured dimensions of quality models produced on printer M7M-1.

Mixing Speed (rpm)	As-Designed	0	100	250	0	100	250
Exposure Time (s)	As-Designed	10	10	10	14	14	14
Height of Hourglass (mm)	35.0	34.1	33.9	34.3	34.1	33.7	34.1
Diameter of Hourglass Top (mm)	15.0	14.7	14.5	14.5	14.7	14.7	14.6
Diameter of Hourglass Narrow Point (mm)	3.0	4.05	3.66	2.83	4.78	4.04	2.98
Diameter of a Small Cylinder (mm)	2.0	1.83	1.86	1.68	1.92	1.91	1.82
Height of a Small Cylinder (mm)	3.0	3.07	2.94	2.97	2.99	3.05	2.87
Square Cut-in Wall Length (mm)	3.0	2.94	3.04	3.03	2.94	2.98	3.02
Square Cut-in Depth (mm)	3.0	1.26	1.62	3.38	1.18	1.78	3.07

Table 5. Percent error of measured dimensions of quality models produced on printer M7M-1.

Mixing Speed (rpm)	0	100	250	0	100	250
Exposure Time (s)	10	10	10	14	14	14
Height of Hourglass (%)	-2.60	-3.23	-2.14	-2.54	-3.80	-2.63
Diameter of Hourglass Top (%)	-2.00	-3.20	-3.53	-1.73	-2.00	-2.73
Diameter of Hourglass Narrow Point (%)	35.00	22.00	-5.67	59.33	34.67	-0.67
Diameter of a Small Cylinder (%)	-8.50	-7.00	-16.00	-4.00	-4.50	-9.00
Height of a Small Cylinder (%)	2.33	-2.00	-1.00	-0.33	1.67	-4.33
Square Cut-in Wall Length (%)	-2.00	1.33	1.00	-2.00	-0.67	0.67
Square Cut-in Depth (%)	-58.00	-46.00	12.67	-60.67	-40.67	2.33
Average Absolute Percent Error (%)	15.78	12.11	6.00	18.66	12.57	3.19

In quality tests produced at 250 rpm and with a 10 second exposure time, some of the small cylinders detached after successfully printing approximately 1 mm. The same behavior was not found within the 14 second exposure time prints, indicating this may be a result of the lowered exposure. Prints at 250 rpm demonstrated noticeable surface roughness on the successful small cylinders, though the dimensions remained generally accurate to the design parameters. Lower speed tests, conversely,

demonstrated significant polymerization outside of intended zones, leading to the narrow section of the hourglass being printed larger than indicated and the square cut-in being filled almost entirely with solid polymer. This behavior is present even under static conditions, indicating it is more related to the performance of the feedstock than to the performance of the mixer system. However, this behavior was also most severe under static conditions, becoming almost unnoticeable at 250 rpm. Based on this, the mixer may also have some utility for arresting unintended polymerization, also known as overcuring, by disrupting unintentionally-exposed zones through turbulence without requiring the addition of a UV absorber, as would be the common solution to this problem in industry. Ultimately, a small loss in dimensional accuracy of fine positive elements was noted when increasing mixing speed, but an increase in the dimensional accuracy of negative elements was also noted. As a result, excluding the loss of the small cylinders in the 10 second exposure condition, the highest mixing speed conditions demonstrated the lowest average inaccuracy of printed dimensions.

Simulation Results

An example of one of the generated particle-volumes is shown in Figure 17. The results of all 10^6 measurements for each condition were averaged to produce the final expected value for each particle loading, shown in Figure 18. The dependence on particle size that was observed in the simulation results indicated the expected diversion from Delesse's principle despite identical weight fractions. For evaluation of printed specimens, a mean particle size of 25 μm was selected as this condition produced particle sizes closest to the distribution observed during microscopy and additional

simulation was conducted up to 20 wt%, shown in Figure 19. The full range of simulation results, 0.1 – 20.0 wt%, was found to closely fit linear behavior and the line of best fit was used to determine an equation relating measured area percentage to likely loading quantity of the bulk material in weight percent, shown in expression (2).

$$wt\% = \frac{area\%+0.0999}{0.8999} \quad (2)$$

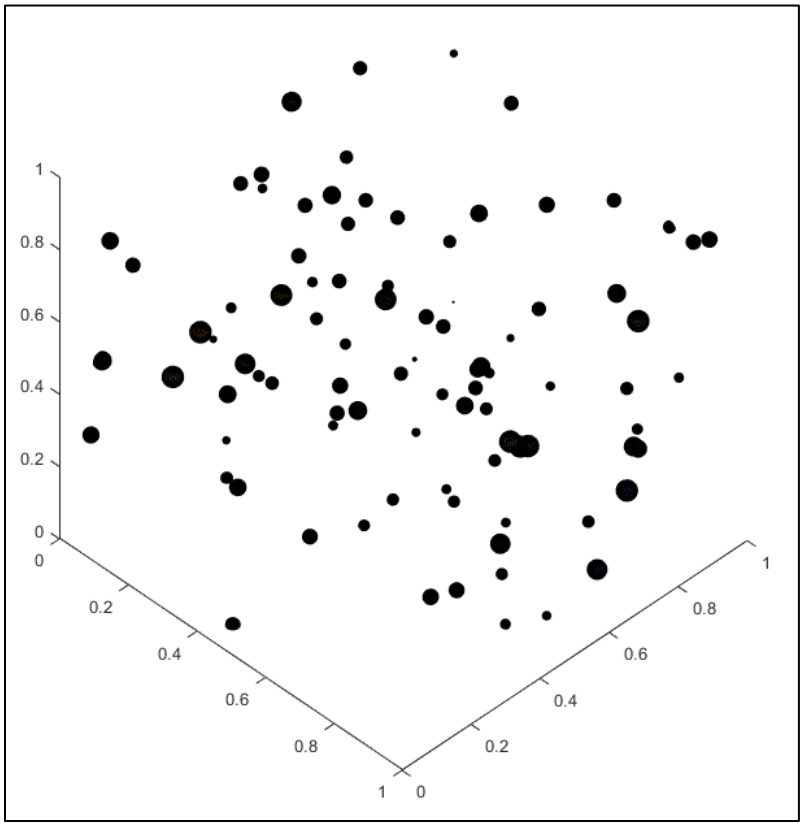

Figure 17. Example of simulated 1 mm^3 particle volume.

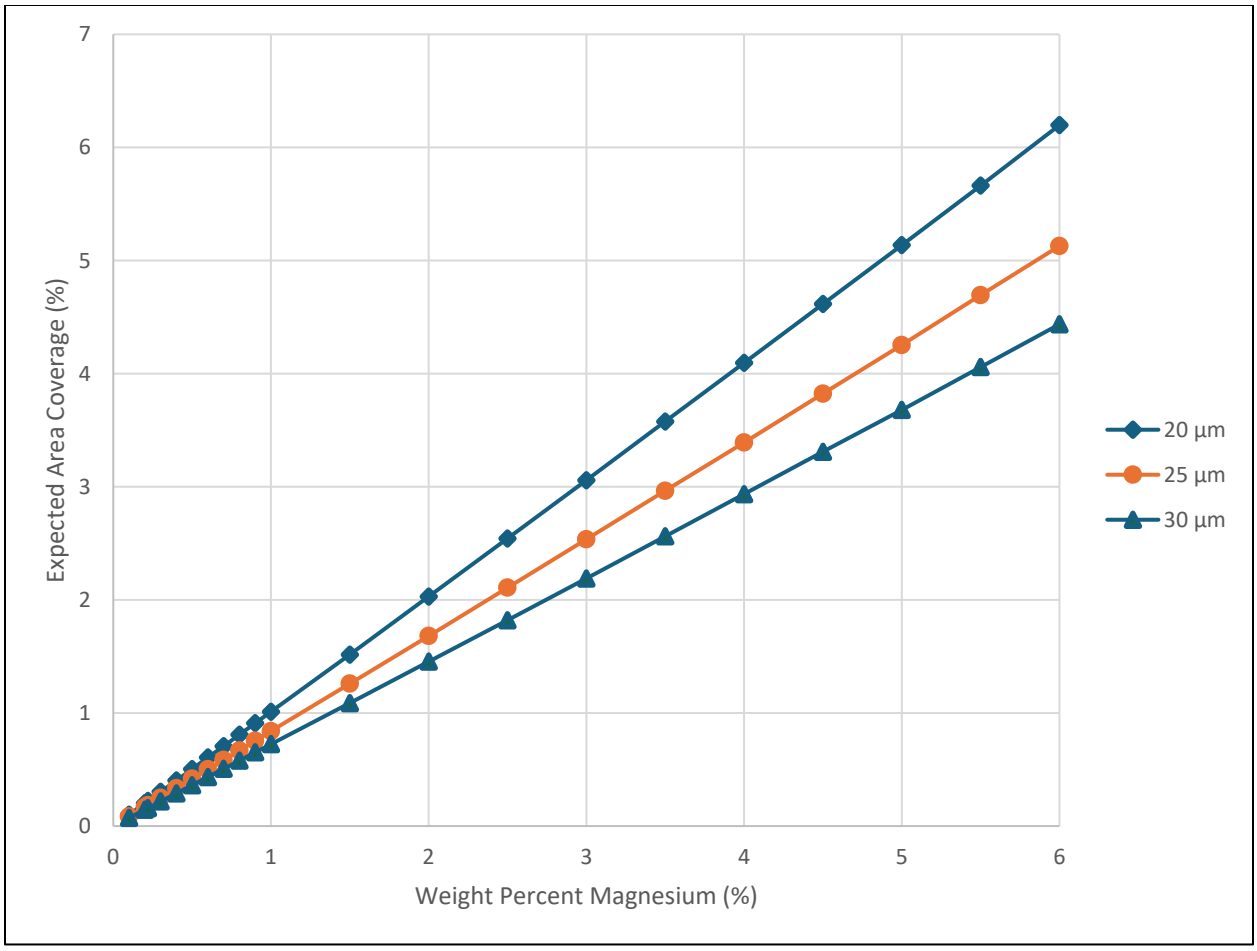

Figure 18. Simulation-predicted area fraction coverage of magnesium particles versus the weight-percent loading and for average particle sizes of 20, 25, and 30 µm.

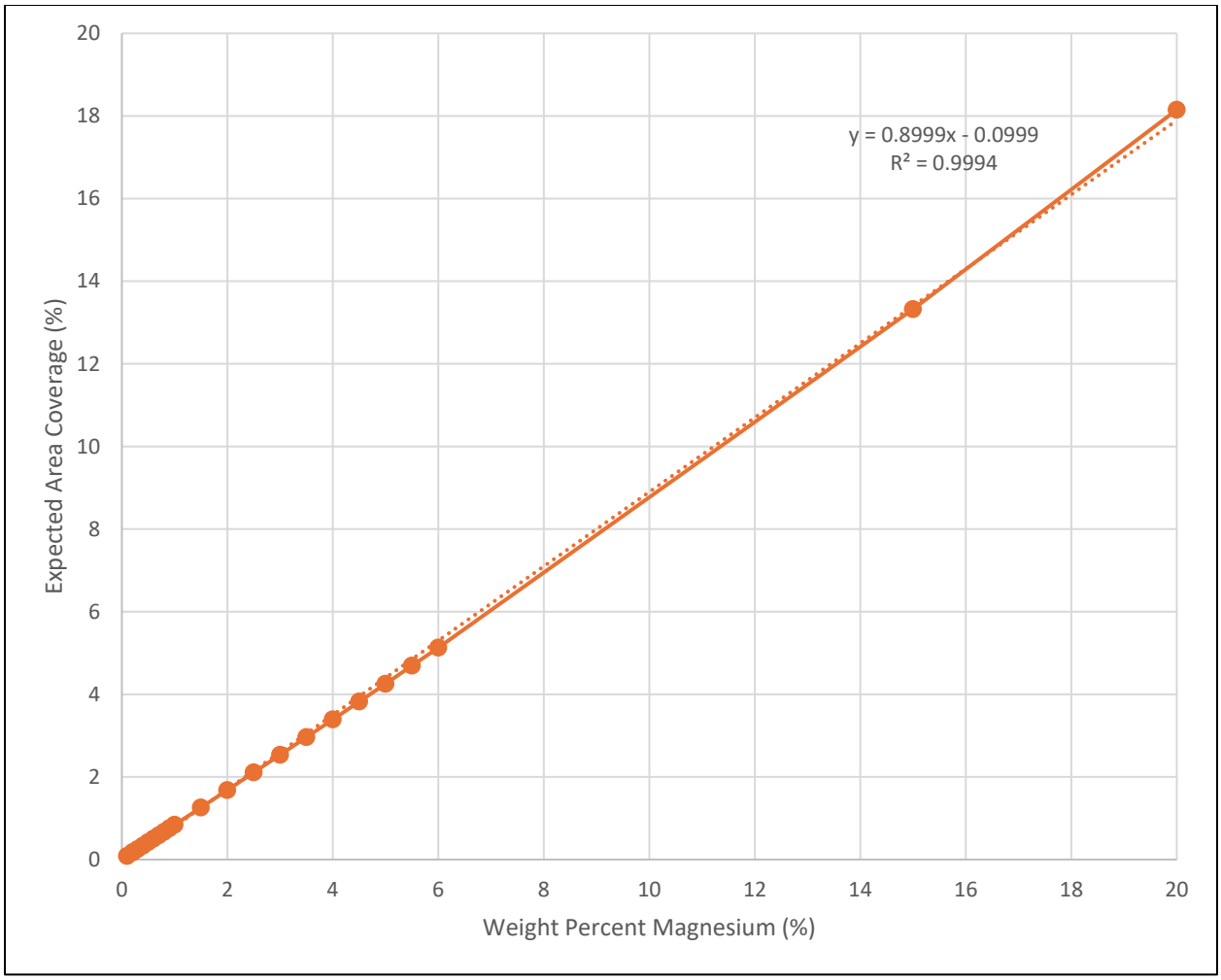

Figure 19. Extended simulation-predicted area fraction coverage of magnesium particles versus the weight-percent loading for an average particle size of 25 µm.

Gravimetric Settling and Static Printing

Results from the gravimetric settling experiment can be seen in Figure 20, including a basic Stokes' law fit to the earliest data points. Gravimetric settling indicated that more than 40% of the added material was expected to settle out of suspension in just 30 minutes. Given that most printing processes take several hours at least, this confirms that settling with this system is rapid enough to be relevant during printing and

is likely to be a significant issue under static conditions. The Stokes' law approximation was derived based on expression (3), defining the terminal velocity (v_t) of settling particles based upon the density of the particles (ρ_p), the density of the fluid (ρ_f), the dynamic viscosity of the fluid (μ), gravity (g), and the radius of the settling particles (R). As exact information on the particle size range and viscosity of the printing material was not available, the fit was performed using a single particle size of 25 μm (R = 12.5 μm) and controlling viscosity to match most closely to the earliest data points. Though insufficient for describing the full range of different particle sizes, this fit was able to be predictive of the behavior of about 40% of the particles in this experiment.

$$v_t = \frac{2}{9} * \frac{\rho_p - \rho_f}{\mu} * g * R^2 \quad (3)$$

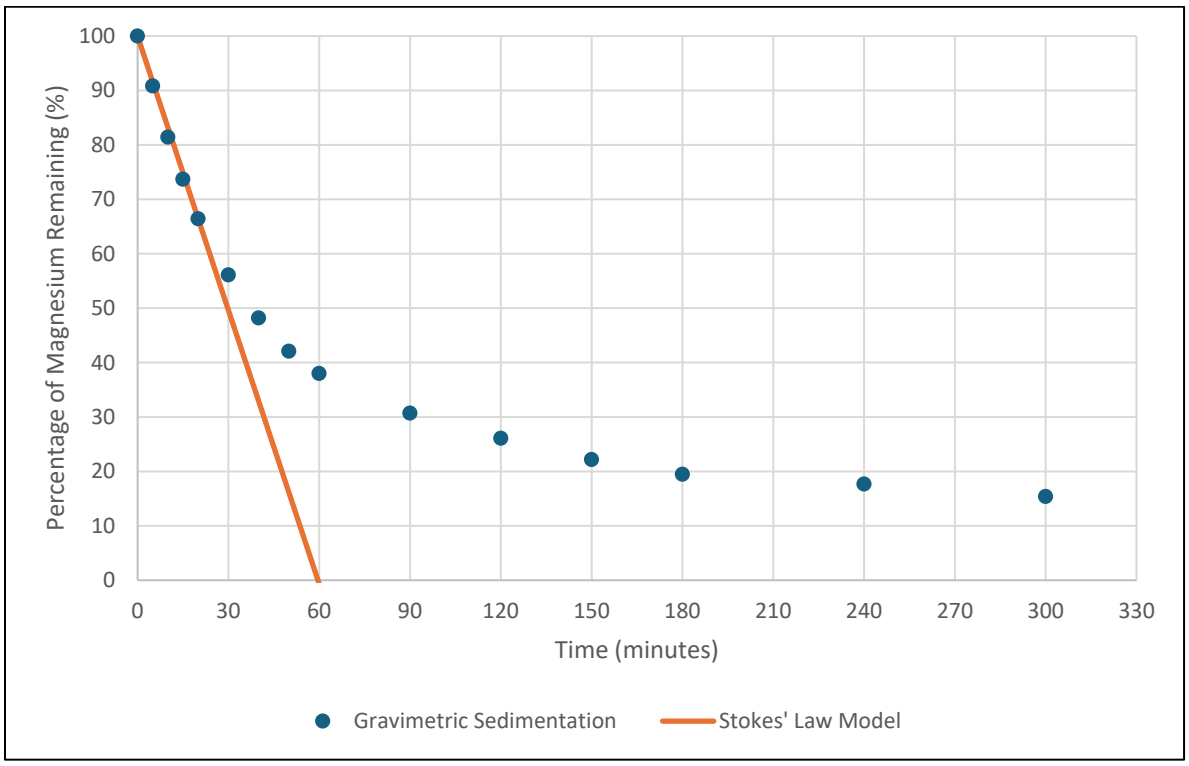

Figure 20. Percentage of magnesium remaining in suspension versus time since the start of gravimetric sedimentation, including single-fit Stokes' law approximation.

To confirm the static settling behavior and its relevance for printing further, a control sample was fabricated under static conditions using a conventional commercial VPP resin vat system on printer M3P and subsequently processed and analyzed using the microscopy methods described previously. The gold-coated, sectioned cylinder and a representative SEM image are shown in Figure 20. The particle area fraction measured across the full height of the cylinder is shown in Figure 21. Across all evaluated regions, only negligible magnesium content was detected when produced under static conditions, confirming limited incorporation of particles in the absence of active mixing. By comparison to the gravimetric settling results, this experiment indicated a substantially lower presence of magnesium remaining in solution over time. This disparity can be explained by the difference between the gravimetric settling environment and the printing environment. In gravimetric settling, the fluid column height was approximately 40 mm, while in a conventional resin vat the used amount of printing material would yield a column height of less than 5 mm instead. Based on Stokes' law, this implies that settling should also occur approximately 8 times faster as the settling distance has decreased by the same factor. Using the Stokes' law model from gravimetric settling, this indicates total settling within the system at approximately 7.5 minutes. The first data point in microscopy of the sample was collected at 2mm, corresponding to 13.5 minutes into the print, or nearly double the amount of time that the Stokes' law approximation predicted for total settling. While the single-fit Stokes' law approximation does not describe the full range of particle settling, it does still indicate a likely reason why minimal additive material was present within the print.

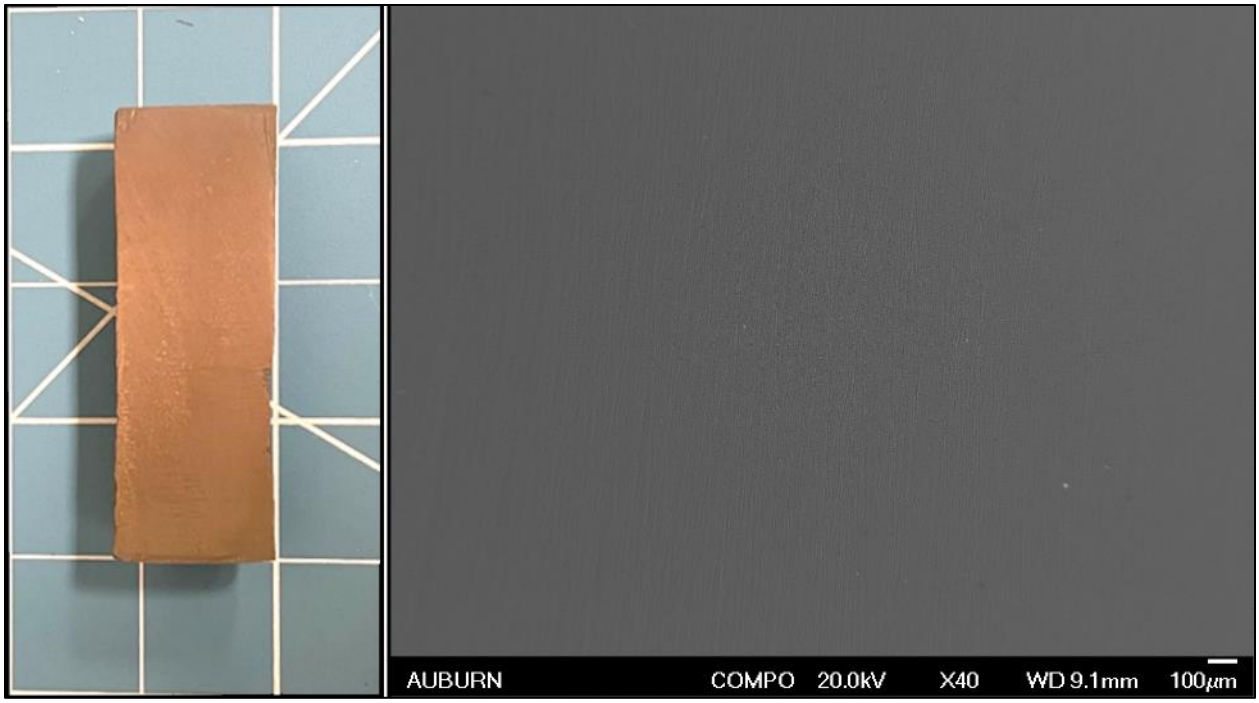

Figure 21. (left) Prepared gold-coated static-printed cylinder for SEM and (right) example SEM image obtained on the centerline of the same cylinder 4 mm from the build platform.

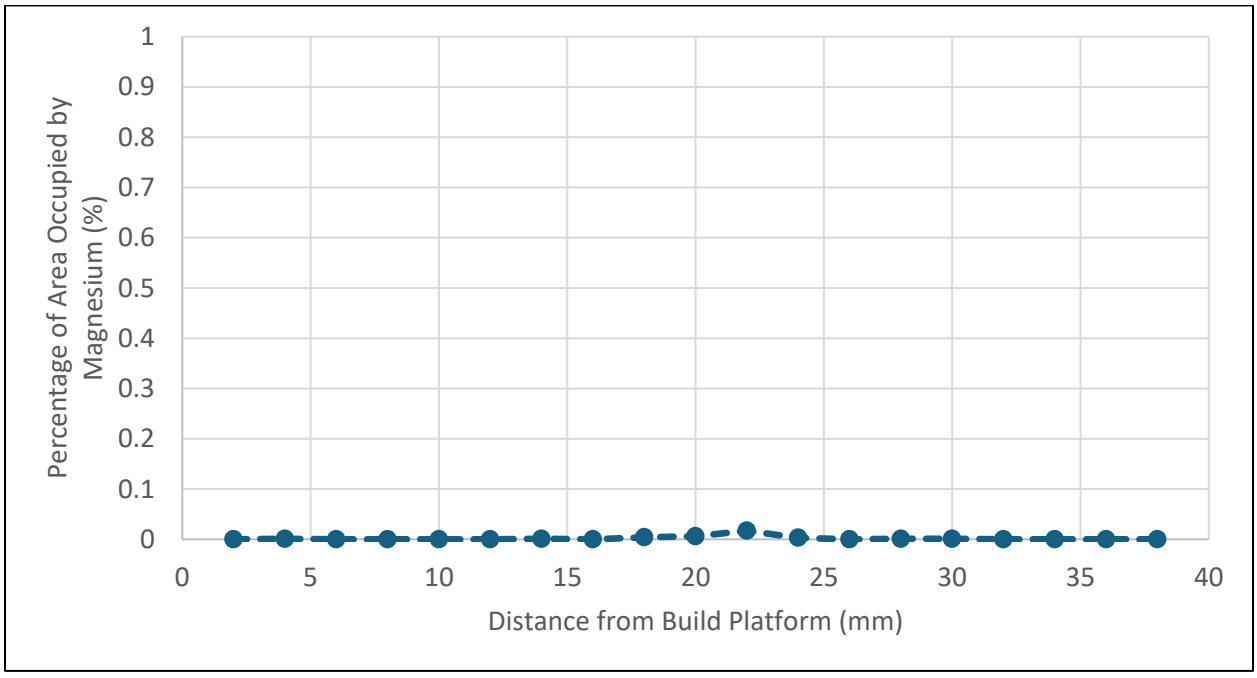

Figure 22. Area percentage occupied by magnesium in collected SEM images of a static-printed cylinder.

Particle Distributions in Printed Material

Particle distributions within printed material can be seen collected in Figure 22 for speed-varying tests conducted on printer M3P, Figure 23 for loading-varying tests conducted on printers M7M-1 and M7M-2, and Figure 24 for particle-size-varying tests on printers M7M-1 and M7M-2. For reference, the macroscopic difference between selected printed cylinders can be seen in Figure 25. Using expression (2) obtained from the simulation results, the estimated loading of magnesium at each location is shown in Figure 26.

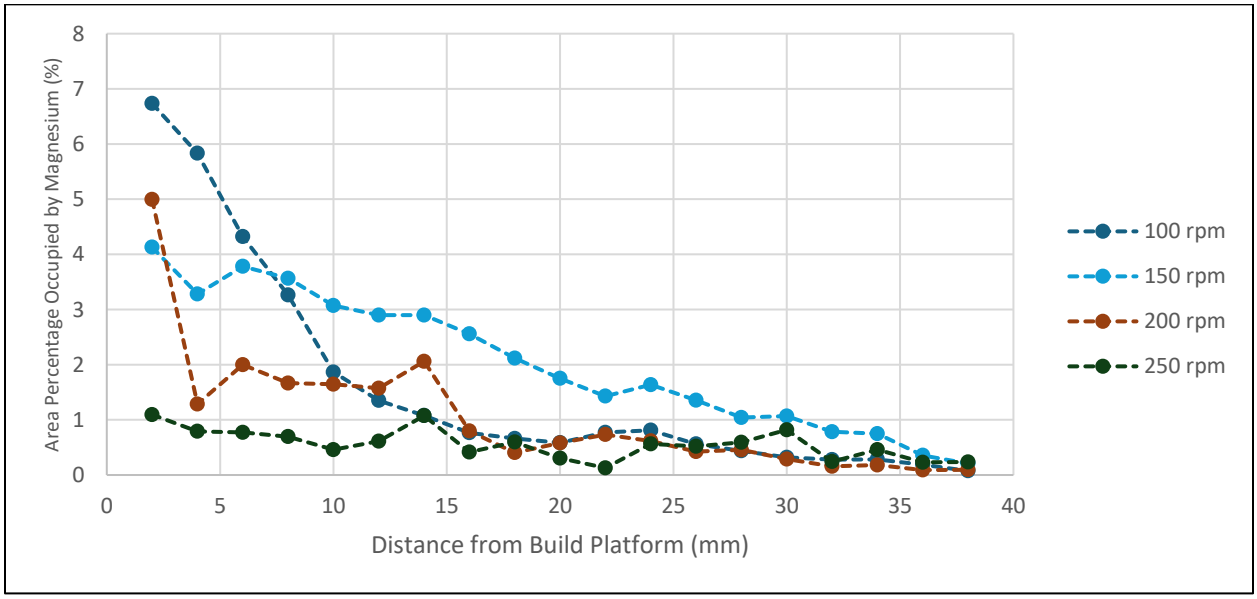

Figure 23. Variation of measured area percentage occupied by magnesium with mixing speed, using a magnesium loading of 0.22 wt%.

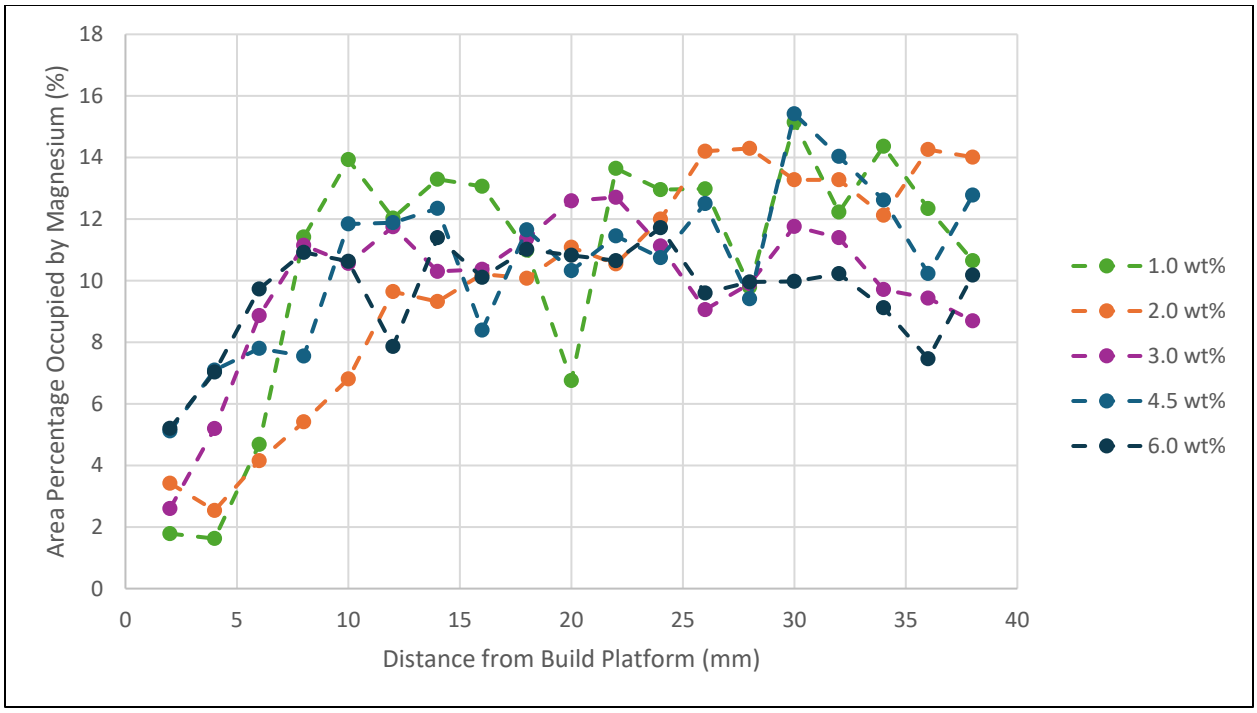

Figure 24. Variation of measured area percentage occupied by magnesium with magnesium loading in the feedstock, printed under 250 rpm of mixing.

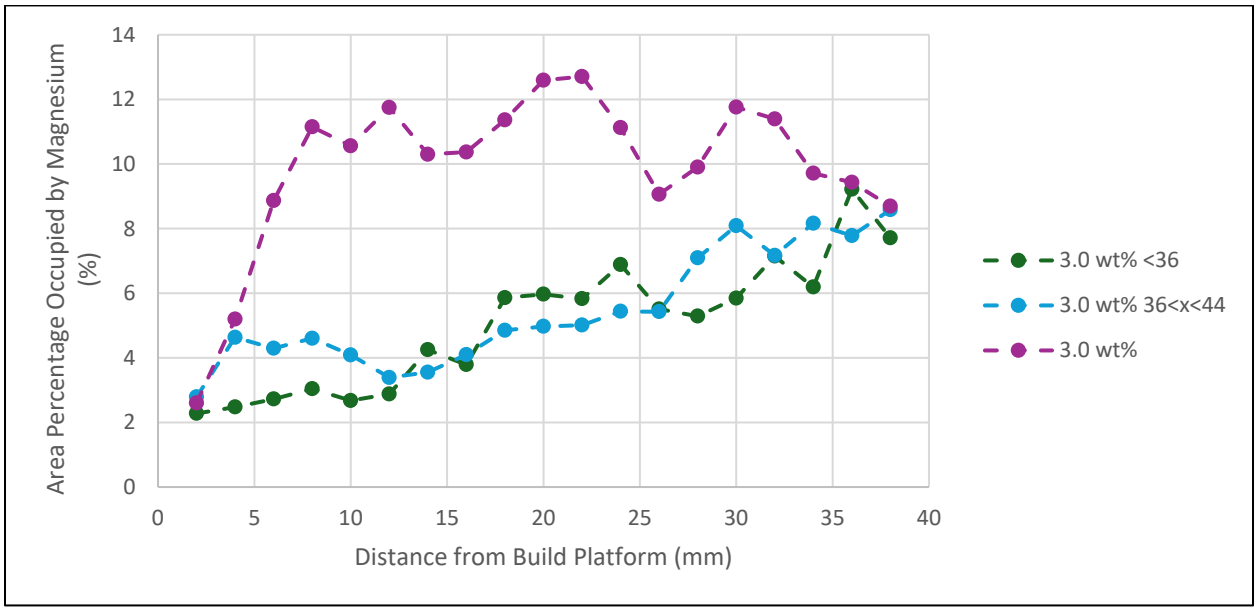

Figure 25. Variation of measured area percentage occupied by magnesium with magnesium particle size, printed under 250 rpm of mixing.

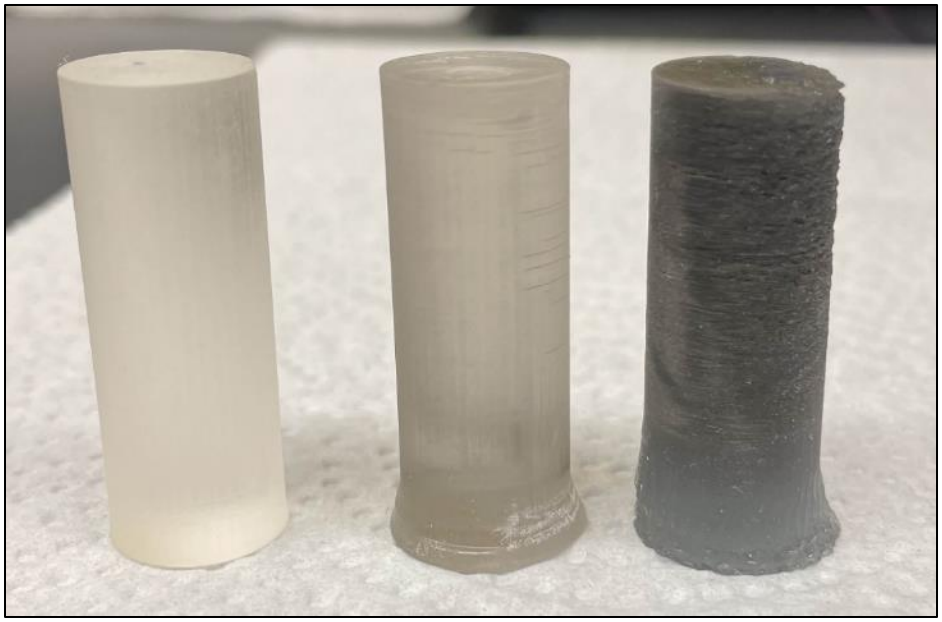

Figure 26. Visual comparison of cylinders produced with no magnesium (left), cylinders produced with 0.22 wt% of magnesium in the feedstock under static conditions (center), and cylinders produced with 0.22 wt% of magnesium in the feedstock under 100 rpm of mixing (right).

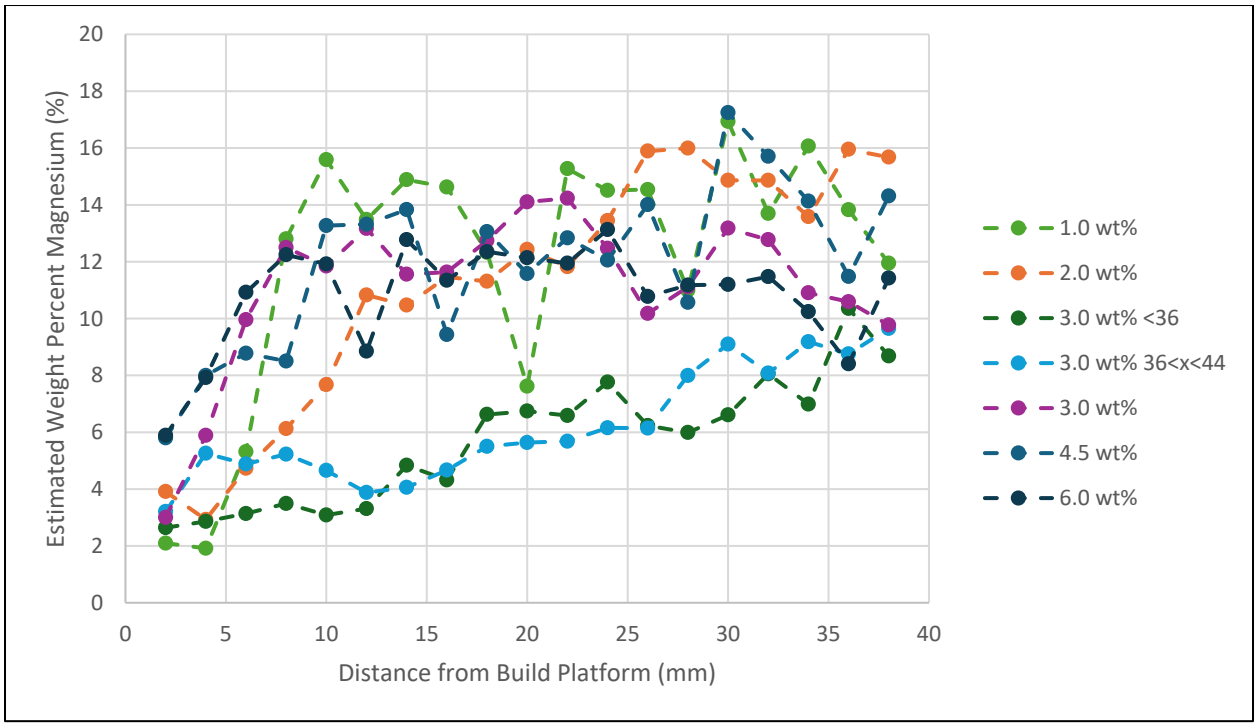

Figure 27. Variation of estimated weight percentage magnesium in each cylinder with the magnesium loading in the feedstock, printed under 250 rpm of mixing.

In speed-varying tests, a clear downward trend is seen in occupied area as printing continues, though the slope of the trend decreases vastly as mixing speed is increased. Additional testing was attempted up to 500 rpm, but speeds of 300 rpm or above resulted in a substantial amount of air inclusion within the printed parts, seen in Figure 27. Subsequent testing with higher loadings at 250 rpm yielded a curious result where the concentration trend had reversed. Rather than decreasing over time, the measured concentration tended to increase as printing continued. Also interesting is that measured area percentage seemed to hold to a consistent value around 11%, even with substantial changes in the concentration of magnesium within the feedstock. This may indicate that the system had reached an equilibrium at some point, but, with comparison to the speed variant data, the fact that an increase in particle loading by a factor of ~5 caused an increase in area percentage within printed parts by a factor of more than 10 is unexpected in this case. The variation with particle size, instead, seems to provide an alternative possibility. Once filtered, either to isolate the larger particles or to isolate the smaller particles, the area percentage resulting from the powder drops much closer to the expected level for each condition. Representative microscope images can be seen in Figure 29 for the 3 wt% magnesium samples. From these images, one possible effect of the particle processing appears to be the breaking up of pre-print agglomerates as agglomeration is noted early in the unmodified particle images, but not in the early images using the other particle sizes. This change in agglomeration may also have led to the difference in settling behavior as a result of the change of the effective size of the additive due to particles clumping together and agglomeration in general may be part of the source of the difference in additive content

noted within the higher feedstock concentration prints compared to the testing at 0.22 wt%.

Figure 28. Example failed prints demonstrating substantial air inclusions resulting from mixing speeds of 300 rpm and above.

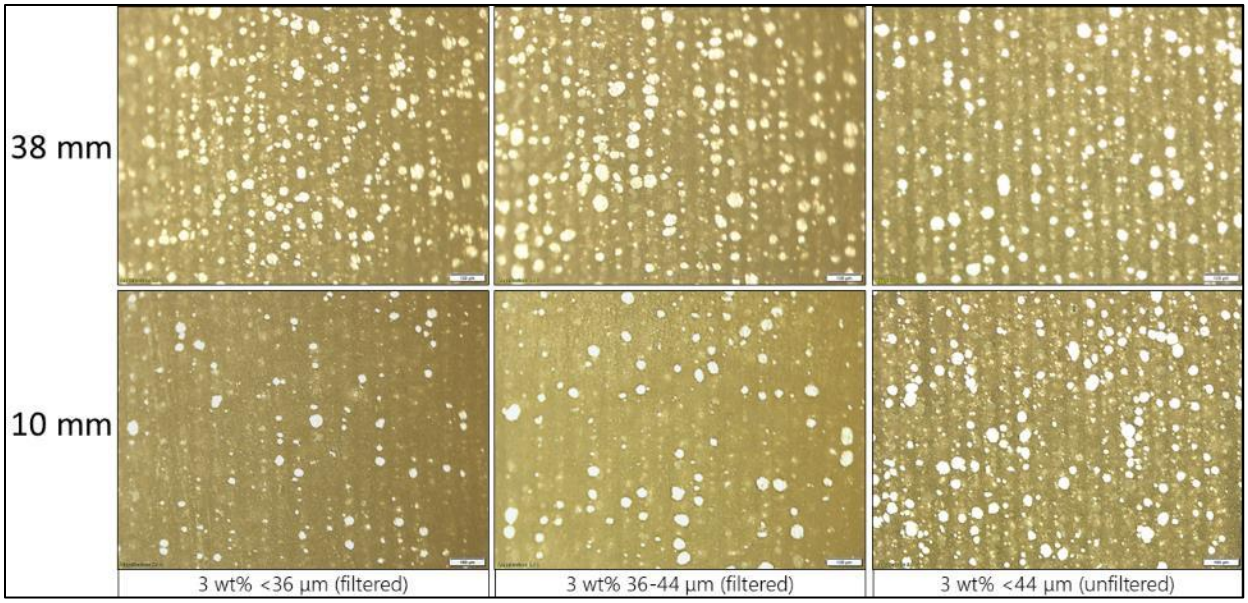

Figure 29. Representative optical microscope images of 3 wt% magnesium samples at 10 mm and 38 mm from the build surface.

Microstructure of Printed Material

Within microscopic examination of the produced material, several features were noted. First, high interfacial contact was noted between the matrix and additive material, as can be seen magnified in Figure 30 and from the representative particle SEM image in Figure 31, and did not have any dependence on the direction of printing. This behavior indicates that the additive particles did not prevent the polymerization of areas immediately behind them due to occlusion of UV light. Second, also observable in Figure 31, the polishing marks can be seen to be consistent across the boundary between magnesium particles and the PEGDA matrix. This, and other imagery, indicates that both magnesium and the used PEGDA were efficiently abraded by the used polishing process. Third, additive material did, however, demonstrate some short-range sedimentation during each polymerization.

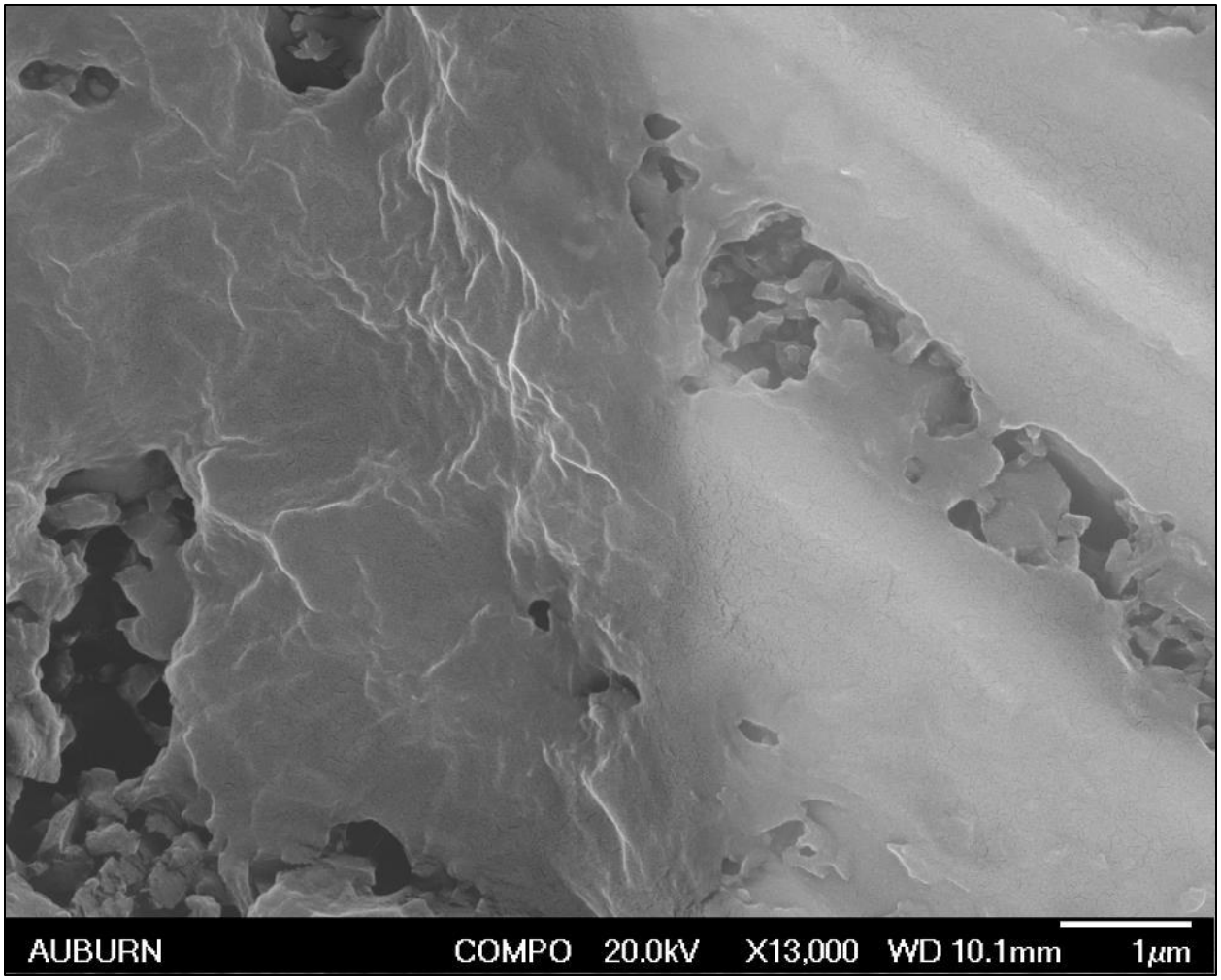

Figure 30. SEM BSE compositional-contrast image of the interface between the PEGDA matrix material and a magnesium particle, rotated compared to normal SEM image orientation for clarity.

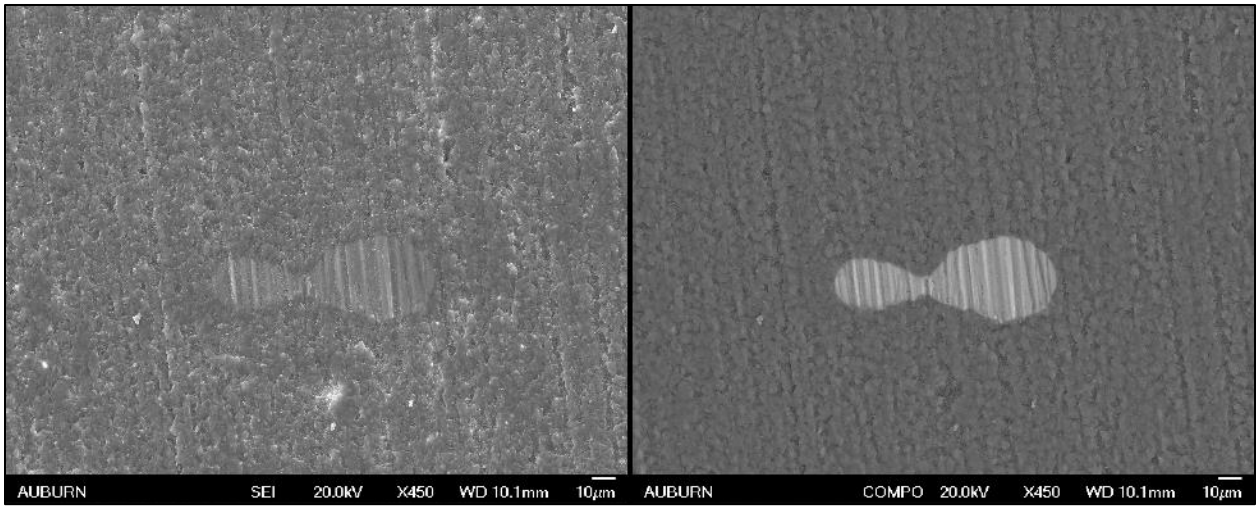

Figure 31. Magnesium particle demonstrating polishing scratches that are continuous with the surrounding PEGDA matrix material. Shown in both SEI topographical contrast (left) and BSE compositional contrast (right) SEM imaging.

During the VPP printing process, a finite exposure time is required for each layer to cure, during which the resin remains effectively static. Under these conditions, suspended additive particles may sediment over short distances toward the release film, resulting in intra-layer concentration gradients. Similar short-range sedimentation effects in VPP composite systems have been reported in previous studies [13].

When using broad particle size distributions, this settling behavior is difficult to arrest. Under such conditions, spatially distinct regions of varying additive concentration may become visible within a single printed layer, as shown in Figure 32. This heterogeneity may introduce local variations in material composition and, consequently, contribute to effects arising from alternating regions of high and low additive content. However, the use of micro-scale particles may allow for matching particle size to the used layer thickness, in this case 50 μm, in order to mitigate this behavior by limiting the maximum settling distance during exposure.

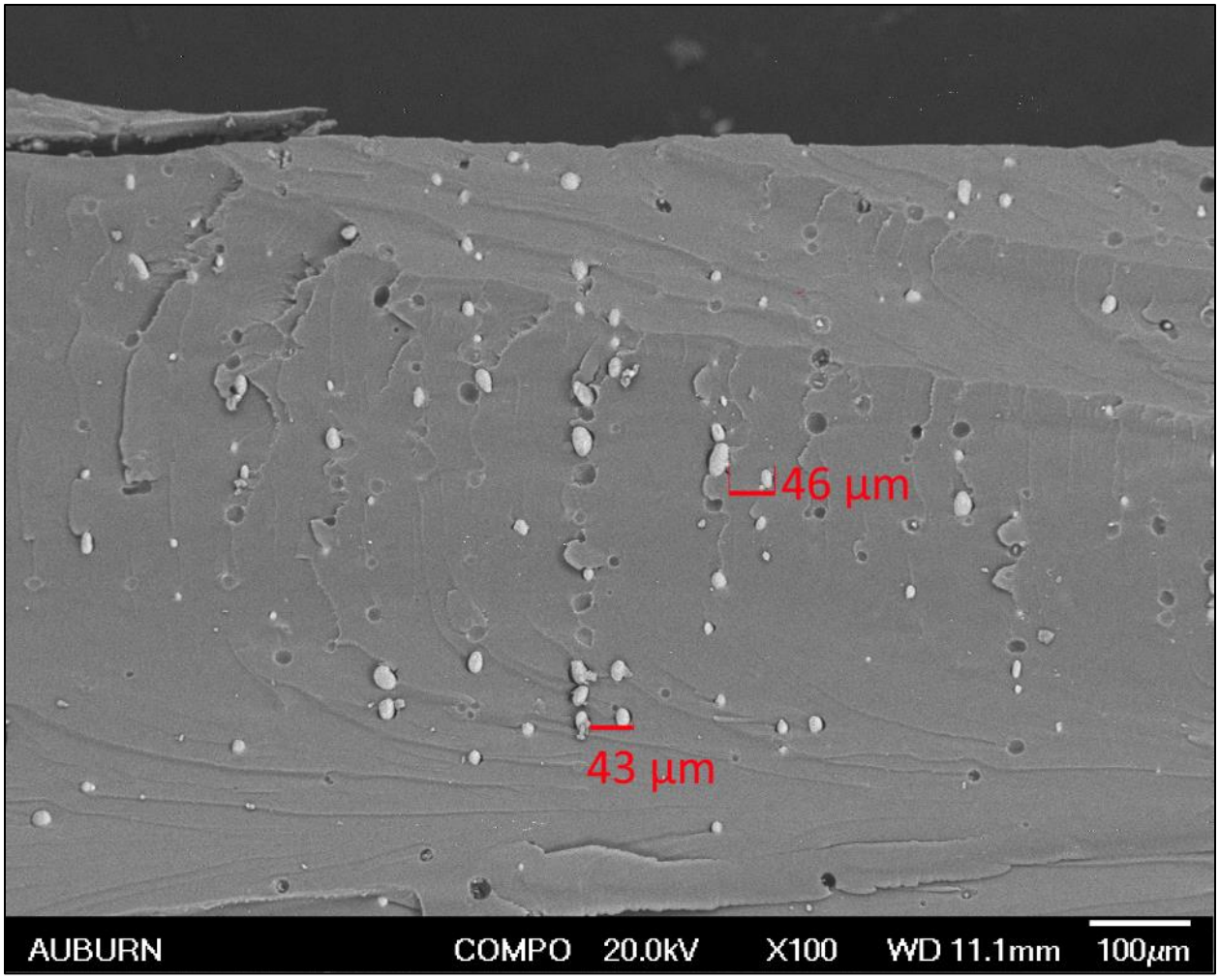

Figure 32. SEM image of interior fracture surface of a magnesium containing cylinder printed under 100 rpm of continuous, single-direction mixing and with a layer height of 50 µm. Annotated with distances between selected settled particles, print direction is oriented left to right from the perspective of the image, displaying vertical layer-lines of settled particles.

Mechanical Testing

The results of the mechanical testing can be seen in Figure 33 for compression and Figure 35 for tensile. In general, compression tests had a wide variance in outcomes, while tensile tests were far more consistent. One-way ANOVA was used to

determine if particle loading had a significant effect upon the tested mechanical properties. For each property, loading percentage was used as the independent variable, with all conditions containing at least three specimens and statistical significance threshold of 0.05. The results from ANOVA indicated that particle loading did not have significant effects on ultimate compressive strength ($F(5, 22) = 0.23$, $p = 0.95$) or ultimate compressive strain ($F(5, 22) = 0.17$, $p = 0.97$), but did have a significant impact on compressive modulus ($F(5, 22) = 13.43$, $p = 4.54E-06$). Follow up evaluation using the Tukey method indicated that only the 0 wt% loading had a significantly different modulus compared to the other conditions. In tension, particle loading was found to have a significant effect on both ultimate tensile stress ($F(5, 13) = 57.91$, $p = 2.00E-08$), ultimate tensile strain ($F(5, 13) = 13.04$, $p = 1.10E-04$), and tensile modulus ($F (5,13) = 157.74$, $p = 3.67E-11$). Follow up evaluation using the Tukey method indicated that the 2 wt% and 0 wt% loadings were significantly different from all other conditions. between 2 wt% and 0 wt%, the ultimate tensile stress was significantly different, but the ultimate tensile strain was not. Lastly, the tensile moduli of the 4.5 wt% condition and the 6.0 wt% condition were also significantly different from each other.

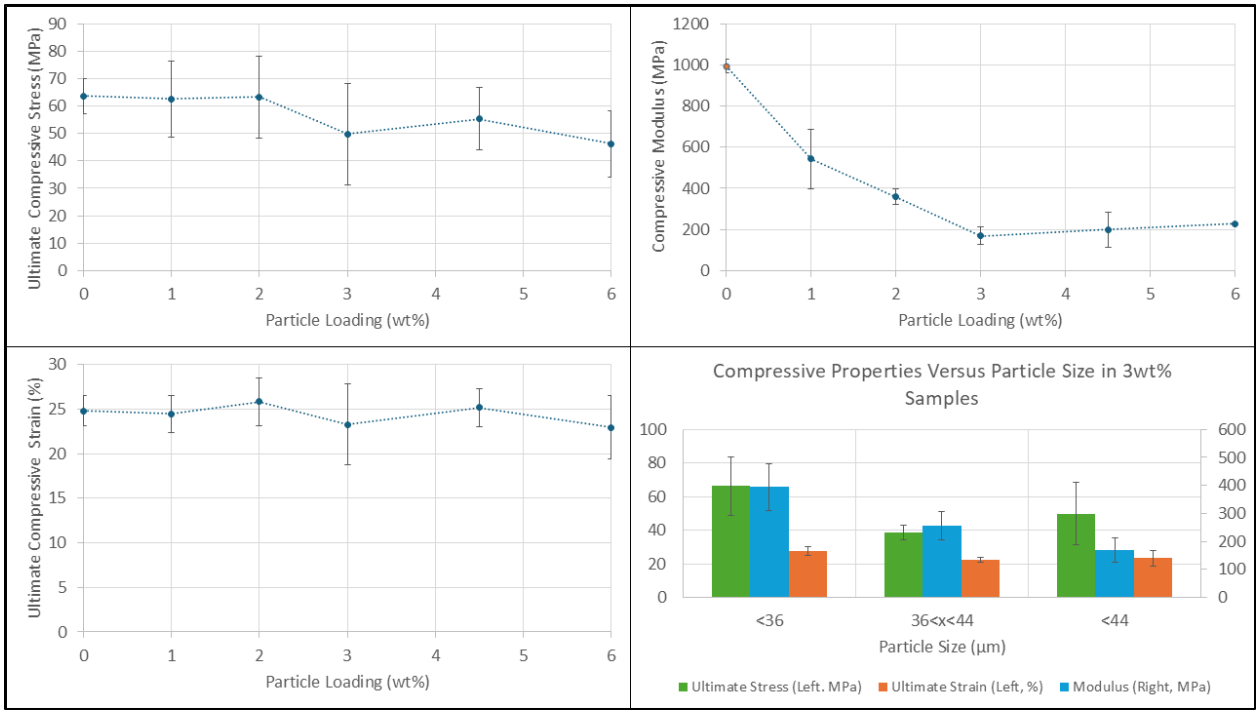

Figure 33. Results of compressive testing on samples containing magnesium loadings between 0 and 6 wt%.

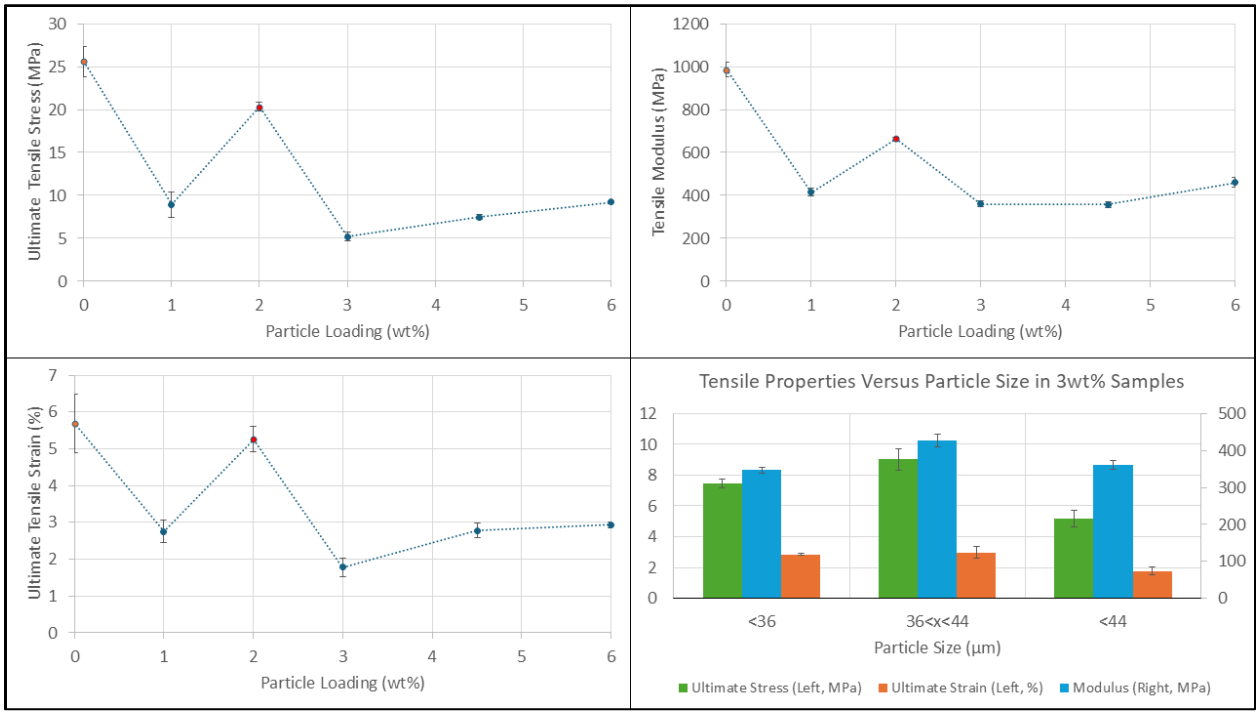

Figure 34. Results of tensile testing on samples containing magnesium loadings between 0 and 6 wt%.

Further analysis of how particle size may affect ultimate strength and ultimate strain indicated that the particle size did not have a significant effect in compression on ultimate strength ($F(2,6) = 0.86$, $p = 0.47$), ultimate strain ($F(2,6) = 0.79$, $p = 0.50$), or modulus ($F(2,6) = 3.34$, $p = 0.11$). In tension, however, ultimate stress ($F(2,9) = 12.41$, $p = 2.5E-03$), and ultimate strain ($F(2,9) = 7.92$, $p = 1.03E-02$), and modulus ($F(2,9) = 13.15$, $p = 2.13E-03$) were significantly affected. For ultimate tensile stress and strain, the two filtered conditions (<36 and 36<x<44 μm) were significantly different from the original condition (<44 μm), but not from each other. In tensile modulus, the 36-44 μm particle size was significantly higher than the other two groups.

No tested magnesium loading was found to significantly exceed the mechanical properties of unmodified PEGDA, but magnesium inclusion did significantly reduce the compressive modulus without causing a corresponding change in ultimate compressive strength. In tension, a 2 wt% magnesium loading was found to produce a significantly higher set of mechanical properties compared to other samples with magnesium. This result may prompt further testing to evaluate loadings close to 2 wt% for the possibility of exceeding the properties of unmodified PEGDA. In addition, particle size was found to significantly affect ultimate strength as well, with substantial increases possible with smaller particles. Combining these two results, testing of smaller particle sizes near loadings of 2 wt% may be a promising direction for PEGDA-Mg composites. However, the difference between the loading in the feedstock and the estimated effective loadings from microscopy indicates that the real loading of these samples is likely to be significantly above the intended ratio and the amount in the feedstock. Further, the real

magnesium loadings may also be much closer in value to each other than the magnesium loadings in the feedstock.

By intent, the addition of magnesium particles was to serve to strengthen the material by reducing matrix deformation as a result of the presence of particles, allowing for force transfer to the particles, and pinning the formation of cracks. However, as the mechanical properties decreased, it appears that these effects may have been outweighed by the particles, especially agglomerated particles, serving instead as force concentrators and crack initiating points instead. These negatives may have also been exacerbated as a result of the increased effective loading compared to the intended loading within the feedstock, and may be partially addressed by reducing the effective loading. Lastly, the agglomeration noted was less present following the filtering and fractioning of the obtained magnesium powder, which may mean that pre-print powder processing may partially address these negatives as well, and may be part of the reason why the fractioned particle size samples performed significantly better than the as-delivered particle size samples in tension.

Mass-loss dissolution

The recorded masses of each specimen across the 30-day test period can be seen in Figure 36, and the total percent change in mass for each specimen at each day in Figure 37. Magnesium containing samples appear to have substantially higher mass changes compared to unmodified PEGDA in all conditions, with higher particle loadings in the feedstock leading to generally higher percent change in mass as well, as shown in Figure 37. Particle size variations at 3 wt% magnesium loadings each demonstrated

similar behavior, with a slight trend towards lower mass change as particle size decreased, as shown in Figure 38. As time in the dissolution media increased, all samples demonstrated an increasingly present layer of a white material on their surface, represented in Figure 39. This layer is expected to be primarily magnesium hydroxide as a result of the degradation of magnesium and magnesium oxide within 1X PBS. This particular degradation process may also have caused a correspondent raise in the pH of the material adjacent to magnesium particles due to the aqueous presence of numerous hydroxide groups, which then may have accelerated the hydrolysis of the bonds within the PEGDA and led to faster degradation of the polymeric material. Faster degradation of the PEGDA may have led to a higher porosity and, thus, water absorption. Both the presence of solid magnesium degradation products and increased PEGDA degradation allowing higher water absorption are likely to have contributed to the higher mass-increases noted in magnesium-containing samples compared to unmodified PEGDA.

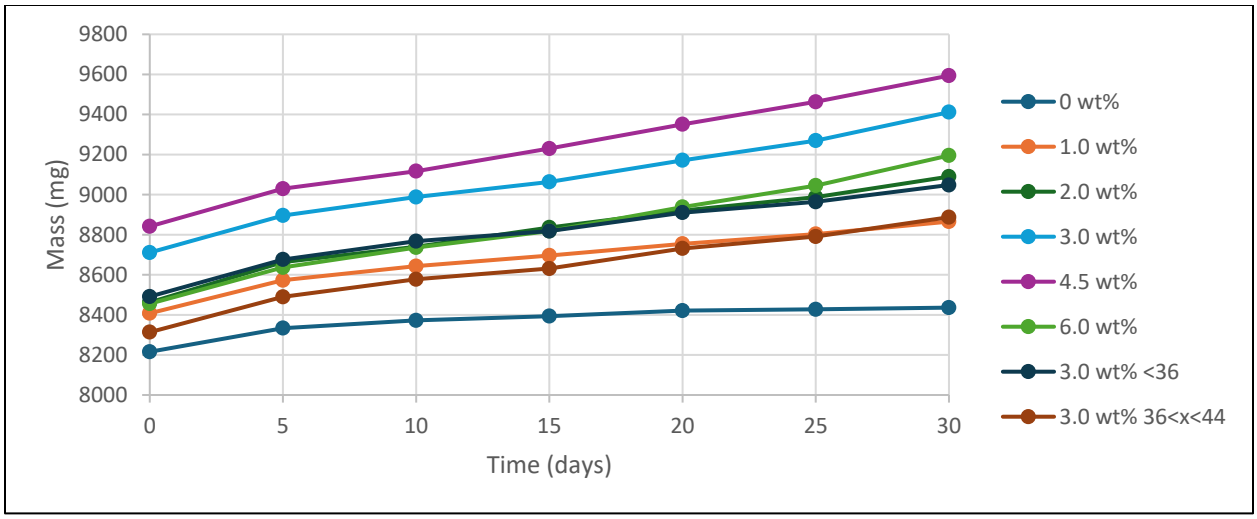

Figure 35. Mass of cylinders printed from feedstock containing various loadings of magnesium versus time spent in dissolution environment.

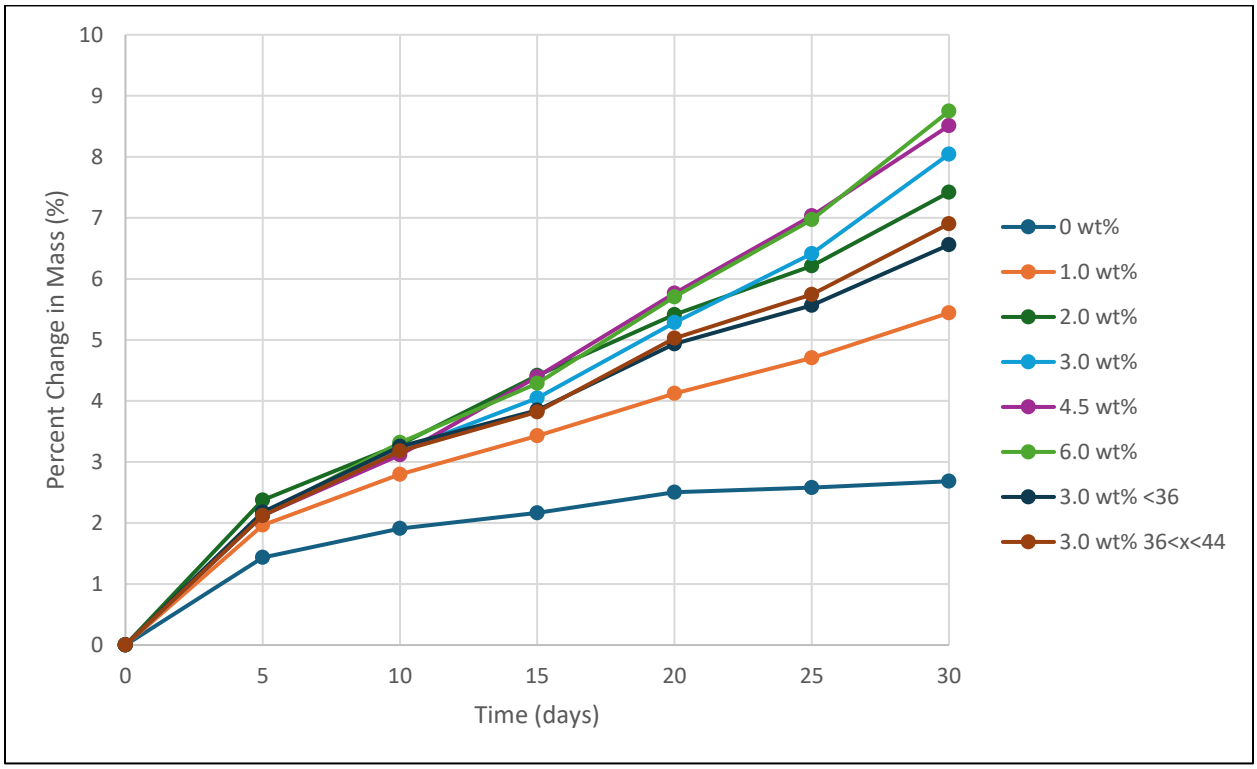

Figure 36. Percent change in the mass of cylinders printed from feedstock containing various loadings of magnesium versus time spent in dissolution environment.

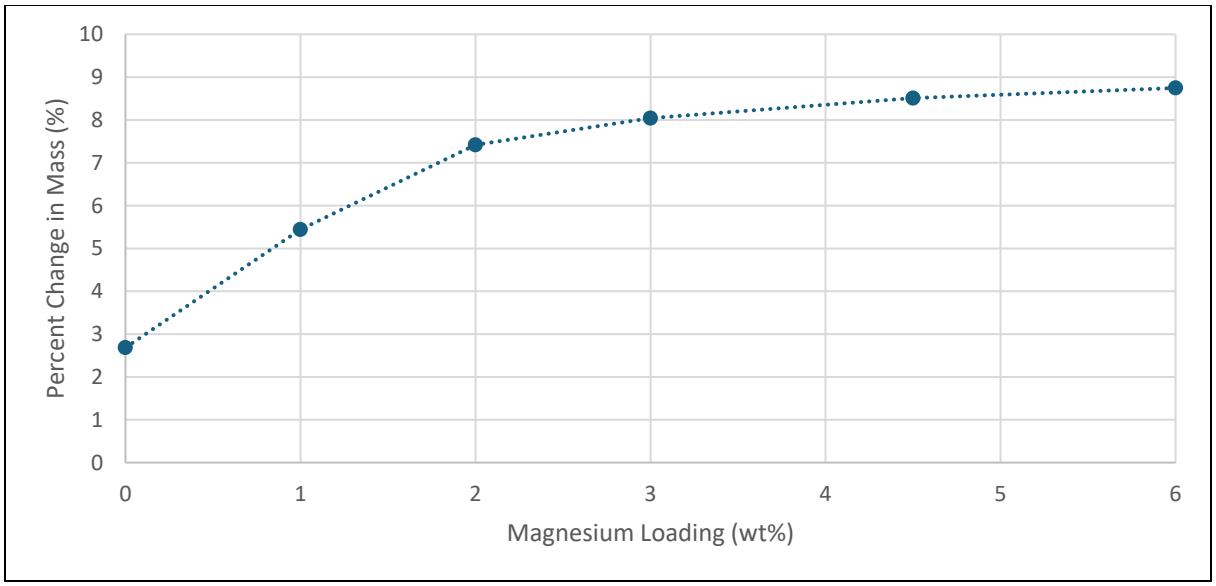

Figure 37. Percent change in the mass of printed cylinders at 30 days in dissolution environment, versus loading of magnesium in the feedstock.

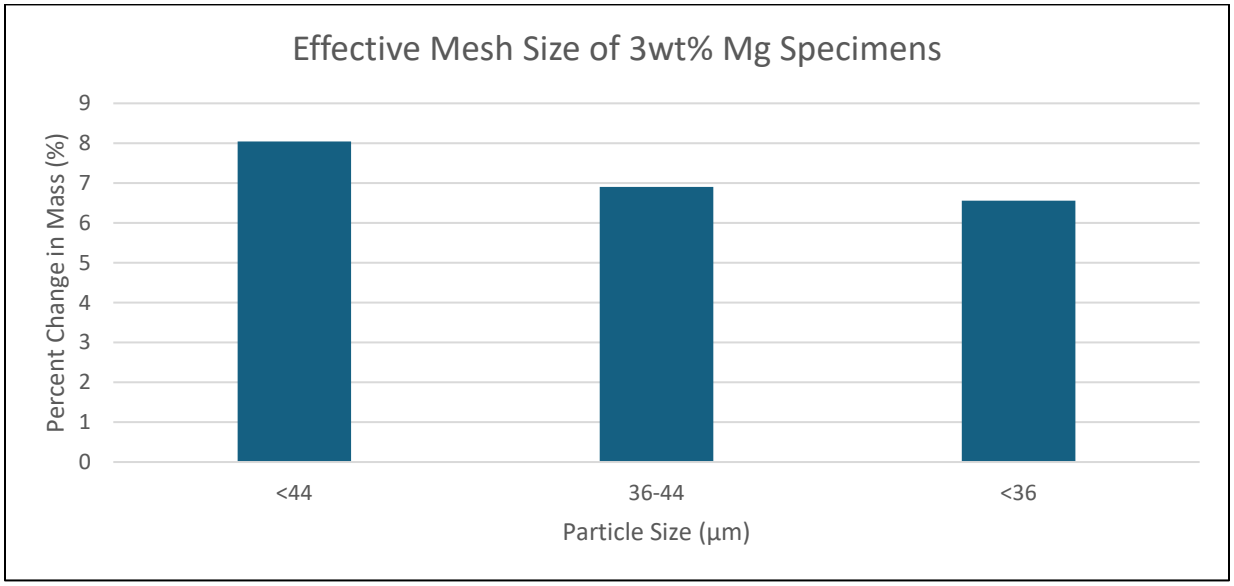

Figure 38. Percent change in the mass of 3 wt% magnesium cylinders at 30 days in dissolution environment, versus size of magnesium particles.

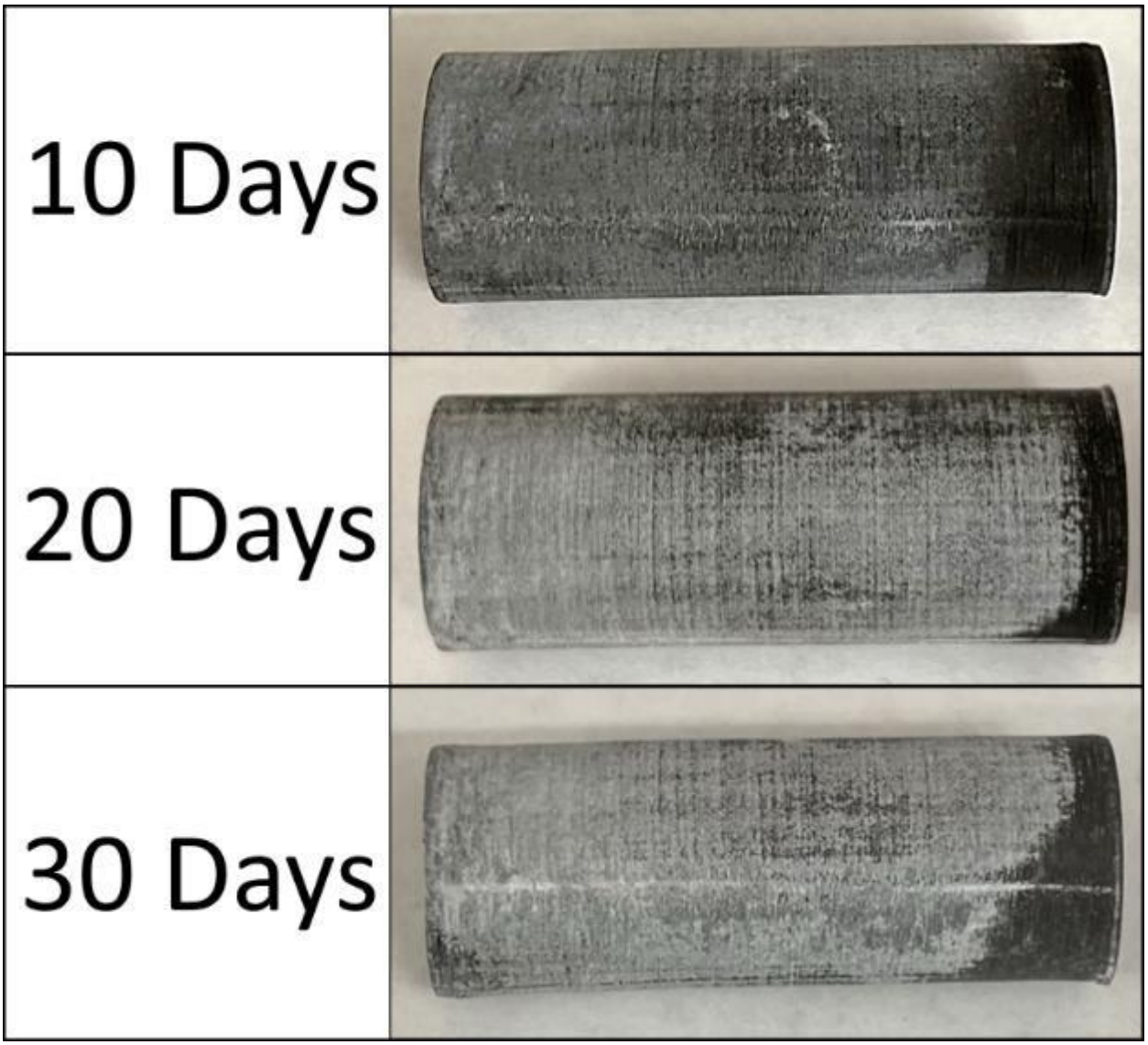

Figure 39. Representative images of cylinders at 10, 20, and 30 days of dissolution. Images are of the 3 wt% magnesium cylinder, using particles less than 44 μm.

Chapter 5 - Conclusions and Future Directions

VPP Mixing System

The presented mixing system for VPP additive manufacturing provides substantial improvement in the distribution of additive material, can be produced rapidly

and inexpensively and can be easily adapted for attachment to a large number of commercial VPP systems. Compared to heavily involved chemical modification methods, this design can be added to presently existing research workflows far more quickly and with minimal effects on the properties of the final part. For some applications, chemical additive solutions may still be viable if not highly beneficial, but the mixer system provides the ability to test additive combinations prior to the development and testing of specialized suspending compounds or similar. This allows for the rapid development and testing of new composite materials for use in a variety of applications without the pre-existing development of specialized suspending agents. Additionally, suspending agents used in industry, though often suitable for many purposes, do not always suspend the additive material permanently. Though settling is often substantially slowed, it can still lead to noticeable inhomogeneity over the course of printing. The mixer system, by contrast, provides homogenizing forces and currents which may be able to maintain presently existing commercial composite resins longer than chemical solutions, possibly providing greater repeatability in part outcomes and also limiting the need for feedstock to be removed from the printing environment for re-homogenization between prints.

Mechanical solutions are currently becoming relevant in industry with several companies exploring solutions such as resin recirculation systems which pump the feedstock to a separate environment for homogenization or slight axial oscillation of the resin vat during printing. However, the system presented here has a much smaller form factor than publicly available descriptions of presently existing industrial solutions and may provide similar or greater benefits. Further, the mixing system here can be used

with consumer desktop printers quite easily, where prior solutions are often only suitable for much larger industrial printing systems. From the perspective of enabling future research, desktop VPP printers have a far lower bar for entry and new equipment which enables them to be used for the more efficient design and production of composite resins could be significantly beneficial to the field.

In terms of improving the mixing system from its current state, moving away from single-direction mixing and into reversing mixing patterns and more developed internal mixing geometry may enable superior homogenization performance. While this improvement may be useful for PEGDA-Mg, it may also enable the system to be more easily applied for material combinations demonstrating even faster settling than this test material.

PEGDA-Mg Hybrids

Though there were no successfully produced composites demonstrating higher mechanical properties than unmodified PEGDA, the PEGDA-Mg composite material does still offer promise. In particular, the particle distributions within printed samples seems to indicate that, despite the feedstock loading, the settings or geometry of the mixer may have led to a stratification of material within the feedstock, or similar behavior, causing the effective concentration within the printed material to approximate the same value despite the differences in the feedstock. This is further supported by the very similar mechanical performance of several of the loadings. Further research utilizing revised mixing patterns and behavior may be able to overcome this behavior and test a wider range of effective loadings. In addition, the microscopy information on

the samples using other particle sizes seems to indicate that agglomeration of the particles prior to printing may be a significant factor for print performance. In particular, the filtered-particle-containing samples demonstrated enhanced performance when evaluated in tension compared to the unmodified-particle-containing samples, which may further indicate that either smaller particles are beneficial in this material, or that agglomeration is a significant source of the weakening noted in tensile testing.

Summary

In conclusion, this work presents and qualifies a new system and methodology for producing composites within VPP additive manufacturing. The test material, PEGDA-Mg, did not demonstrate the desired mechanical properties in the tested loadings, but did demonstrate the ability of the system and methodology for producing composites, without any suspending agents or modification of the feedstock. Given that present methods of addressing settling inside of composite VPP feedstocks rely on additives and altered rheology, often making sacrifices to print quality or part performance in the process, the mixer system presents a new, viable, method of limiting settling in VPP without necessarily imposing the same penalties.

References

[1] T.D. Ngo, A. Kashani, G. Imbalzano, K.T.Q. Nguyen, D. Hui, Additive manufacturing (3D printing): A review of materials, methods, applications and challenges, Composites Part B: Engineering 143 (2018) 172-196.
[2] M. Salmi, Additive Manufacturing Processes in Medical Applications, Materials (Basel) 14(1) (2021).
[3] A. Pandey, S. Sahoo, Progress on Medical Implant: A Review and Prospects, Journal of Bionic Engineering 20(2) (2023) 470-494.
[4] S. Chatterjee, M. Saxena, D. Padmanabhan, M. Jayachandra, H.J. Pandya, Futuristic medical implants using bioresorbable materials and devices, Biosensors and Bioelectronics 142 (2019) 111489.
[5] H. Ibrahim, S.N. Esfahani, B. Poorganji, D. Dean, M. Elahinia, Resorbable bone fixation alloys, forming, and post-fabrication treatments, Materials Science and Engineering: C 70 (2017) 870-888.
[6] Z. Liu, Q. Lei, S. Xing, Mechanical characteristics of wood, ceramic, metal and carbon fiber-based PLA composites fabricated by FDM, Journal of Materials Research and Technology 8(5) (2019) 3741-3751.
[7] J. Mogan, L. Sandanamsamy, W.S.W. Harun, I. Ishak, F.R.M. Romlay, K. Kadirgama, D. Ramasamy, Thermo-mechanical properties of ABS/stainless steel composite using FDM, Materials Today: Proceedings (2024).
[8] D. Jiang, F. Ning, Fused Filament Fabrication of Biodegradable PLA/316L Composite Scaffolds: Effects of Metal Particle Content, Procedia Manufacturing 48 (2020) 755-762.
[9] F. Alam, V.R. Shukla, K.M. Varadarajan, S. Kumar, Microarchitected 3D printed polylactic acid (PLA) nanocomposite scaffolds for biomedical applications, Journal of the Mechanical Behavior of Biomedical Materials 103 (2020) 103576.
[10] J. Lee, H. Lee, K.-H. Cheon, C. Park, T.-S. Jang, H.-E. Kim, H.-D. Jung, Fabrication of poly(lactic acid)/Ti composite scaffolds with enhanced mechanical properties and biocompatibility via fused filament fabrication (FFF)–based 3D printing, Additive Manufacturing 30 (2019) 100883.
[11] E. Yarali, M.J. Mirzaali, A. Ghalayaniesfahani, A. Accardo, P.J. Diaz-Payno, A.A. Zadpoor, 4D Printing for Biomedical Applications, Advanced Materials 36(31) (2024) 2402301.
[12] S. Zakeri, M. Vippola, E. Levänen, A comprehensive review of the photopolymerization of ceramic resins used in stereolithography, Additive Manufacturing 35 (2020) 101177.
[13] E. Prause, J. Hey, F. Beuer, J. Yassine, B. Hesse, T. Weitkamp, J. Gerber, F. Schmidt, Microstructural investigation of hybrid CAD/CAM restorative dental materials by micro-CT and SEM, Dental Materials 40(6) (2024) 930-940.
[14] S. Safaee, A. Otero, M. Fei, T. Liu, J. Zhang, R.K. Chen, Particle-resin systems for additive manufacturing of rigid and elastic magnetic polymeric composites, Additive Manufacturing 51 (2022) 102587.
[15] P.K. Picariello, Y. Im, T.J. Kolibaba, C.I. Higgins, G.L. Brennecka, Disentangling physical and chemical consequences of particle sedimentation in ceramic vat photopolymerization, Journal of the European Ceramic Society 46(15) (2026) 118517.

[16] M. Yuan, M. Hu, F. Dai, Y. Fan, Z. Deng, H. Deng, Y. Cheng, Application of synthetic and natural polymers in surgical mesh for pelvic floor reconstruction, Materials & Design 209 (2021) 109984.
[17] M. Kauke-Navarro, L. Knoedler, S. Knoedler, C. Deniz, L. Stucki, A.-F. Safi, Balancing beauty and science: a review of facial implant materials in craniofacial surgery, Frontiers in Surgery 11 (2024).
[18] M.N. Collins, G. Ren, K. Young, S. Pina, R.L. Reis, J.M. Oliveira, Scaffold Fabrication Technologies and Structure/Function Properties in Bone Tissue Engineering, Advanced Functional Materials 31(21) (2021) 2010609.
[19] O.I. Velikokhatnyi, P.N. Kumta, First principles study of the elastic properties of magnesium and iron based bio-resorbable alloys, Materials Science and Engineering: B 230 (2018) 20-23.
[20] S. McMahon, N. Bertollo, E.D. O'Cearbhaill, J. Salber, L. Pierucci, P. Duffy, T. Dürig, V. Bi, W. Wang, Bio-resorbable polymer stents: a review of material progress and prospects, Progress in Polymer Science 83 (2018) 79-96.
[21] S. Vach Agocsova, M. Culenova, I. Birova, L. Omanikova, B. Moncmanova, L. Danisovic, S. Ziaran, D. Bakos, P. Alexy, Resorbable biomaterials used for 3D scaffolds in tissue engineering: A review, Materials 16(12) (2023) 4267.
[22] Y. Qin, P. Wen, H. Guo, D. Xia, Y. Zheng, L. Jauer, R. Poprawe, M. Voshage, J.H. Schleifenbaum, Additive manufacturing of biodegradable metals: Current research status and future perspectives, Acta biomaterialia 98 (2019) 3-22.
[23] D. Hong, D.-T. Chou, O.I. Velikokhatnyi, A. Roy, B. Lee, I. Swink, I. Issaev, H.A. Kuhn, P.N. Kumta, Binder-jetting 3D printing and alloy development of new biodegradable Fe-Mn-Ca/Mg alloys, Acta Biomaterialia 45 (2016) 375-386.
[24] K. Oh-ishi, R. Watanabe, C.L. Mendis, K. Hono, Age-hardening response of Mg–0.3at.%Ca alloys with different Zn contents, Materials Science and Engineering: A 526(1) (2009) 177-184.
[25] Y. Sun, B. Zhang, Y. Wang, L. Geng, X. Jiao, Preparation and characterization of a new biomedical Mg–Zn–Ca alloy, Materials & Design 34 (2012) 58-64.
[26] U. Sharma, D. Concagh, L. Core, Y. Kuang, C. You, Q. Pham, G. Zugates, R. Busold, S. Webber, J. Merlo, R. Langer, George M. Whitesides, M. Palasis, The development of bioresorbable composite polymeric implants with high mechanical strength, Nature Materials 17(1) (2018) 96-103.
[27] R.N. Oosterbeek, X.C. Zhang, S.M. Best, R.E. Cameron, The evolution of the structure and mechanical properties of fully bioresorbable polymer-glass composites during degradation, Composites Science and Technology 218 (2022) 109194.
[28] J.A. Weisman, D.H. Ballard, U. Jammalamadaka, K. Tappa, J. Sumerel, H.B. D'Agostino, D.K. Mills, P.K. Woodard, 3D Printed Antibiotic and Chemotherapeutic Eluting Catheters for Potential Use in Interventional Radiology: In Vitro Proof of Concept Study, Academic Radiology 26(2) (2019) 270-274.
[29] J.B. Wolinsky, Y.L. Colson, M.W. Grinstaff, Local drug delivery strategies for cancer treatment: Gels, nanoparticles, polymeric films, rods, and wafers, Journal of Controlled Release 159(1) (2012) 14-26.
[30] Y. Wang, L. Sun, Z. Mei, F. Zhang, M. He, C. Fletcher, F. Wang, J. Yang, D. Bi, Y. Jiang, P. Liu, 3D printed biodegradable implants as an individualized drug delivery

system for local chemotherapy of osteosarcoma, Materials & Design 186 (2020) 108336.
[31] Y. Yang, X. Qiao, R. Huang, H. Chen, X. Shi, J. Wang, W. Tan, Z. Tan, E-jet 3D printed drug delivery implants to inhibit growth and metastasis of orthotopic breast cancer, Biomaterials 230 (2020) 119618.
[32] P. Fouladian, Q. Jin, M. Arafat, Y. Song, X. Guo, A. Blencowe, S. Garg, Drug-Loaded, Polyurethane Coated Nitinol Stents for the Controlled Release of Docetaxel for the Treatment of Oesophageal Cancer, Pharmaceuticals 14(4) (2021) 311.
[33] L. Xu, Q. Yang, W. Qiang, H. Li, W. Zhong, S. Pan, G. Yang, Hydrophilic Excipient-Independent Drug Release from SLA-Printed Pellets, Pharmaceutics 13(10) (2021) 1717.
[34] H. Sun, C. Zhang, B. Zhang, P. Song, X. Xu, X. Gui, X. Chen, G. Lu, X. Li, J. Liang, J. Sun, Q. Jiang, C. Zhou, Y. Fan, X. Zhou, X. Zhang, 3D printed calcium phosphate scaffolds with controlled release of osteogenic drugs for bone regeneration, Chemical Engineering Journal 427 (2022) 130961.
[35] V. Martin, I.A. Ribeiro, M.M. Alves, L. Gonçalves, R.A. Claudio, L. Grenho, M.H. Fernandes, P. Gomes, C.F. Santos, A.F. Bettencourt, Engineering a multifunctional 3D-printed PLA-collagen-minocycline-nanoHydroxyapatite scaffold with combined antimicrobial and osteogenic effects for bone regeneration, Materials Science and Engineering: C 101 (2019) 15-26.
[36] Q. Dong, M. Zhang, X. Zhou, Y. Shao, J. Li, L. Wang, C. Chu, F. Xue, Q. Yao, J. Bai, 3D-printed Mg-incorporated PCL-based scaffolds: A promising approach for bone healing, Materials Science and Engineering: C 129 (2021) 112372.
[37] Y. Gu, J. Zhang, X. Zhang, G. Liang, T. Xu, W. Niu, Three-dimensional Printed Mg-Doped β-TCP Bone Tissue Engineering Scaffolds: Effects of Magnesium Ion Concentration on Osteogenesis and Angiogenesis In Vitro, Tissue Engineering and Regenerative Medicine 16(4) (2019) 415-429.
[38] K. Takata, H. Takai, Y. Yoshizaki, T. Nagata, K. Kawahara, Y. Yoshida, A. Kuzuya, Y. Ohya, Peptide Drug Release Behavior from Biodegradable Temperature-Responsive Injectable Hydrogels Exhibiting Irreversible Gelation, Gels 3(4) (2017) 38.
[39] H. Khan, J.P. Chaudhary, R. Meena, Anionic carboxymethylagarose-based pH-responsive smart superabsorbent hydrogels for controlled release of anticancer drug, International Journal of Biological Macromolecules 124 (2019) 1220-1229.
[40] Z. Chen, S. Song, J. Ma, S.D. Ling, Y.D. Wang, T.T. Kong, J.H. Xu, Fabrication of magnetic core/shell hydrogels via microfluidics for controlled drug delivery, Chemical Engineering Science 248 (2022) 117216.
[41] J. Morton, M. Derakhshan, S. Kaza, C. Li, Design of the Invisalign system performance, Seminars in Orthodontics 23(1) (2017) 3-11.
[42] J.-A. Lee, Y.-G. Koh, K.-T. Kang, Biomechanical and Clinical Effect of Patient-Specific or Customized Knee Implants: A Review, Journal of Clinical Medicine 9(5) (2020) 1559.
[43] M. Meier, S. Zingde, A. Steinert, W. Kurtz, F. Koeck, J. Beckmann, What Is the Possible Impact of High Variability of Distal Femoral Geometry on TKA? A CT Data Analysis of 24,042 Knees, Clinical Orthopaedics and Related Research® 477(3) (2019) 561-570.

[44] E.L. Papazoglou, N.E. Karkalos, P. Karmiris-Obratański, A.P. Markopoulos, On the Modeling and Simulation of SLM and SLS for Metal and Polymer Powders: A Review, Archives of Computational Methods in Engineering 29(2) (2022) 941-973.
[45] A.E. Patterson, S.L. Messimer, P.A. Farrington, Overhanging Features and the SLM/DMLS Residual Stresses Problem: Review and Future Research Need, Technologies 5(2) (2017) 15.
[46] A. Khorasani, I. Gibson, J.K. Veetil, A.H. Ghasemi, A review of technological improvements in laser-based powder bed fusion of metal printers, The International Journal of Advanced Manufacturing Technology 108(1) (2020) 191-209.
[47] A. Soltani-Tehrani, J.P. Isaac, H.V. Tippur, D.F. Silva, S. Shao, N. Shamsaei, Ti-6Al-4V powder reuse in laser powder bed fusion (L-PBF): The effect on porosity, microstructure, and mechanical behavior, International Journal of Fatigue 167 (2023) 107343.
[48] V.K. Tiwary, A. P., A.S. Deshpande, N. Rangaswamy, Surface enhancement of FDM patterns to be used in rapid investment casting for making medical implants, Rapid Prototyping Journal 25(5) (2019) 904-914.
[49] C.S. Lee, S.G. Kim, H.J. Kim, S.H. Ahn, Measurement of anisotropic compressive strength of rapid prototyping parts, Journal of Materials Processing Technology 187-188 (2007) 627-630.
[50] Y. Bao, Recent Trends in Advanced Photoinitiators for Vat Photopolymerization 3D Printing, Macromolecular Rapid Communications 43(14) (2022) 2200202.
[51] K. Elkhoury, J. Zuazola, S. Vijayavenkataraman, Bioprinting the future using light: A review on photocrosslinking reactions, photoreactive groups, and photoinitiators, SLAS Technology 28(3) (2023) 142-151.
[52] C. Warr, J.C. Valdoz, B.P. Bickham, C.J. Knight, N.A. Franks, N. Chartrand, P.M. Van Ry, K.A. Christensen, G.P. Nordin, A.D. Cook, Biocompatible PEGDA Resin for 3D Printing, ACS Applied Bio Materials 3(4) (2020) 2239-2244.
[53] W. Harun, M. Kamariah, N. Muhamad, S. Ghani, F. Ahmad, Z. Mohamed, A review of powder additive manufacturing processes for metallic biomaterials, Powder Technology 327 (2018) 128-151.
[54] S. Saleh Alghamdi, S. John, N. Roy Choudhury, N.K. Dutta, Additive Manufacturing of Polymer Materials: Progress, Promise and Challenges, Polymers 13(5) (2021) 753.
[55] D. Wang, J. Wang, Z. Shen, C. Jiang, J. Zou, L. Dong, N.X. Fang, G. Gu, Soft actuators and robots enabled by additive manufacturing, Annual Review of Control, Robotics, and Autonomous Systems 6 (2023) 31-63.
[56] E. Ghio, E. Cerri, Additive Manufacturing of AlSi10Mg and Ti6Al4V Lightweight Alloys via Laser Powder Bed Fusion: A Review of Heat Treatments Effects, Materials 15(6) (2022) 2047.
[57] D. Syrlybayev, B. Zharylkassyn, A. Seisekulova, M. Akhmetov, A. Perveen, D. Talamona, Optimisation of Strength Properties of FDM Printed Parts—A Critical Review, Polymers 13(10) (2021) 1587.
[58] A. Garg, A. Bhattacharya, A. Batish, Chemical vapor treatment of ABS parts built by FDM: Analysis of surface finish and mechanical strength, The International Journal of Advanced Manufacturing Technology 89(5) (2017) 2175-2191.

[59] A. Katz-Demyanetz, V.V. Popov Jr, A. Kovalevsky, D. Safranchik, A. Koptioug, Powder-bed additive manufacturing for aerospace application: Techniques, metallic and metal/ceramic composite materials and trends, Manufacturing review 6 (2019).
[60] P. Parandoush, D. Lin, A review on additive manufacturing of polymer-fiber composites, Composite Structures 182 (2017) 36-53.
[61] M. Strano, K. Rane, F.B. Vangosa, L. Di Landro, Extrusion of metal powder-polymer mixtures: Melt rheology and process stability, Journal of Materials Processing Technology 273 (2019) 116250.
[62] S. Mubarak, D. Dhamodharan, M. B. Kale, N. Divakaran, T. Senthil, S. P, L. Wu, J. Wang, A novel approach to enhance mechanical and thermal properties of SLA 3D printed structure by incorporation of metal–metal oxide nanoparticles, Nanomaterials 10(2) (2020) 217.
[63] Z. Guo, A.A. Poot, D.W. Grijpma, Advanced polymer-based composites and structures for biomedical applications, European Polymer Journal 149 (2021) 110388.
[64] M. Mohammadi Zerankeshi, R. Bakhshi, R. Alizadeh, Polymer/metal composite 3D porous bone tissue engineering scaffolds fabricated by additive manufacturing techniques: A review, Bioprinting 25 (2022) e00191.
[65] C. Shuai, Y. Li, P. Feng, W. Guo, W. Yang, S. Peng, Positive feedback effects of Mg on the hydrolysis of poly-l-lactic acid (PLLA): Promoted degradation of PLLA scaffolds, Polymer Testing 68 (2018) 27-33.
[66] L. Carlsson, T. Röstlund, B. Albrektsson, T. Albrektsson, P.-I. Brånemark, Osseointegration of titanium implants, Acta Orthopaedica Scandinavica 57(4) (1986) 285-289.
[67] M. Shah, A. Ullah, K. Azher, A. Ur Rehman, N. Akturk, W. Juan, C.S. Tüfekci, M.U. Salamci, The Influence of Nanoparticle Dispersions on Mechanical and Thermal Properties of Polymer Nanocomposites Using SLA 3D Printing, Crystals 13(2) (2023) 285.
[68] M. Dehghan, M. Tahmasebipour, S. Ebrahimi, Design, fabrication, and characterization of an SLA 3D printed nanocomposite electromagnetic microactuator, Microelectronic Engineering 254 (2022) 111695.
[69] I. Romero-Ocaña, S.I. Molina, Cork photocurable resin composite for stereolithography (SLA): Influence of cork particle size on mechanical and thermal properties, Additive Manufacturing 51 (2022) 102586.
[70] L.D. Gil, S.N. Monteiro, H.A. Colorado, Polymer Matrix Nanocomposites Fabricated with Copper Nanoparticles and Photopolymer Resin via Vat Photopolymerization Additive Manufacturing, Polymers 16(17) (2024) 2434.
[71] M. Mousapour, J. Partanen, M. Salmi, NiTiCu alloy from elemental and alloyed powders using vat photopolymerization additive manufacturing, Additive Manufacturing 78 (2023) 103853.
[72] C. Xiao, K. Zheng, S. Chen, N. Li, X. Shang, F. Wang, J. Liang, S.B. Khan, Y. Shen, B. Lu, H. Ma, Z. Chen, Additive manufacturing of high solid content lunar regolith simulant paste based on vat photopolymerization and the effect of water addition on paste retention properties, Additive Manufacturing 71 (2023) 103607.
[73] J. Tang, H. Zhang, H. Chang, X. Guo, C. Wang, Y. Wei, Z. Huang, Y. Yang, Vat photopolymerization-based additive manufacturing of high-strength RB-SiC ceramics by

introducing quasi-spherical diamond, Journal of the European Ceramic Society 43(13) (2023) 5436-5445.
[74] L. Šimunović, L. Brenko, A.J. Marić, S. Meštrović, T. Haramina, Rheology of Dental Photopolymers for SLA/DLP/MSLA 3D Printing, Polymers 17(19) (2025) 2706.
[75] S.Y. Song, M.S. Park, J.W. Lee, J.S. Yun, A Study on the Rheological and Mechanical Properties of Photo-Curable Ceramic/Polymer Composites with Different Silane Coupling Agents for SLA 3D Printing Technology, Nanomaterials 8(2) (2018) 93.
[76] C. Alparslan, M. Minaz, E. Baysal, M.F. Yentimur, O. Koçar, Ş. Bayraktar, Mechanical Enhancement and Fracture Mechanisms of SLA Photopolymer Composites Reinforced with Fish Bone Ash, Polymers 18(11) (2026) 1348.
[77] A. Al Rashid, A. Afridi, M. Koç, Mechanical Performance of Laminated Polymer Composites Fabricated via Stereolithography (SLA) 3D Printing, Chemistry 7(6) (2025) 179.
[78] S. Mahadevappa Bale, G. Devalapura Paramashivaiah, D. Mudigere Hanumanthappa, K. Ramaiah, Influence of Material Composition and Printing Parameters on Impact Strength and Hardness Properties of SLA-Fabricated BN/Resin Composites, Polymers for Advanced Technologies 36(9) (2025) e70325.
[79] S. Mubarak, D. Dhamodharan, M. B. Kale, N. Divakaran, T. Senthil, S. P., L. Wu, J. Wang, A Novel Approach to Enhance Mechanical and Thermal Properties of SLA 3D Printed Structure by Incorporation of Metal–Metal Oxide Nanoparticles, Nanomaterials 10(2) (2020) 217.
[80] M.B. Swathi, D.P. Girish, M.H. Dinesh, R. Keshavamurthy, K. Manjunatha, Taguchi-Based Analysis of Wear Performance in SLA Printed Boron Nitride Composites, Journal of Bio- and Tribo-Corrosion 11(2) (2025) 63.
[81] P.S. Sokolov, D.A. Komissarenko, I.A. Shmeleva, I.V. Slyusar, G.A. Dosovitskiy, P.V. Evdokimov, V.I. Putlyaev, A.E. Dosovitskiy, Suspensions on the basis of stabilised zirconium oxide for three-dimensional printing, IOP Conference Series: Materials Science and Engineering 347(1) (2018) 012012.
[82] M. Alshihabi, M.Y. Kayacan, Effect of nanosized carbon nanotubes, Titanium Nitride and cubic Boron Nitride powders on mechanical and thermal properties of SLA 3D printed resin composites, Polymer Composites 45(17) (2024) 15561-15573.